

ISTANBUL TECHNICAL UNIVERSITY ★ GRADUATE SCHOOL OF SCIENCE
ENGINEERING AND TECHNOLOGY

**MECHANICS OF NANOMATERIALS
CONSISTED OF RANDOM NETWORKS**

Ph.D. THESIS

Mesut KIRCA

Department of Mechanical Engineering

Mechanical Engineering Programme

AUGUST 2013

ISTANBUL TECHNICAL UNIVERSITY ★ GRADUATE SCHOOL OF SCIENCE
ENGINEERING AND TECHNOLOGY

**MECHANICS OF NANOMATERIALS
CONSISTED OF RANDOM NETWORKS**

Ph.D. THESIS

**Mesut KIRCA
(503062028)**

Department of Mechanical Engineering

Mechanical Engineering Programme

**Thesis Advisor: Prof. Dr. Ata MUĞAN
Co-Advisor: Assist. Prof. Albert C. TO**

AUGUST 2013

İSTANBUL TEKNİK ÜNİVERSİTESİ ★ FEN BİLİMLERİ ENSTİTÜSÜ

RASTGELE AĞ YAPILI NANO MALZEMELERİN MEKANIĞI

DOKTORA TEZİ

**Mesut KIRCA
(503062028)**

Makina Mühendisliği Bölümü

Makine Mühendisliği Programı

Tez Danışmanı: Prof. Dr. Ata MUĞAN

Eş Danışman: Yard. Doç. Dr. Albert C. TO

AĞUSTOS 2013

Mesut KIRCA, a Ph.D. student of ITU **Graduate School of Science, Engineering and Technology** student ID 503062028, successfully defended the **dissertation** entitled “MECHANICS OF NANOMATERIALS CONSISTED OF RANDOM NETWORKS”, which he prepared after fulfilling the requirements specified in the associated legislations, before the jury whose signatures are below.

Thesis Advisor : **Prof.Dr. Ata MUĞAN**
Istanbul Technical University

Co-Advisor : **Assist.Prof. Albert C. TO**
University of Pittsburgh

Jury Members : **Prof.Dr. Alaeddin ARPACI**
Istanbul Technical University

Prof.Dr. Uğur GÜVEN
Yıldız Technical University

Assoc.Prof. Celaletdin ERGÜN
Istanbul Technical University

Assoc.Prof. Serdar BARIŞ
Istanbul University

Assist.Prof. Ali GÖKŞENLİ
Istanbul Technical University

Date of Submission : 31 May 2013
Date of Defense : 06 August 2013

To my spouse, Aslihan and daughter, Defne,

FOREWORD

Firstly, I would like to convey my gratitude to my advisors, Professor Ata Muğan and Professor Albert C. To, who provided me fundamental advises. They always supported me strongly in my research studies with availability, patience and encouragement. I am very grateful for the things that I learnt from them, not only the scientific matters, but also lots of knowledge which are very helpful in all aspects of my life. It had been a true privilege to learn from such competent and sincere supervisors.

Secondly, I would like to offer my great appreciation to my parents and my wife who have always encouraged and supported me through my many years of academic endeavors. They are the driving force behind all of my successes. I could not have accomplished this without them.

August 2013

Mesut KIRCA

TABLE OF CONTENTS

	<u>Page</u>
FOREWORD.....	ix
TABLE OF CONTENTS.....	xi
ABBREVIATIONS	xiii
LIST OF TABLES	xv
LIST OF FIGURES	xvii
SUMMARY	xxi
ÖZET.....	xxv
1. INTRODUCTION.....	1
1.1 Nanomaterials.....	2
1.1.1 Applications of nanomaterials	3
1.1.2 Classification of nanomaterials	6
1.1.3 Manufacturing of nanomaterials	6
1.2 Introduction to Nanoporous Materials	8
1.2.1 Properties of nanoporous materials	11
1.2.2 Major opportunities in applications of nanoporous materials.....	11
1.3 Introduction to Carbon Nanotubes	12
1.3.1 Geometry of CNTs.....	14
1.3.2 Manufacturing of CNTs	15
1.3.3 Applications of carbon nanotubes	16
1.4 Purpose of Thesis	18
2. OVERVIEW OF MOLECULAR DYNAMICS SIMULATIONS.....	21
2.1 Introduction	21
2.2 History and Future of MD Simulations.....	25
2.3 Limitations on MD	27
2.4 Time Evolution in MD Simulation.....	29
2.5 Interatomic Potentials.....	31
2.5.1 Pairwise interactions	33
2.5.2 Lennard-Jones potential	33
2.5.3 Embedded atom method.....	34
2.5.4 Adaptive intermolecular reactive empirical bond-order potential	35
2.6 Overview of LAMMPS	36
3. ATOMISTIC MODELLING AND MECHANICS OF NANOPOROUS MATERIALS	39
3.1 Introduction	39
3.2 Literature Review	41
3.2.1 Theoretical and semi-empirical models for macroporous foams	43
3.2.2 Experimental studies on nanoporous foams.....	45
3.2.3 Studies on the Young's modulus of nanoporous materials.....	47
3.2.4 Studies on the yield strength of nanoporous materials	49
3.2.5 Studies on the Tensile Behavior of Nanoporous Materials.....	58

3.3 Atomistic Modeling of Nanoporous Materials	61
3.3.1 Random network nature of nanoporous materials.....	61
3.3.2 Algorithm for generation of nanoporous models	62
3.4 Numerical Experiments	67
3.5 Results	71
3.6 Summary and Conclusion.....	76
4. STOCHASTIC MODELING AND MECHANICS OF CARBON NANOTUBE NETWORKS.....	79
4.1 Purpose	79
4.2 Literature Review	79
4.2.1 Elastic modulus of CNTs	82
4.2.2 Tensile strength of CNTs	83
4.2.3 Buckling and bending of carbon nanotubes	85
4.2.4 Studies on CNT Network Materials	87
4.3 Atomistic Modelling of Heat Welded CNT Networks.....	91
4.3.1 General Concepts	91
4.3.2 General Algorithm.....	92
4.3.2.1 Line segment representation of CNTs.....	93
4.3.2.2 Target based approach.....	94
4.3.2.3 Checking constraints	96
4.3.2.4 Making decision	97
4.3.3 Sample Networks and Welding Procedure.....	97
4.3.4 Statistical Characterization of Random Networks	103
4.4 Investigations on the Mechanical Behavior of CNT Networks.....	106
4.4.1 Numerical Experiments.....	106
4.4.2 Results	109
4.5 Summary and Conclusion.....	117
5. CONCLUSIONS AND RECOMMENDATIONS	121
REFERENCES	127
APPENDICES	139
APPENDIX A	141
CURRICULUM VITAE	145

ABBREVIATIONS

AFM	: Atomic Force Microscope
AIREBO	: Adaptive Intermolecular Reactive Empirical Bond-Order
CLU	: Cubic Lattice Unit
CNT	: Carbon Nanotube
CVD	: Chemical Vapor Deposition
DIC	: Digital Image Correlation
DNA	: Deoxyribonucleic Acid
DOE	: Department of Energy
EAM	: Embedded Atom Method
EBSD	: Electron Backscatter Diffraction
EMI	: Electromagnetic Interference
FE	: Finite Element
HRTEM	: High Resolution Transmission Electron Microscope
IUPAC	: International Union of Pure and Applied Chemistry
LAMMPS	: Large-scale Atomic/Molecular Massively Parallel Simulator
MNP	: Metal Nanoparticles
MWNT	: Multi-walled Carbon Nanotube
REBO	: Reactive Empirical Bond-Order
RNA	: Ribonucleic Acid
NP	: Nanoporous
SEM	: Scanning Electron Microscope
SWNT	: Single Walled Carbon Nanotube
TEM	: Transmission Electron Microscope
USA	: United States of America

LIST OF TABLES

	<u>Page</u>
Table 1.1 : Examples of microporous, mesoporous and macroporous materials.....	10
Table 3.1 : Parameters employed in the random sphere generation algorithm.....	69
Table 4.1 : Experimental studies on the determination of the Young's modulus of CNTs.....	80
Table 4.2 : Numerical studies on the determination of the Young's modulus of the CNTs.....	81
Table 4.3 : Summary of quantitative results from tensile loading simulations.....	112
Table 4.4 : Summary of quantitative results from shear loading simulations.....	117

LIST OF FIGURES

	<u>Page</u>
Figure 1.1 : From macro-materials to atom.	2
Figure 1.2 : Nanomaterials with different morphologies: (a) Au nanoparticle, (b) Buckminsterfullerene, (c) FePt nanosphere, (d) Titanium nanoflower, (e) Silver nanocubes, and (f) SnO ₂ nanoflower.	4
Figure 1.3 : Classification of nanomaterials.	6
Figure 1.4 : Scheme of Top-Down and Bottom-up approaches to the synthesis of metal nanoparticles (MNP).	7
Figure 1.5 : Specific surface area enhancements: (a) Three blocks having the same volume initially but different surface areas due to different features, (b) Surface area increments by splitting a volume.	9
Figure 1.6 : Three different types of nanoporous silica materials. (a) A microporous material: zeolite, (b) A mesoporous material, (c) A macroporous material.....	10
Figure 1.7 : Different structural forms of carbon element (a) diamond, (b) graphite, (c) Lonsdaleite (hexagonal diamoond), (d) Buckminster-Fullerene (C60), (e) C540, (f) C70, (g) amorphous carbon, (h) Nanotube.	13
Figure 1.8 : (a) Different rolling directions on a graphene sheet causing different chiralities, (b) General geometric parameters for CNTs.....	15
Figure 1.9 : CNT composites and macrostructures (a) Micrograph showing the cross section of a carbon fiber laminate with the CNTs dispersed in the epoxy resin and its application. (b) CNT sheets and yarns used as lightweight data cables and electromagnetic (EM) shielding material.	17
Figure 2.1 : Examples of nanostructures that can be simulated by MD (a) Nanowires, (b) Carbon nanotubes, (c) Bio-molecules.	22
Figure 2.2 : Molecular device design examples (a) Gear chain and (b) Planetary Gear.....	26
Figure 2.3 : MD simulations workflow.....	28
Figure 2.4 : (a) Two-body potential parameters, (b) 3-body potential parameters ..	32
Figure 2.5 : Lennard-Jones potential.....	34
Figure 3.1 : Sample nanoporous material morphologies: (a) Nanoporous Gold (b) Nanoporous Platin.....	40
Figure 3.2 : SEM micrographs of 8000-mN indentations on a fractured surface of np gold: (a) conospherical tip with a tip radius of 0.1 mm, and (b) Berkovich tip with a curvature of 200 nm. Ductile densification is observed for both probes. Note that the plastic deformation is confined to the area under the indenter, and adjacent areas are virtually undisturbed.....	51

Figure 3.3 : Experimental values for foam yield stress for samples of np Au with relative density ranging from 20% to 42%, normalized by the yield stress of fully dense Au. The solid line presents the Gibson and Ashby prediction for a gold foam.....	52
Figure 3.4 : The load-displacement curve recorded during in-situ TEM nanoindentation of a 150 nm np-Au film. It appears that the load drops (marked by arrows) corresponding to collective collapse of a layer of pores.	55
Figure 3.5 : True stress-strain curves from 1, 4 and 8 μm diameter nanoporous Au columns	57
Figure 3.6 : Foam models employed for the mechanical response of carbon foams (a) Computer Aided Drawing (CAD) model, (b) FEA results of foam models.	62
Figure 3.7 : (a) Representation of a target sphere and its neighbor spheres and (b) Parameters used for overlapping and non-overlapping ratio calculations.	63
Figure 3.8 : Generation of a CAD foam model by spherical ensemble approach.	65
Figure 3.9 : A close view of the CAD model of a sample porous structure.	66
Figure 3.10 : An example of nanoporous models with different porosities (a) 66% porosity, (b) 70% porosity and (c) with 72% porosity.	67
Figure 3.11 : Sectioning characterization of nanoporous samples at different sections.	68
Figure 3.12 : (a) Boundary conditions applied on the specimens and (b) Classical continuum stress-strain relationships where P , A_0 , L_0 are total cross-sectional force, cross-sectional area and length of the specimen, respectively. σ , ϵ and E are stress, strain and Young's modulus, respectively.....	70
Figure 3.13 : (a) Stress-strain curves for nanoporous aluminum with various porosities; (b) postpeak tangent modulus as measured from the ultimate stress point of the corresponding stress-strain curve in (a).	72
Figure 3.14 : Local von Mises stress field during tensile loading of nanoporous -Al structure with 72% porosity at (a) 1% strain level, (b) 5% strain level, structure with 78% porosity at (c) 1% strain level and (d) 5% strain level.	73
Figure 3.15 : Local stress distributions of the structures with 72% and 78% porosities at 5% strain level.	75
Figure 4.1 : (a) TEM image of a multiwalled carbon nanotube and (b) Schematic of a multiwalled carbon nanotube.	82
Figure 4.2 : Visualization of tensile loading of a single-walled carbon nanotube by TEM (a-d) Tensile deformation of a SWNT at high temperature. Kinks are showed by arrowheads. (e-g) Tensile loading of a SWNT with initial length of 75nm (e) at room temperature, (f) length after elongation, (g) length at the failure which is 84nm.	84
Figure 4.3 : Uniaxial compressive loading of a SWNT with 6nm length, 1nm diameter and armchair chirality of (7,7).....	86
Figure 4.4 : (a) HREM image of kinking formation of a MWNT with 8nm diameter and (b) Atomic configuration of a SWNT with a single kink formation simulated under bending loads.	86
Figure 4.5 : Bending of multi-walled CNTs exhibiting rippling modes of deformation.	87

Figure 4.6 : Images of CNT aerogels: (a) Macroscopic pieces of 7.5 mg mL ⁻¹ CNT aerogels, (b) Three polyvinyl alcohol (PVA) reinforced aerogel pillars supporting 100g, (c) SEM image of open porous structure of aerogel and (d) TEM image of CNT aerogel.....	88
Figure 4.7 : (a) Line segment representation of CNT, (b) Minimum distance between CNTs by using line segment representation.	93
Figure 4.8 : Segmentations of line segments by dividing the segment domain by the number of cross-links which is four in this example.	94
Figure 4.9 : Process of placing CNT candidates into the design space : (a) Rotation of the candidate CNT in library, (b) Target CNT in the design space waiting for intersecting CNT coming from library and (c) Design space after translation.....	95
Figure 4.10 : 2-D network samples with increasing number of CNT units.....	98
Figure 4.11 : 2-D network sample showing different junction types and spot areas.	99
Figure 4.12 : (a) Top view of a welded 2-D network, (b)-(c) Junctions formed after annealing.....	100
Figure 4.13 : (a)Perspective view of a 3-D CNT network, (b-c) Snapshots of junctions.....	101
Figure 4.14 : Example of junctions throughout 3-D CNT network.	102
Figure 4.15 : (a) Atomistic view of 2-D network, (b) Surface CAD drawing view of atomistic model and (c) Equivalent FE model of the atomistic model.	103
Figure 4.16 : (a) Distribution of the number of target CNTs which are completely cross-linked by 4 CNTs for 100 samples, (b) Distribution of acute angles (in degree) between cross-linked CNTs in a single sample of network.	104
Figure 4.17 : Distribution of distances between cross-links on the same CNT for one of the sample network.....	105
Figure 4.18 : (a) Distribution of mean values of cross-link angularity through 100 samples and (b) Distribution of mean values of cross-link distances through 100 samples.....	106
Figure 4.19 : CNT network samples with different cross-link densities, (a) 5 cross-links and (b) 7 cross-links per CNT.....	107
Figure 4.20 : Several instances of CNT network specimen with cross-link density of 7 at different time points in tensile loading simulation.	109
Figure 4.21 : Stress-strain curves of CNT network specimens under tensile loading with different cross-link densities.....	111
Figure 4.22 : Stress-strain curves of CNT network specimens under tensile loading with different cross-link densities.....	113
Figure 4.23 : Several instances of CNT network specimen with cross-link density of 6 at different time points in shear loading simulation.	114
Figure 4.24 : Stress-strain curves of CNT network specimens under shear loading of the specimens with the cross-link densities of 5 and 6.....	115
Figure 4.25 : Linear elastic regime of stress-strain curves of CNT network specimens under shear loading with different cross-link densities. ..	116
Figure A.1 : Workflow for generation of randomly intersected sphere network....	141
Figure A.2 : Workflow for the generation of CNT network.....	143

MECHANICS OF NANOMATERIALS CONSISTED OF RANDOM NETWORKS

SUMMARY

In the field of nanotechnology, nanomaterials with morphological features on the nanoscale have caught the interest of researchers all around the globe. One class of these materials which are known as carbon nanotubes (CNTs) is one of the extraordinary nanomaterials that are promising candidates for thermal, electrical and structural applications due to their unique properties. Since their discovery by Iijima (1991), thousands of studies, so far, have been adopted to their exceptional high strength and unusual electrical and thermal properties, displaying the desirable nature of their multifunctional capability. In the last years, the usefulness of the CNTs has been enormously extended by their use as CNT networks through which the CNTs are self-intersected in two or three dimensional space.

Nanoporous materials with morphological features at the nanoscale have the potential to be employed as sensors, actuators, insulators, electrodes, energy absorbents and also for adsorption and separation in recent years. The interest in studying this class of materials derives from their characteristic high surface-to-volume ratio. In many of the applications such as actuators, their mechanical properties are a prerequisite. For example, as actuators, these materials need to withstand coarsening and sintering. The mechanical strength of nanoporous materials has been studied through different experimental techniques such as nanoindentation, beam bending and micro column compression tests.

Due to their random complex structures, randomly structured nanomaterials are challenging to be modelled and tested numerically. In the proposed thesis, stochastic methods have been developed to build up numerical models of nanomaterials that are structured randomly organized nanoscale features such as CNT networked and nanoporous materials. By using the stochastic methods, sample models for CNT networks and nanoporous materials have been generated and tested numerically to show the validity of the stochastic methods and the models generated by them. Furthermore, generated models have been employed as test specimens within molecular dynamics simulations to investigate mechanical properties of CNT network and nanoporous materials.

Both CNT networks and nanoporous materials are examples of random networked nanomaterials. CNT networks consist of randomly oriented and cross-linked carbon nanotubes. Nanoporous materials, in a similar way, are built up by randomly oriented ligaments which are interconnected at junctions. Therefore, both CNT network and nanoporous materials can be considered as randomly organized materials which are the subjects of this study.

In the content of this thesis, stochastic models have been developed for random natured nanomaterials such as CNT network materials and nanoporous materials. For

this purpose, regarding CNT networked materials, a quasi-random self-intersected CNT network generation algorithm that enables the control of behavior decisive parameters, such as CNT length scale, density of junctions and relative angular position, has been presented and several sample networks with different parameters mentioned above have been generated. Following the generation of a CNT network in which the CNT units are so close together that heating to certain temperatures can yield a covalently bonded network, molecular dynamics (MD) simulations have been carried out to obtain bonded networks. As a result, parameter-controlled covalently bonded CNT network models were able to be employed within numerical simulations to investigate mechanical, thermal and electrical properties of CNT networks and their co-operating systems (i.e., nanocomposites) for the future studies.

Within stochastic method that has been developed for the CNT network modeling, in order to save computational time, the CNTs are represented by 3-D line segments passing through the central points of the CNTs cylindrical geometry.

The atomistic modeling of the nanoporous structures within the proposed thesis study has been based on an earlier work used to model microcellular carbon foams. The models have been constructed by initially creating randomly generated spheres that overlap with each other. After generating enough spheres to cover the desired model space, the final atomistic model for the nanoporous structure has then been obtained by deleting from a pristine block the atoms lying within the spheres. In order to control certain aspects of the topography of the nanoporous structure such as porosity and ligament size, the following parameters were designed to be adjustable in the random sphere generation algorithm: (1) range of the size of spheres to be generated, (2) range of overlapping ratios see below (3) minimum nonoverlapping ratio, and (4) minimum number of spheres intersecting with any single sphere. Here the overlapping ratio is defined as the ratio of the distance between the centers of two overlapping spheres and the sum of their radii. The non-overlapping ratio is defined as the ratio of the distance between the centers of two non-overlapping spheres and the sum of their radii.

The general idea behind creating the porous topology is deleting the atoms that fall inside certain regions within a pristine solid block. These regions are defined by first interconnecting a “target sphere” with randomly chosen number of “neighbor spheres”. The neighbor spheres then become the target sphere and each of these spheres is interconnected with its neighbor spheres. In this way, a network of interconnected spheres is generated. Atoms that fall inside the regions defined by these spheres are deleted and what are left behind are the atoms that form ligaments of the open celled nanoporous structure. One of the restrictions to follow when generating these spheres is that the neighbor spheres from the same target sphere cannot overlap each other. The distance between the centers of the two neighbor spheres can be adjusted by controlling the “non-overlapping ratio”, which is defined as the ratio between the distance of two non-intersected spheres and sum of the radii of these two spheres. Another important parameter that influences the overall porosity of the structure is the “overlapping ratio” between a target sphere and one of its neighbors. This is defined as the ratio of the distance between the center of the two spheres and the sum of their radii.

Numerical atomistic models, which have been generated by the stochastics algorithms, developed for nanoporous and CNT network materials have been employed in molecular dynamics simulations to test the mechanical behavior of

numerical specimens under tensile loading. In a classical MD simulation, the Newton's equations of motion are solved to obtain the temporal and spatial trajectories of atoms, where the force field interactions between the atoms are described by interatomic potentials derived from quantum mechanical based calculations. In this way, the state of the atomistic system at any future time can be predicted from its current state in a deterministic way. The MD method is based on the assumption that atoms behave like classical particles whose trajectories are governed by Newton's equations of motion. With more accurate interatomic potentials that are obtained by first-principles quantum mechanical (QM) calculations, engineering properties of nanomaterials obtained through MD simulations become more faithful and practical. The widely-used MD code LAMMPS (Large-scale Atomistic/Molecular Massively Parallel Simulator) developed by the DOE Sandia National Laboratories has been employed to perform MD simulations on the numerical specimens. The well-tested adaptive intermolecular reactive empirical bond order (AI-REBO) interatomic potential has been employed to model the interaction among carbon atoms in CNT networks while Embedded Atom Method (EAM) potentials have been utilized for the MD simulations of nanoporous materials.

At the first stage of the proposed study, algorithms of stochastic models for various nanostructures (i.e., CNT networks and nanoporous materials) have been developed, which enabled us to generate random natured nanostructures while having control on the behavior decisive geometric parameters of the corresponding morphology. Then, the algorithms have been implemented in Matlab environment to generate random atomistic models of proposed CNT networks and nanoporous materials. Sample atomistic models have been presented to demonstrate the applicability of developed algorithms in further computational studies.

At the second stage, generated atomistic models of CNT networks and nanoporous materials with different morphologic parameters have been employed in MD simulations to investigate their mechanical behavior subjected tensile loading. In this regard, atomistic nanoporous specimens with different porosities and different ligament shapes/sizes have been tested numerically under mechanical loading (i.e., tensile loading). By this way, effects of porosity, which is one of the controlled parameter, on the mechanical behavior of nanoporous materials have been studied quantitatively. As a result of MD simulations, it has been shown that basic mechanical properties such as the Young's modulus, yield and ultimate strength values of nanoporous materials increases as the porosity decreases. In addition to that, it has been also demonstrated that softening rate values after the peak stress on the stress-strain curves for the specimens with higher porosities have been shown to be slower than the specimens with lower porosities. Detailed evaluation of these findings considering the deformation mechanisms underlying these differences has been also provided. Along the same line, random CNT networks generated by the stochastic method have been used as atomistic models in the MD simulations to determine the effect of network parameters such as cross link density on the mechanical behavior under tensile and shear loadings. It has been shown that as the number of cross links per CNT increases, mechanical properties including elastic modulus, yield and tensile strength values. The results obtained from numerical tests performed by the MD simulations have been compared with the experimental results or if-exists numerical results in the literature. Furthermore, basic deformation

mechanisms of CNT network materials under tensile and shear loading have been investigated thoroughly by tracing out the MD simulation snapshots.

RASTGELE AĞ YAPILI NANO MALZEMELERİN MEKANIĞI

ÖZET

Hızla gelişen nanoteknoloji alanında nano ölçekteki morfolojik özellikler ile nano malzemeler pek çok araştırmacının ilgi odağında olma özelliği kazanmıştır. Nano malzemelerin bir çeşidi olan karbon nanotüpler ıslı, elektrik ve yapısal özelliklerini itibarıyle pek çok potansiyel uygulama alanı bulunan sıra dışı nano malzemelere verilebilecek en popüler örneklerden biri olarak gösterilebilir. İjima tarafından 1991 yılındaki keşfedilmesinden sonra karbon nanotüpler üzerinde binlerce akademik çalışma yapılmış ve olağanüstü yüksek dayanımı, sıra dışı elektriksel ve ıslı özelliklerinin bir arada olmasından ötürü çok fonksiyonlu kullanılabilme kapasitesi üzerinde durulmuştur. Özellikle son yıllarda karbon nanotüplerin birbirleriyle 2 veya 3 boyutta kesişmelerinden ibaret olan karbon nanotüp ağ malzemelerin ortaya çıkmasıyla karbon nanotüplerin makro ölçekteki uygulama alanları daha da genişletilmiştir.

Nano gözenekli malzemeler de nano ölçekte sahip oldukları yapısal özellikler sebebiyle nano malzemelerin ilgi toplayan bir başka çeşidi olarak gösterilebilir. Nano gözenekli malzemeler sensör, eyleyici, yalıtıcı, enerji emici, elektrot ve hatta soğurucu (adsorption) ve ayırıcı (separation) olarak kullanılma potansiyeli taşıyan malzemeler olarak son yıllarda ön plana çıkmıştır. Bu malzemeler üzerinde yoğunlaşan ilginin temelinde nano gözeneklerinden kaynaklanan yüksek yüzey/hacim oranı yattmaktadır. Bu nedenle bu malzemeler üzerinde yapılacak çalışmalarda nano gözenek yapısının doğru olarak modellenmesi çok önemlidir. Bununla beraber, eyleyici olarak kullanılması gibi pek çok uygulamada bu malzemelerin mekanik özellikleri büyük rol oynamaktadır. Nano gözenekli malzemelerin mekanik dayanımları nano çentikleme, kırış eğilmesi, mikro kolon basma testleri gibi farklı deneysel yöntemlerle incelenmiştir.

Rastgele dağılımlı yapıdaki nano malzemeleri sahip oldukları karmaşık rastgele yapıları dolayısıyla hem modellenmesi hem de numerik olarak test edilmesi oldukça zor malzemelerdir. Bu doktora tezinde, rastgele yapısal birimlerden oluşan nano malzemelerden karbon nanotüp ağ yapılı ve nano gözenekli malzemelerin rastgele yapılarının sayısal modellenmesi için gerekli yöntemlerin geliştirilmesi amaçlanmaktadır. Ayrıca, bu yöntemler kullanılarak üretilen sayısal test numuneleri kullanılarak rastgele modellerin geçerliliğinin gösterilmesi adına moleküler dinamik (MD) metodu kullanılarak sayısal benzetimler uygulanmıştır. Bununla beraber, mekanik davranışlarının incelenmesi maksadıyla her iki malzeme tipi için farklı özelliklerde üretilen test numunelerinin MD yöntemiyle çekme yükü altındaki davranışını incelenmiştir.

Karbon nanotüp ağ malzemeler, rastgele oryantasyona sahip karbon nanotüplerin birbirleriyle kesişmelerinden oluşan malzemelerdir. Benzer şekilde, nano gözenekli malzemeler de rastgele konumlanmış kırışların kesiştiği nano kırış ağı şeklinde yapılmıştır. Dolayısıyla hem karbon nanotüp ağ malzemeler hem de nano

gözenekli malzemeler rastgele yapılı nano malzemeler sınıfında değerlendirilebilirler. Rastgele dağılımlı yapısal birimlerden oluşan karmaşık geometrili bu malzemelerin sayısal olarak modellenebilmeleri için yapıldaki rastgeleliğin elde edilebilmesi adına özel algoritmaların geliştirilmesine ihtiyaç duyulmaktadır.

Bu tez kapsamında, yukarıda bahsedilen ihtiyaç doğrultusunda rastgele tabiatlı nano malzemelerden olan karbon nanotüp ağ yapılı ve nano gözenekli malzemelere ait rastgele sayısal modellerin oluşturulmasını sağlayan yöntemler geliştirilmiştir. Bu kapsamında, karbon nanotüp ağ yapılı malzemeler için bazı parametrelerin kontrol altında tutulabildiği karbon nanotüplerin birbiriyle rastgele olarak kesiştiği bir ağ yapısının oluşturulabildiği bir algoritma geliştirilmiştir. Bu algoritmda karbon nanotüp uzunluğu, karbon nanotüp kesim yoğunluğu ve görelî açısal konum gibi davranışları etkileyebilecek topolojik parametreler kontrol altına alınmıştır. Farklı parametreler kullanılarak elde edilen ağ modelleri tez kapsamında sunulmaktadır. Oluşturulan karbon nanotüp ağ yapılı modeller kullanılarak bir sonraki adımda moleküler dinamik simülasyonları vasıtasiyla kesim bölgelerinde lokal olarak uygulanan ısıtma işlemi neticesinde karbon nanotüpler arasında kovalent bağlar oluşturulmuş ve bir nevi lokal ıslık kaynağı yapılmıştır. Sonuç olarak kovalent bağlarla birbirine bağlı karbon nanotüplerden oluşmuş rastgele tabiatlı ağ malzemesi elde edilmiştir. Bu sayısal modeller söz konusu malzemenin mekanik, ıslık ve elektrik gibi özelliklerinin incelenmesi adına gelecekteki çalışmalarında kullanılabilecek niteliktedirler.

Karbon nanotüp ağ yapılı malzemelerin rastgele sayısal modelinin oluşturulmasında hesaplama zamanını düşürmek amacıyla karbon nanotüpler 3 boyutlu doğru parçaları olarak modellenmiştir. Söz konusu doğru parçaları silindirik hacimli karbon nanotüplerin merkez noktalarını birleştiren eksenden geçecek şekilde oluşturulmuştur.

Diğer yandan, nano gözenekli malzemelerin modellenmesi için geliştirilen yöntemde ise daha önce mikro gözenekli karbon köpüklerin modellenmesinde kullanılan yaklaşımından yola çıkmıştır. Bu kapsamında ilk adımda birbiriyle belirli oranlarda rastgele doğrultularda kesişen küresel hacimler topluluğu oluşturulmuştur. Oluşturulan küresel hacimler topluluğunun büyülüüğü elde edilmek istenen nano yapının ölçülerinden daha büyük olması gereğinin altı çizilmelidir. Yeteri kadar büyük, birbiriyle kesişen küresel hacimler topluluğu elde edildikten sonra elde edilmek istenen atomik kafes parametresine sahip malzeme bloğundan küresel hacimler içerisinde kalan atomların silinmesi suretiyle nano gözenekli yapı elde edilmiş olur. Boşluk oranı ve kırış boyutları gibi malzeme davranışını etkileyebilecek parametreleri kontrol edebilmek adına rastgele kesişimli küresel hacimler topluluğunun oluşturulması için geliştirilen algoritmda bazı değişkenler kısıt altına alınarak kontrol edilmiştir. Kısıt altındaki bu değişkenler şöyle sıralanmıştır: (1) kürelerin çap değişim aralığı, (2) kürelerin kesişme oranı aralığı, (3) aynı küre üzerinde kesişmeyen küreler arasındaki minimum mesafe oranı, ve (4) aynı küre ile kesişme halindeki minimum küre sayısı. Bu değişkenlerden kesişim oranının hesaplanmasında kesişen iki kürenin merkezleri arasındaki mesafe ile yarıçaplarının toplamı arasındaki oran kullanılır. Benzer şekilde (3) no.lu değişken olan kesişim yapmayan küreler arasındaki minimum mesafe oranı küreler arasındaki mesafe ile küre yarıçaplarının toplamı arasında yapılır.

Nano gözenekli yapıların sayısal modellenmesindeki genel yaklaşım belirli bir kafes sistemi parametresine göre oluşturulmuş katı bir hacimsel blok malzemeden, belirli küresel hacimler içerisinde kalan atomların silinmesi şeklindedir. Bu küresel hacimler, “hedef” küreler üzerinde birbirleriyle kesişmeden, sadece hedef küre ile kesişen “komşu” kürelerin yerleştirilmesi ile oluşturulmaktadır. Herhangi bir hedef küre üzerine yerleştirilecek maksimum sayıda komşu küre oluşturulduktan sonra yeni bir hedef küre seçilerek yeni seçilen hedef kürenin komşu kürelerle donatılması sağlanmaktadır. Eski komşu küre niteliğindeki kürelerin hedef küre nitelidine kavuşarak zincirleme etkiyle birbiriyle kesişen küresel hacimler topluluğu oluşturulmuş olmaktadır. Nihayetinde bu küresel hacimler içerisinde kalan atomların blok atom topluluğundan çıkartılmasıyla geride nano gözenekli yapının kırışları ve bu kırışların kesişikleri alanlar olan eklem bölgeleri ortaya çıkmaktadır. Kürelerin oluşturulurken kontrol altında tutulan kısıtlardan bir tanesi aynı hedef küre üzerindeki komşu kürelerin birbiriyle kesişmemesi hususudur. Bunu sağlamak için aynı hedef küre üzerindeki komşu küreler arasındaki mesafe kontrol altında tutulmaktadır. Kontrol altındaki bir diğer önemli parametre de boşluk oranını doğrudan etkileyen, hedef küre ile komşu küreler arasındaki kesişim oranıdır.

Rastgele yapıtı nano yapıların sayısal modelleri oluşturulduktan sonra klasik moleküler dinamik simülasyonlarında kullanılarak numerik modellerin mekanik davranışının incelenmesi yapılmıştır. Klasik moleküler dinamik simülasyonlarında Newton'un hareket denklemlerinin çözümü suretiyle atomların zaman ve lokasyon uzay yörüngeleri elde edilir. Bu esnada atomlar arasındaki etkileşimler kuantum mekanığı hesaplamaları veya tamamen empirik yöntemler ile oluşturulmuş atomlar arası potansiyeller vasıtıyla tanımlanmıştır. Bu şekilde belirli bir andaki atomların hızları ve konumları kullanılarak bir sonraki zaman adımlarındaki atom koordinat ve hızlarının elde edilmesiyle deterministik bir sistem çözülmektedir. Moleküler dinamik metodunda yapılan varsayılmış atomların, zaman ve mekan yörüngelerinin Newton'in hareket denklemleri ile belirlenen klasik parçacıklar gibi davranışasıdır. Birincil prensipli (first principle) kuantum mekanığı hesaplamalarına dayanarak elde edilen atomlar arası potansiyellerin kullanıldığı moleküler dinamiği simülasyonlarıyla sonucu elde edilen nano malzemelerin özelliklerinin güvenilirliği daha üst seviyededir. Bu çalışmada moleküler dinamik simülasyonlarında LAMMPS (Large-scale Atomistic/Molecular Massively Parallel Simulator) adı verilen ve USA DOE Sandia Ulusal Labaratuvar'larında geliştirilmiş açık kodlu ve akademik çevreler tarafından iyi bilinen bir kod kullanılmıştır. Karbon nanotüp ağ yapılarının simülasyonlarında AIREBO (Adaptive Intermolecular Reactive Empirical Bond Order) atomlar arası potansiyel olarak kullanılırken nano gözenekli malzemelerin analizlerinde ise gömülü atom metoduna (Embedded Atom Method, EAM) dayalı potansiyeller kullanılmıştır.

Bu doktora çalışmasının ilk aşamasında karbon nanotüp ağ yapıtı malzemelerin ve nano gözenekli metal malzemelerin rastgele yapıtı sayısal modellerinin oluşturulması için algoritmalar geliştirildi. Bu algoritmalar vasıtıyla rastgele tabiatlı adı geçen malzemelerin davranışlarını etkileyebilecek geometrik parametreler de kontrol altında tutulmaktadır. Daha sonra bu algoritmalar Matlab programlama dilinde kodlara dönüştürülerek karbon nanotüp ağ yapıtı ve nano gözenekli malzemelerin sayısal modelleri üretilmiştir.

Çalışmanın ikinci aşamasında ise birinci aşamada geliştirilen algoritmalar ile farklı morfolojik karakterde üretilen numerik test numuneleri moleküler dinamik simülasyonlarında kullanılarak mekanik davranışları incelenmiştir. Bu kapsamda,

farklı boşluk oranına sahip nano gözenekli test numuneleri kullanılarak MD yöntemiyle çekme yüklemesi altında test edilerek gerilme-birim şekil değiştirme eğrileri elde edilmiştir. Boşluk oranı azaldıkça makro gözenekli yapılarda olduğu gibi nano gözenekli yapıların Young modülü, akma ve çekme mukavemetlerinin arttığı gözlenmiştir. Bununla beraber, maksimum gerilmenin elde edilmesinden sonra gözlenen yumuşama (softening) hızının boşluk oranı arttıkça azaldığı ve belli bir boşluk oranında ise hızlı bir azalmanın olduğu görülmüştür. Yumuşama hızındaki bu ani değişikliğin nedenleri üzerinde durularak nano gözenekli malzemelerin çekme yüklemesi altındaki deformasyon mekanizmaları incelenmiştir. Benzer şekilde farklı kesim yoğunluklarına sahip karbon nanotüp ağ yapıları numuneler de numerik mekanik çekme ve kayma testlerine tabii tutulmuştur. Tek bir nanotüp üzerindeki kesim yoğunluğunun farklı olduğu sayısal numunelerin çekme ve kayma benzetimleri sonucunda gerilme-birim şekil değiştirme eğrileri elde edilerek kesim yoğunluğu arttıkça mekanik özelliklerde görülen değişiklikler gösterilmiştir. Elde edilen sonuçlar literatürdeki deneysel veya mevcutsa sayısal sonuçlarla kıyaslanarak değerlendirilmiştir. Ayrıca, çekme ve kayma yüklemeleri altında karbon nanotüp ağ yapılarının gösterdiği deformasyon mekanizmaları, MD benzetimleri sonucunda ayrıntılı olarak incelenerek arkasındaki sebepler üzerinde çıkarımlar yapılmıştır.

1. INTRODUCTION

Nanoscience and nanotechnology deal with ultra-small things that can be employed across all scientific disciplines such as chemistry, physics, materials science and engineering. Nanotechnology that is the ability of controlling the nanostructured phenomena to achieve a targeted end makes use of nanoscience which is the understanding of what the nanostructured item behaves.

According to many scientists, the lecture entitled as “There’s plenty of room at the bottom” given by Nobel Prize awarded physicist Richard Feynman is one of the milestones that stimulates the ideas behind the development of nanotechnology [1]. Due to unconventional nature of nano-scale world, disciplines that are differentiated on the continuum scale such as mechanics, materials science and physics are required to be synthesized on the same core to interpret mysteries of nano-scale world. At this point, nanoscience is the product of this multi-disciplinary approach to understand nano-featured processes and characteristics [2-4]. Exciting and highly accelerated progress that has been established in nanoscience is mainly because of recently developed capability of controlling and observing the structures at ultra small length and short time scales together with the highly-developed computational capabilities that can be utilized to realize numerical experiments.

One billionth of a metre, that is a nanometer (nm), can be approximately visualized in the minds by several comparisons. For instance, a sheet of paper is about 100,000 nanometers thick while a human hair is roughly 80,000-100,000 nanometers wide. As more examples, growth rate of human fingernails is at the order of 1nm per second and a DNA molecule is about 1-2 nm wide. In this regard, Figure 1.1 shows the relation between macro scale objects and nanoscale world on a scaled axis to show the transition from macro to nano. Materials at nano scale represent distinguishing chemical, mechanical, electrical and magnetic behaviors. Even though nanoscience appears as a new research area, nanomaterials have been used as early as medieval times. For example, more than thousands year ago gold nano particles were being added into ceramic porcelains to give red color by Chinese people.

Similarly, Roman glass makers were using metal nanoparticles to generate remarkably nice colors for decoration.

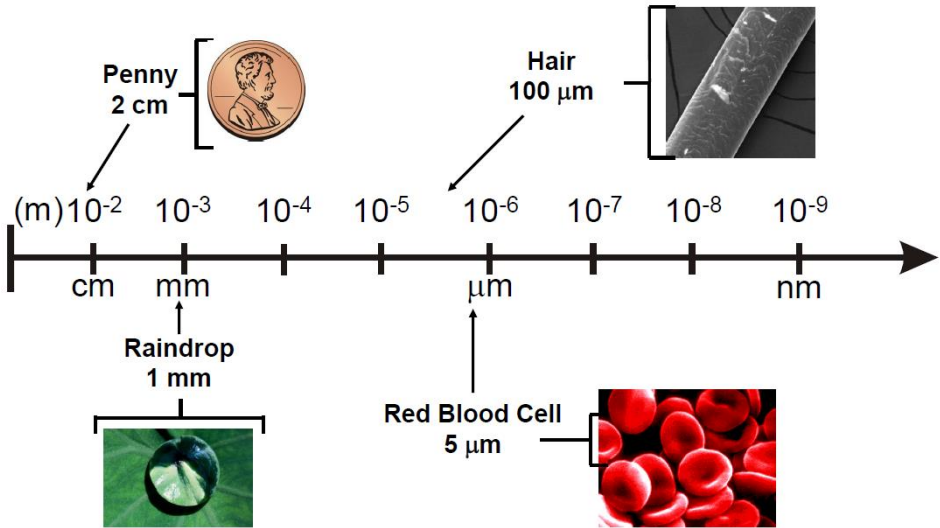


Figure 1.1 : From macro-materials to atom [3].

In many fields of nanotechnology, science of nanomaterials constitutes a basic building block for the further improvements and innovations. More specifically, mechanics of nanostructured materials is a very critical area to be understood due to the fact that many nanoscale phenomena such as folding of proteins that organize a living cell or the interaction of interfaces between nano-size crystals are controlled or governed by the mechanics at the nanoscale.

1.1 Nanomaterials

Applications of nanotechnology benefit from the extraordinary properties of nanomaterials which include at least one property-determining dimension smaller than 100 nanometer. In the meantime, nanomaterials, or in other words nanostructured materials consist of structural elements that are in the range of 1 to 100 nm, such as nano scale particles, tubes, fibres or rods, can also be thought as the main products of nanotechnology. One of the basic reasons behind the high interest in these materials by both academic and industrial environment in recent years is mostly because of incredible variation of properties observed at continuum and nano scales [3]. Due to these size-dependent intriguing properties, nanomaterials have great potential to create impacts in many fields, e.g., aerospace, medicine, electronics, etc.

While some of nanomaterials occur naturally (e.g., volcanic ash and soot from forest fires), many of nanomaterials can be classified into engineered nanomaterials that are designed to be manufactured and already being processed to commercial usage. Nowadays, we realize that many samples of nanomaterials have taken place in the products of cosmetics, sporting goods, stain-resistant clothing, tires, electronics, sunscreens and many other stuff that are being used in daily life [5]. Beside these, as medical applications, nanomaterials are utilized for the purposes of imaging, drug delivery and diagnosis.

Engineered nanomaterials represent the materials that are designed and manipulated at nano scale such that they gain novel properties compared with their bulk counterparts. Two major reasons can be pointed out explaining the different properties observed at nanomaterials designed at molecular level. One of these is substantial increase of the surface area due to existence of at least one nanoscale dimension in the topology of nanomaterials. Increase of surface area results in greater chemical reactivity of the structures, which in turn affects the mechanical, electrical and thermal behavior of the material. For example, sensitivity and sensor selectivity of chemical sensors can be increased by employing nanoparticles and nanowires due to high surface-to-volume ratio.

The other reason that can be used in the explanation of scale-dependent behavior is the quantum effect. At the atomic level, quantum effects play much more significant role in the extraordinary optical, electrical, mechanical and magnetic behaviors of nanomaterials. Traditionally, basic properties of materials such as the Young's modulus are measured by using macroscale or recently microscale test specimens, which results in no information up-scaled from nano scale. However, properties determined at macroscale do not predict the behavior of devices that are fabricated by continuously advancing nanomanufacturing techniques [6].

1.1.1 Applications of nanomaterials

Day by day, appearance of nanomaterials in commercial arena is increasing. Moreover, the range of available products comprises very large and different fields. Today, we can find nanomaterials in products of cosmetics, self-cleaning windows, wrinkle-free or stain-resistant textiles and in many other applications [5]. Nanocomposites and nanocoatings which include nanoscaled particles/fibres to

reinforce or change properties of overall bulk material are initiated to be exploited in variable products such as sports equipment, bicycles, windows and automobiles. For instance, on glass bottles, novel UV-barrier coatings are used to prevent sunlight damages on the beverages [3]. Tennis balls with much longer service life can be achieved by using butyl-rubber/nano-clay composites [3]. As another example, nanoscale titanium dioxide is employed in cosmetics, sun-protective creams and self-cleaning windows. Along the same line, nanoscale silica is finding applications as a filler material in cosmetics and dental operations [4].

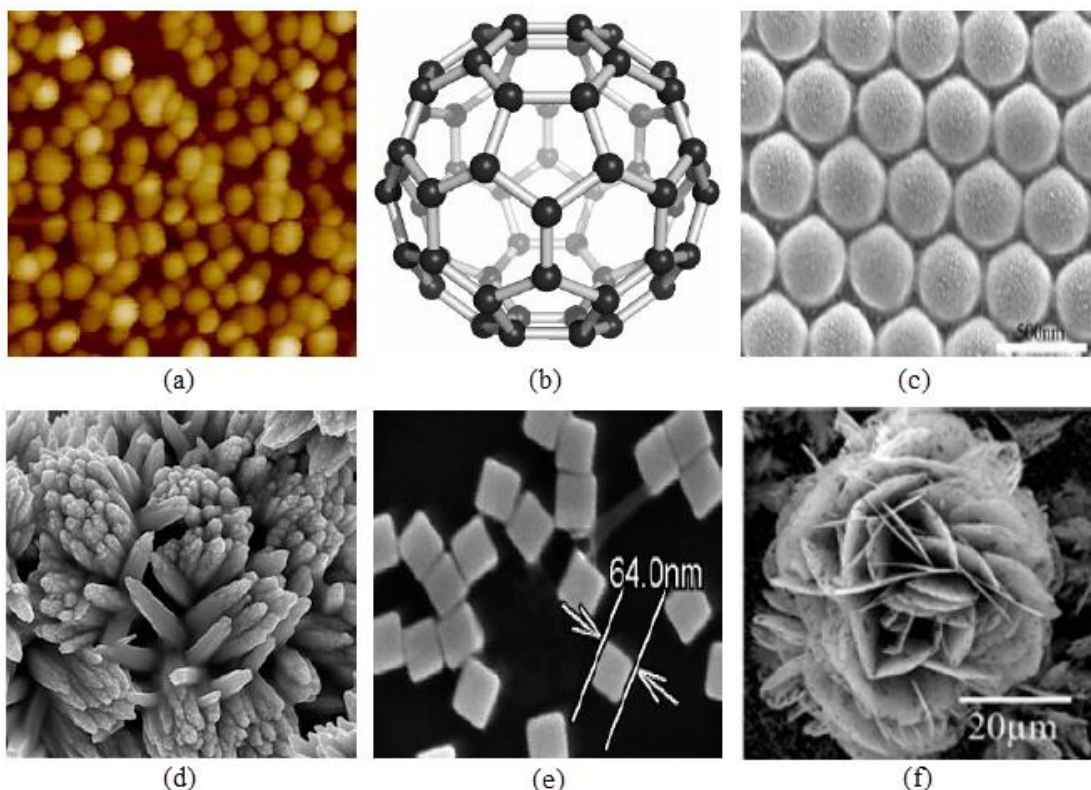


Figure 1.2 : Nanomaterials with different morphologies: (a) Au nanoparticle [2], (b) Buckminsterfullerene [1], (c) FePt nanosphere [2], (d) Titanium nanoflower [4], (e) Silver nanocubes [3], and (f) SnO₂ nanoflower [6].

Some more examples can be given explaining the high interest concentrated on nanomaterials due to their unusual mechanical, electrical, optical and magnetic properties [5]. For example, popularity of nanophase ceramics is mainly because of their higher ductility at extreme temperatures comparing to coarse-grained ceramics. Metallic nano powders are being used for the production of porous coatings as well as gas tight materials [7]. They are also good candidates for metal-metal bonding owing to their high valued cold welding properties in addition to their ductility. Remarkably high surface-to-volume ratio of nanoparticles leads to

extraordinary improvements of chemical catalysis. The range of potential applications of nanoparticles in catalysis is very broad to be from fuel cell applications to catalytic converters and photocatalytic devices [4].

Scientific interest on nanomaterials has begun in the 19th century despite the fact that nanomaterials already exist in the nature. Unquestionably, the most important stimulating factor leading the scientific research on nanomaterials is the development of high capability of microscopic devices that enable us to observe the nanoscale world [6]. In 1857, Michael Faraday's report on the colloidal gold particles can be shown as one of the first studies on nanomaterials [7]. On the other hand, investigations on the nanostructured catalysts have been in progress for approximately over 70 years. In USA and Germany, as a substitution of ultrafine carbon black for rubber reinforcements, fume silica nano particles were being manufactured in the beginnings of 1940's [8]. Extending the examples of applications of nanomaterials, nanostructured amorphous silica particles have also been used in many daily life products such as non-diary coffee creamer to automobile tires and catalyst supports [3]. In the 1960s and 1970s, magnetic recording tapes were developed to be produced by using metallic nanopowders. Granqvist and Buhrman published a new technique which is popular now, called the inert-gas evaporation technique to produce nanocrystals in 1976 [4]. Lately, the mystery of beautiful tone of Maya blue paint and its resistance to acidic environment has been explained by its hybrid nanostructure consisting of amorphous silicate substrate with inclusions of metal (i.e., Mg) nanoparticles [5].

By non-stop progress being achieved in nanotechnology, the number of nanostructured functional materials which permit altering of mechanical, electrical, magnetic, optical and electronic functions. Nanophased or cluster-assembled bulk materials are good examples of this kind of progress. Initially, discrete nano clusters/particles are manufactured at the first step and then these small particles/clusters are embedded into liquid or solid matrix materials [6]. As an example, nanophased silicon that is completely different from conventional silicon in physical and electrical properties can be employed in macroscopic semiconductor processes. In another example, conventional glass turns into a high performance optical medium presenting potential optical computational capability after being doped with quantized semiconductor colloids [9].

1.1.2 Classification of nanomaterials

As mentioned, nanomaterials are structurally organized at nanoscale such that at least one dimension is less than 100 nm. Nanomaterials can be classified according to the number of nano dimensions that form the nanostructure. In this regard, nanostructures such as nanofilms and nanowires are classified into 1-dimensional nanomaterials. Nano strands, tubes or fibres, on the other hand, are examples of nanostructures in two dimensions. In the same manner, nanoparticles, quantum dots and fullerenes are nano-structured in all three dimensions [10]. Figure 1.3 presents some visual examples for the classification based on the dimensions. Considering all, nanomaterials can be in different shapes such as spherical, tubular or irregular shapes in the form of singular, fused or agglomerated.

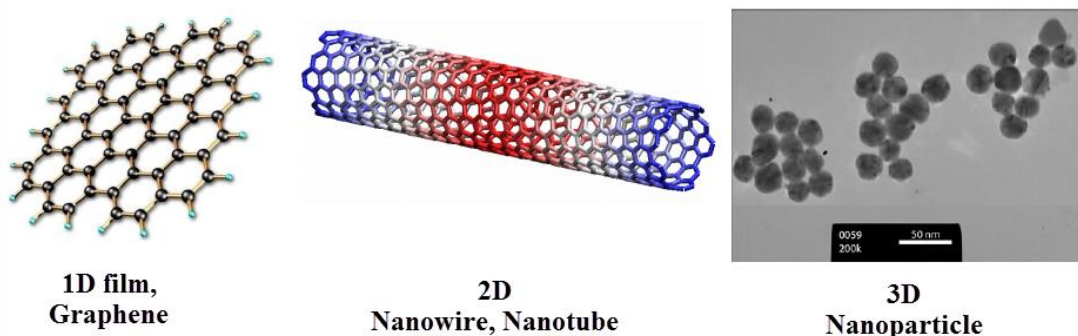


Figure 1.3 : Classification of nanomaterials [11].

Classifications on the nanomaterials can be also done on the basis of phase composition of nanomaterials. Single phase materials consist of only one ingredient such as crystalline or amorphous particles [9]. However, multi-phase nanomaterials are formed by more than one unit such as nanocomposites or coated particles. Merging of nanostructural units into existing bulk products results in enhancements of certain properties or opportunity of emerging new functionalities, e.g., higher strength or conductivity, improved heat or chemical resistance, etc.

1.1.3 Manufacturing of nanomaterials

Approaches on the manufacturing of nanomaterials are divided into two major branches which are bottom-up and top-down methods.

In the bottom-up approach that has been already known by chemists, nanostructured materials are constructed starting from the molecular level manipulations. Atoms and molecules are collected, combined or shaped by chemical and catalytic reactions to

form desired nanostructural units [12]. By employing AFM (Atomic Force Microscope) and using liquid phase techniques based on inverse micelles, bottom-up approach is being utilized by several nano scale manufacturing techniques such as chemical vapor deposition (CVD), laser pyrolysis and molecular self-assembly [10]. In this approach, atomic scale structural units, i.e., atoms, molecules or clusters, arrange themselves into more complex structural units similar to the growth of a crystal.

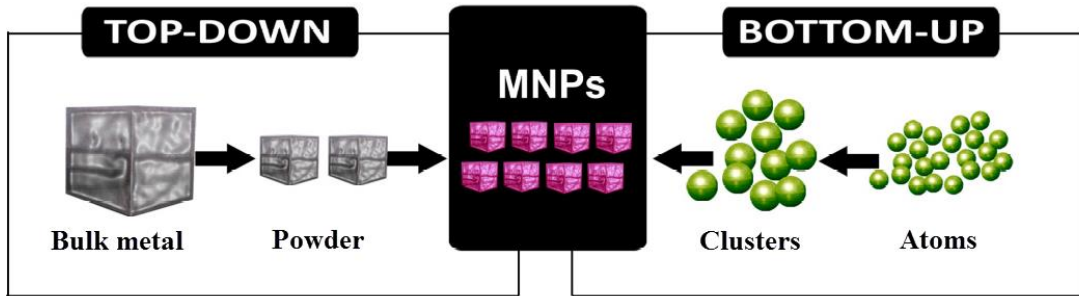


Figure 1.4 : Scheme of Top-Down and Bottom-up approaches to the synthesis of metal nanoparticles (MNP) [11].

Top down approach, on the other hand, constructs the nano-structured topology starting from the macro-level materials instead of molecular level. Therefore, in this kind of approach, traditional fabrication operations for manufacturing include cutting, carving and molding [13]. By this approach, exceptional machinery and electronic devices have been able to be fabricated. However, due to limitations on the size of cutting, carving and molding capabilities, the size of these devices cannot be downsized beyond a certain limit. Nano-lithography, laser ablation, physical vapor deposition, electrochemical method (electroplating), milling and hydrothermal technique are the examples of techniques that are based on top-down approach [14].

Nanomaterials that are sized in the order of that top-down production methods cannot deal with can be processed by bottom-up methods. Top down manufacturing of metal nanoparticles (MNPs) is an example for this situation. Because top-down methods can not yield uniform particles of very small sizes, bottom-up methods can provide uniform particles (Figure 1.4). Furthermore, some of the top-down techniques such as lithography cause formation of significant defects. For instance, on the surface of nanowires produced by lithography many impurities and structural defects are introduced. Because of the fact that the surface-to volume ratios of nanomaterials are very high, surface defects on the nanomaterials can cause

considerable change in the surface properties [11]. Despite this disadvantage, top-down engineering methods constitute an important place together with the bottom-up chemistry in the development of nanoscience and nanotechnology.

In the perspective of nanoscience, every element in the periodic table, depending on the desired target material, can be utilized in the manufacturing of nanomaterials. Increasing control on the manufacturing of single nanostructural units that are designed for specific purposes after their assembly into larger structures, nanotechnology will enable us to synthesize revolutionary materials. In this way, metals, ceramics or polymers can be manufactured in nano precision exactly without machining.

1.2 Introduction to Nanoporous Materials

Like the CNTs and CNT based materials, nanoporous (np) materials are also attractive research fields in nanoscience and nanotechnology. Nanoporous materials are generally characterized as nano scale solid materials that include porous topology in the length scales less than $1\mu\text{m}$ [12]. Materials categorized as np materials consist of nano scaled cellular structure through which open channels or empty spaces exist, which directly affect the behavior of np materials.

Large amount of nanoporous materials already exist in nature, especially in biological systems and in minerals. For example, walls of biological living cells are a kind of nanoporous membranes which include significant complexities due to their responsibilities in living organisms. Besides that, some of the nanoporous materials have found industrial applications for many years. Zeolites are the most known nanoporous material, which have been employed in petroleum industry as a catalyst for decades. Although the zeolites used in industry were natural, now most of them are synthetic. As the progress achieved in nanotechnology to manipulate and visualize objects at nanoscale, ability to control pore size of these materials at nanoscale has been increased. By this way, creation of nano membranes having controllable molecular structures with atomistic perfection can be realized. As the size and composition of the nanoporous structure can be modified, its physical and chemical properties can also be altered in a desired way.

Nanoporous materials show different functionalities according to the properties of nanopores such as their shapes, sizes and amounts. Conventionally, pores are defined as the voids or holes with different shapes (e.g., cylinders, balls, slits, hexagons, spheres, etc.) in a solid material. Pores may exist as isolated cells or interconnected with each other through holes on the cell walls.

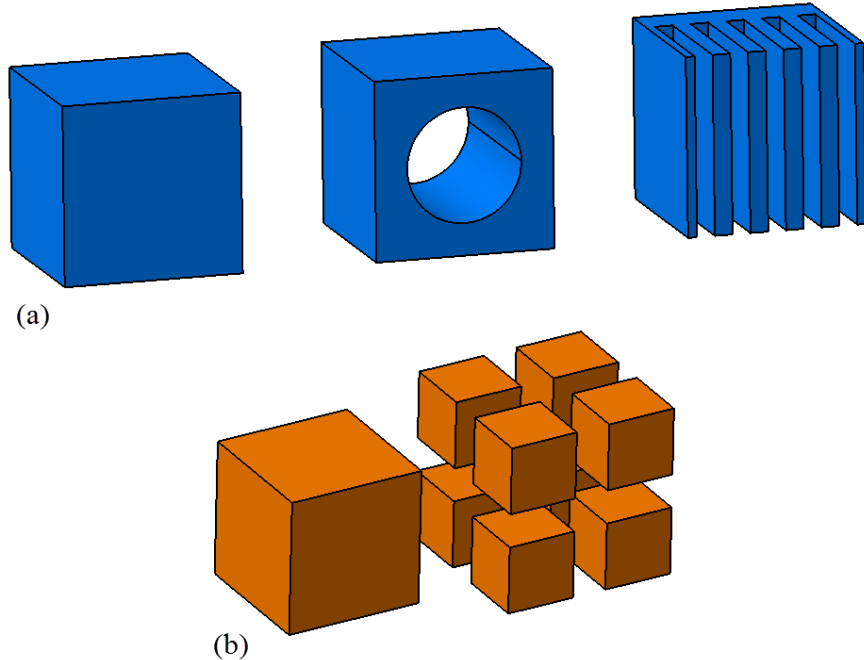


Figure 1.5 : Specific surface area enhancements: (a) Three blocks having the same volume initially but different surface areas due to different features, (b) Surface area increments by splitting a volume.

The most significant property of nanoporous materials is ultra high specific surface area which is defined as the ratio of surface area to mass. High surface area characteristics of nanoporous materials arises from nano scale topology which has nano scaled channels and pores [2]. The concept of increased surface area due to nano scaled topologic features is shown in Figure 1.5(a). Another way of increasing the specific surface area of a material is to divide it into tiny particles without decreasing the total volume.

Morphologies of the most of the nanoporous materials can be approximately simplified to doable geometries such as cylindrical hole in order to perform several analysis. According to the size of holes throughout the porous network, cellular materials can be classified as microporous if the hole diameter is less than 2nm; mesoporous if the diameter of the hole is between 2nm and 50 nm; and macroporous if the diameter is greater than 50nm [14]. This classification is made by the

international scientific community (The International Union of Pure and Applied Chemistry, IUPAC) to reach an agreement on the classification of pores. Figure 1.6 illustrates some examples regarding this classification. Furthermore, examples of microporous, mesoporous and macroporous materials are given in Table 1.1.

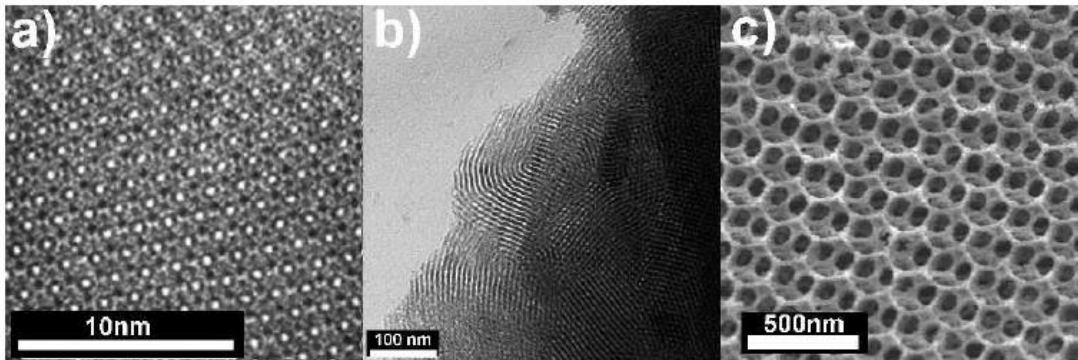


Figure 1.6 : Three different types of nanoporous silica materials. (a) A microporous material: zeolite, (b) A mesoporous material, (c) A macroporous material [13].

The existence of pores within a material brings extra useful properties that do not exist in the corresponding bulk material that do not have porous network. Porosity is defined as the ratio of the empty space to the total volume of the material and usually this value is between 0.2 and 0.95 for porous materials [15].

Table 1.1 : Examples of microporous, mesoporous and macroporous materials [16].

Microporous materials	Zeolite-like materials, activated carbon fibers (ACF), templated carbon from zeolites, metal organic frameworks (MOFs)
Mesoporous materials	Mesoporous oxides (silica, alumina, zirconia), MCM-41, CMK-1, polymeric materials
Macroporous materials	Porous glass, nanoporous silicon
Hybrid porous materials	Activated carbon (AC, silica gel, pillared clay, nanoporous oxide-bridged carbon nanosheet composites)

Pores within a porous material can be open or closed state. Open pores are an interconnected network of the pores, but in case of a closed pore system, pores are not interconnected with each other and at the isolated condition. Therefore, in applications such as catalysis, filtration and adsorption, porous materials with open pore architecture are much more favorable instead of porous systems with closed pores. On the other hand, closed pore systems are preferable in sonic and thermal insulation or lightweighted structural applications.

1.2.1 Properties of nanoporous materials

Due to their novel structural properties and large interconnected internal surface at atomistic scale, the usage of nanoporous materials as catalysts and absorption media is increasing day by day. Beside this, owing to their capacity to absorb and interact with atoms and molecules, porous materials have significant importance in nanoscience and nanotechnology [17].

Basic properties of nanoporous materials can be depicted as long as their microscale characteristics are understood. In this regard, atomistic simulations such as molecular dynamics simulations play an important role in supporting experimental studies.

As the porosity, pore size, pore size distribution and composition of nanoporous materials vary, their pore and surface properties also change that also cause changes in their potential applications. For different applications, a candidate material should satisfy different set of requirements. For instance, to be a good absorbent, a material should have several performance parameters such as high adsorption capacity, high selectivity, good mechanical properties and acceptable stability and durability. High adsorption capacity is mainly driven by the properties of specific surface area, chemistry of surface and pore size which dictate the amount of materials collected by unit mass of adsorbents. Similarly, selectivity property which is especially required in case of a target of separating a desired material from a multi-component mixture, depends highly on the pore size, shape and pore size distribution in addition to the type of adsorbates. The other required property is excellent mechanical properties which help absorbers to resist attrition, erosion and crushing in adsorption columns. In addition to these, due to abrasive chemical and thermal environments, stability and durability of absorbent materials are very critical to sustain their functionality in long terms. Several factors affect the degree of satisfying these requirements for nanomaterials such as manufacturing methods and processing conditions.

1.2.2 Major opportunities in applications of nanoporous materials

The main advantage of nanoporous materials is their cellular structure at the nano scale. Due to their porous nanostructure, they have a ultra-large surface area in addition to controllable cell size and morphology. As mentioned previously, because of their ultra-fine porous morphology, their material properties are superior in comparison with their bulk counterparts. For that reason, extraordinary properties of

nанопорous materials enable them potential candidates in wide range applications including photonic crystals, bio-implants, sensors and separators. Application areas of nanoporous materials can be divided into two categories in which nanoporous materials are employed as a bulk material form and membrane form. Generally separation related applications make use of membrane type nanoporous materials whereas bio-implants, sensors and photonic crystals are corresponding to the bulk nature of nanoporous materials.

The most exciting point of membrane-type nanoporous materials is due to their capacity of allowing certain sizes of objects to pass through the membrane while other objects cannot pass. As the size of the cells within the nanoporous membranes are controlled, control on the size of the objects that are targeted to eliminate can also be controlled. Zeolites which are crystalline porous materials are known to be one of the most popular nanoporous materials that have been used for separation purposes for a long time. As observed in zeolites, three dimensional cellular network structure of nanoporous materials offers very advantageous medium for selecting and separating different molecular types.

One of the most important feature of nanoporous materials is their ultra large surface areas as mentioned repeatedly in the text. Such a huge surface area results in high sensitivity to alterations in the environmental conditions such as temperature, light and humidity. Due to this advantage, nanoporous materials are widely used as sensors and actuators.

1.3 Introduction to Carbon Nanotubes

Carbon is the essential element of life, because of the fact that its organic compounds take parts in every living tissue. One of the reasons for its diversity in compounds is the reality that carbon atoms have the ability to combine with other carbon atoms as well as with other elements. Figure 1.7 shows the different structural forms of carbon in nature. Carbon nanotubes (CNTs) which are shown as the allotropes of carbon element are one of the fascinating examples of carbon based nanomaterials and can be considered of as the sheet of graphite (graphene) rolled up into a seamless molecular cylinder.

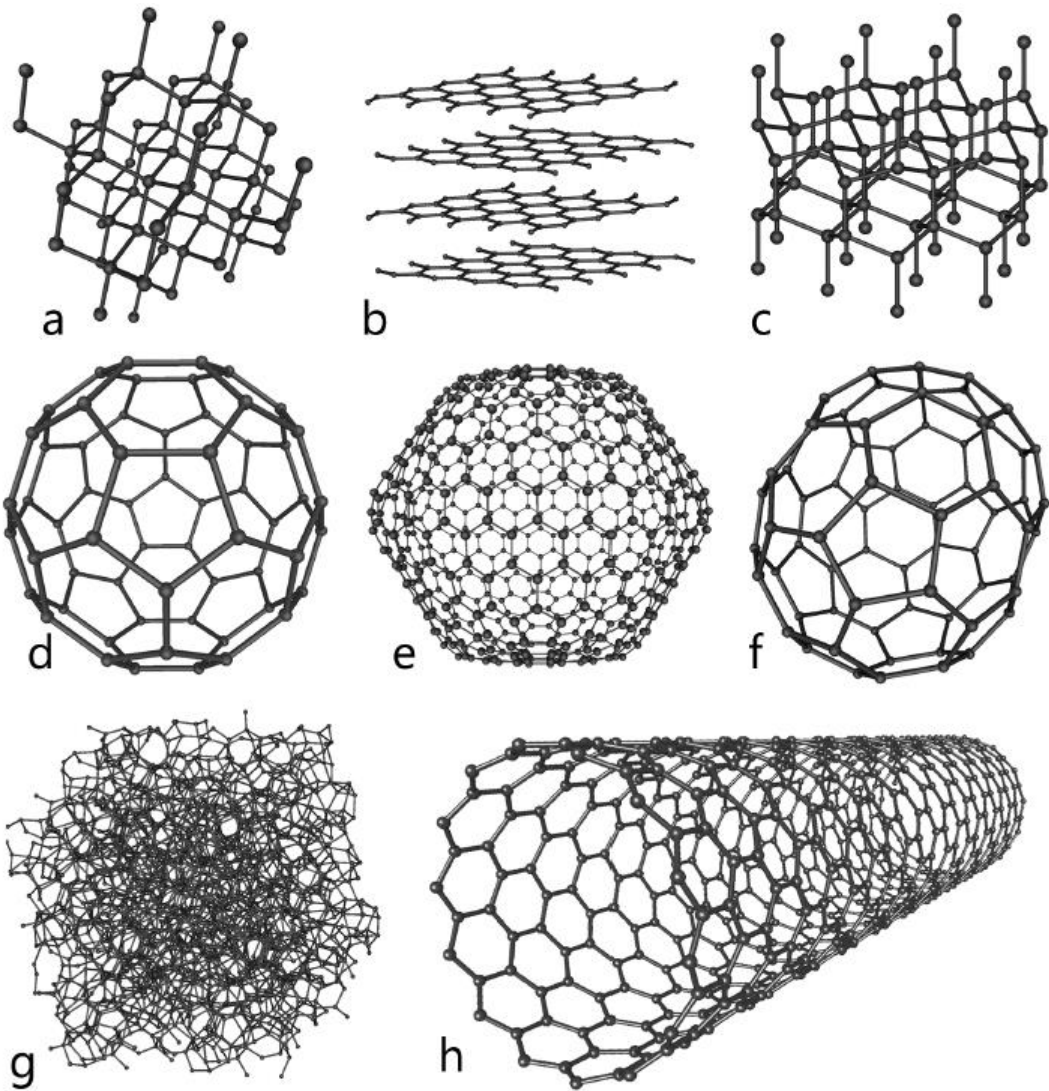


Figure 1.7 : Different structural forms of carbon element (a) diamond, (b) graphite, (c) Lonsdaleite (hexagonal diamoond), (d) Buckminster-Fullerene (C60), (e) C540, (f) C70, (g) amorphous carbon, (h) Nanotube [8].

The CNTs can have a length-to-diameter ratio greater than 106 making them an ultra high aspect ratio material. Their diameter varies between 1 to 100 nm with a length of up to several micrometers or even milimeters. The CNTs can be classified into two major groups as single-walled carbon nanotubes (SWNT) and multi-walled carbon nanotubes (MWNT). The SWNTs consist of only one layer of graphene sheet while the MWNTs can be considered as the rolled stack of several graphene sheets.

Although discovery of the SWNTs are undisputedly clear, discovery of the MWNTs is controversial. Regarding the SWNT, two papers [15,16] which were published independently in the same year (1993) introduced the SWNTs into the scientific research area. In case of the MWNTs, the first report giving the TEM images of nanodiameter carbon fibres was published by Radushkevich and Lukyanovich in

1952 in the Journal of Physics and Chemistry of Russia in Russian. Because of cold war, this report was not known by many scientists in the world. Therefore, many people consider Iijima's paper [17] published in 1991 as the first introduction of the MWNTs into the research community.

Bulk synthesis of the SWNTs is relatively more difficult than the MWNTs due to proper control requirement on the growth and atmospheric condition. Beside that catalyst is required for the synthesis of the SWNTs while not needed for MWNTs. Moreover, purity of the MWNTs are higher than SWNTs.

The CNTs are regarded as the one of the promising materials for the 21st century due to their exceptional physical properties. Owing to these novel properties, the CNTs have many potential applications in nanotechnology.

1.3.1 Geometry of CNTs

It is previously mentioned that the CNTs can be considered as the graphene sheets rolled up in the form of cylinder. Morphologies of the CNTs depend on the direction of the axis around which the graphene layer is rolled up (see Figure 1.8(a)). Two integers (n,m) called as chiral indices and are defined to indicate rolling direction, or in other words the chiral vector (\mathbf{C}_h). The chirality vector is extended from one carbon atom to another carbon atom which is crystallographically equivalent on graphene lattice. The chirality vector is defined as the linear combination of basis vectors \mathbf{a}_1 and \mathbf{a}_2 , i.e., $\mathbf{C}_h = n\mathbf{a}_1 + m\mathbf{a}_2$.

All physical properties of a given CNT is highly dependent on chiral indices. Depending on chiral indices, the CNTs are categorized into 3 classes which are shown in Figure 1.8(a). Two of them are highly symmetric zigzag and armchair CNTs in cases m is equal to zero and m is equal to n, respectively.

The circumference of a given CNT is determined by the length of its chiral vector. Therefore, the diameter of a CNT is given as

$$d = \frac{|\mathbf{C}_h|}{\pi} = b\sqrt{n^2 + nm + m^2} \quad (1.1)$$

where b is the lattice constant of the graphene honeycomb lattice which is equal to 2.49 Å. The translation vector shown in Figure 1.8(b) defines the periodicity of the lattice along the CNT cylinder axis.

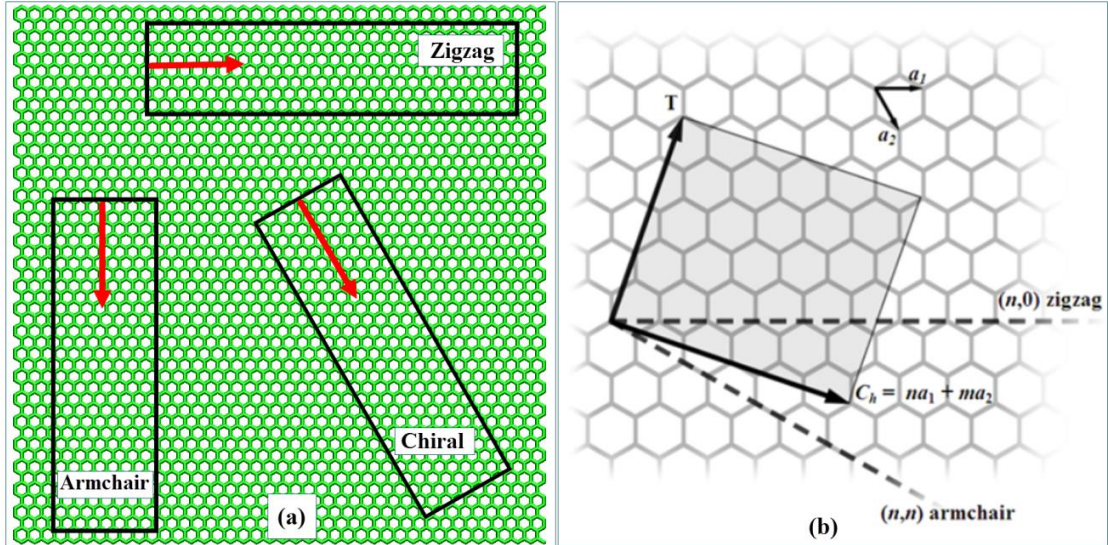


Figure 1.8 : (a) Different rolling directions on a graphene sheet causing different chiralities, (b) General geometric parameters for CNTs [18].

In a perfect CNT structure, all covalent bonds excluding the tip bonds are on the hexagonal lattice system. However, during the synthesis process, defects are formed and pentagonal, heptagonal bonds and other imperfections occur, which lowers the quality of the CNTs.

1.3.2 Manufacturing of CNTs

Several techniques have been used for the synthesis of carbon nanotubes including arc discharge, laser ablation, high-pressure carbon monoxide disproportionation (Hipco) and chemical vapor deposition (CVD). Processes for the generation of the CNTs in many of these methods are realized in a vacuum or with process gases. On the other hand, the CVD synthesis of the CNTs can be in vacuum or at atmospheric pressure. As the techniques used in catalytic or continuous growth processes are advancing, commercialization of CNT products becomes feasible.

The quality of the CNTs generated by catalytic techniques is not as good as the ones synthesized by the arc-evaporation method in which a catalyst is not utilized. However, despite this disadvantage catalytically manufactured CNTs have received great attention following Iijima's paper in 1991 [17] due to several reasons. The most important reason behind this popularity is the capacity of catalytic methods to produce scaled-up CNTs, in other words susceptibility of massive production. Therefore, bulk synthesis of the CNTs by employing catalytic methods is possible, which in turn creates popularity on them. Secondly, controlled growth of the CNTs on the target substrates can be managed by catalytic methods, which is highly

applicable especially in display technology. In this regard, the CVD is the dominant technique for the high-volume CNT production.

1.3.3 Applications of carbon nanotubes

Ranges of diameters for the SWNTs and MWNTs are usually 0.8 to 2nm and 5 to 20nm, respectively. However, sometimes diameters of the MWNTs can exceed 100nm. On the other hand, the maximum length scale of the CNTs starts from the values less than 100 nm and reach up to several centimeters which is the macroscale range [19].

The tensile strength value measured for an individual MWNT is 100 GPa which is 10 times higher than any industrial fiber. Depending on the chirality, the SWNTs can be metallic or semiconducting while the MWNTs are usually metallic and can carry currents up to 10^9 (A/cm^2). Beside this, thermal conductivity of a SWNT based on the wall area is around 3500 ($\text{Wm}^{-1}\text{K}^{-1}$) which is higher than the thermal conductivity of diamond [15].

Even though scientific research on the CNTs exploded in 1990s following the first industrial synthesis of CNTs, substantial growth in the commercial area has observed in the last decade. Following the year 2006, the capacity of CNT production has increased 10 times and growth of research study numbers on CNT related subjects continue [16].

Today, most of the CNTs which are bulk produced is employed in composite materials and thin films, and topology of these CNTs is randomly organized rather than being in a specific order. However, ordered CNT structures such as vertically aligned forests, yarns and sheets have very high potential to be used in shape recovery, dry adhesion, high damping, terahertz polarization, large stroke actuation and thermoacoustic sound emission [20-22].

It should be noted that CNT macrostructures such as yarns and sheets possess considerably lower mechanical, thermal and electrical properties than those of individual CNTs. Usage of the MWNTs are more favorable than the usage of the SWNTs where diameter and band gap of the CNTs are not so important, because of higher prices of SWNT production. The reason behind this higher cost is that synthesis of SWNT by the CVD needs to be controlled by tighter process parameters and high cost of research and development of process. Thus, the SWNTs that have

controlled the chirality can be favorably employed in the emerging applications if the prices can be cut down.

First usage of the MWNTs was in plastics as a electrically conductive filler due to their ability of forming a light percolated network with a 0.01 weight percentage. By using disordered MWNTs in polymers to form CNT-polymer composites, conductivity of overall composites can be increased to $10000\text{ (S m}^{-1}\text{)}$ at a weight percentage of 10. These electrically conductive light plastic composites are used in automotive industry to sustain electrostatic- assisted painting of mirror housings and also in the fuel lines and filters to ensure dissipation of electrostatic charge. These CNT polymer composites are also utilized in electromagnetic interference (EMI) shielding packages and wafer carriers in microelectronics industry [21].

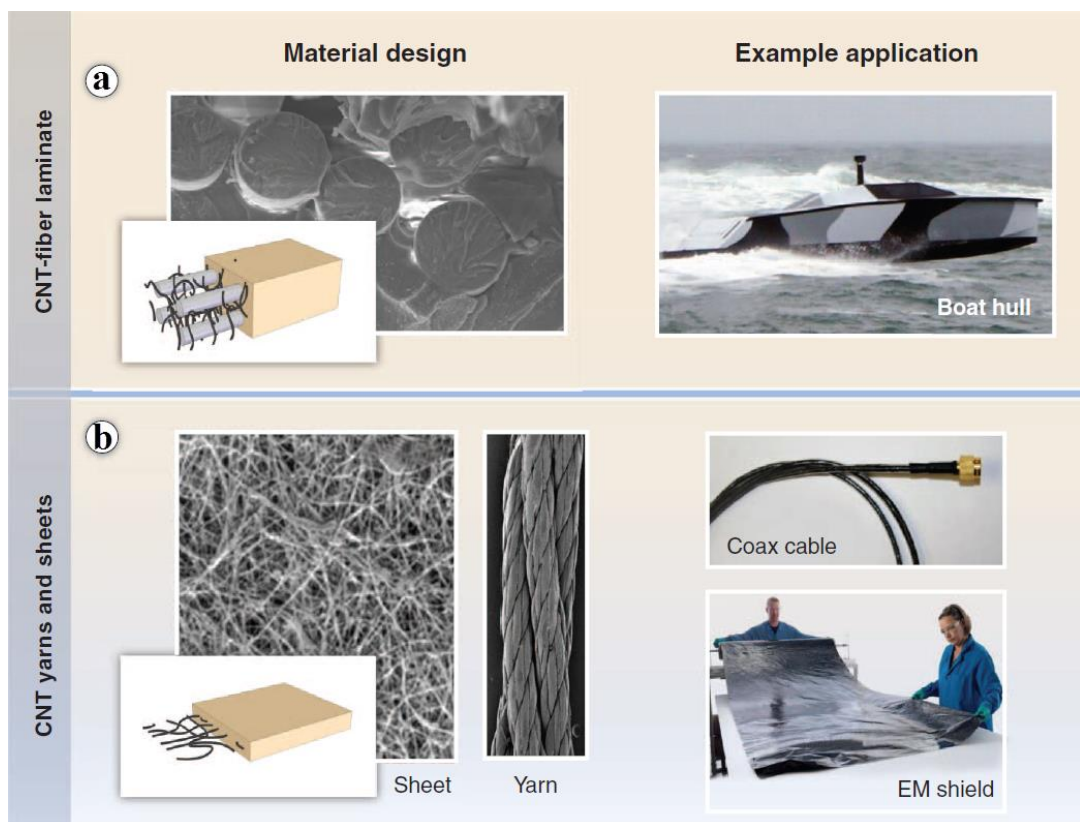


Figure 1.9 : CNT composites and macrostructures (a) Micrograph showing the cross section of a carbon fiber laminate with the CNTs dispersed in the epoxy resin and its application. (b) CNT sheets and yarns used as lightweight data cables and electromagnetic (EM) shielding material [23].

The CNT reinforced polymer composites are also used as a solution to lighweighted structural applications. For this purpose, the CNT powders are added into polymeric resins to elevate stiffness, strength and toughness properties effectively. For example, adding only approximately 1 weight percentage of the MWNTs into epoxy resin

improve the stiffness and fracture toughness by 6 and 23%, respectively [24]. In the meantime, this amplification does not yield any degradation on the other mechanical properties. The CNT reinforced composites can also present good damping characteristics due to stick-slip mechanisms between the CNTs themselves and the contact between CNT and polymer. Due to its enhanced damping capacity, the CNT composites are used to improve sporting goods such as tennis racquets, baseball bats and bicycle frames.

The CNT based resins are also utilized to upgrade fiber composites. This enhancement has recently been used for lightweight wind turbine blades and hulls of maritime boats. In this regard, Figure 1.9(a) shows a cross section of a composite fiber laminate that consists of dispersed CNTs in the epoxy resin and a sample application is given as maritime security boats of which boat hull is made by lightweighted CNT fiber reinforced composites [25].

For high technology applications where lightweight solutions together with multifunctional capabilities such as combined mechanical and electrical functionality are required, a serious competition is expected to be observed between the CNT yarns and laminated sheets produced by the direct CVD and carbon fiber (see Figure 1.9(b)).

1.4 Purpose of Thesis

The main purpose of this dissertation is mainly to develop efficient algorithms to generate representative atomistic models of randomly organized nanostructures which were selected as CNT network and nanoporous materials and to employ those atomistic models in molecular dynamics simulations for investigating the mechanical behavior of selected nanomaterials. Both CNT networks and nanoporous materials have complex geometries formed by random networks of carbon nanotubes and ligaments, respectively. Thus, generating their computational atomistic models is a very challenging issue that should be solved to realize numerical experiments. In this regard, as the first step of the dissertation, stochastic models have been developed for random natured CNT network materials and nanoporous materials. The other purpose of this dissertation is to open a way that other researchers can employ the algorithms that are developed within this study, in other studies for the investigation

of randomly organized nanostructures. In this perspective, it is aimed to develop tools or methods that can be used in future studies.

Due to lack of efficient algorithms that can be used in the modeling of randomly organized nanostructures, i.e., CNT networks and nanoporous materials, there are a few studies in literature regarding mechanics of these materials. Therefore, the other main purpose of this study is to examine mechanical behavior of CNT networks and nanoporous materials by using the atomistic models generated by the techniques which are developed in the first stage of the dissertation. In this perspective, the ultimate goal of this dissertation is to get deep understanding of the deformation mechanisms in CNT network and nanoporous materials. It is important to have essential information about the dependence of mechanical performance on the topological features, in order to manufacture outstanding novel materials. Therefore, in the scope of this dissertation, numerical experiments are conducted by molecular dynamics simulations to provide the relationship between topological parameters and mechanical properties.

2. OVERVIEW OF MOLECULAR DYNAMICS SIMULATIONS

As mentioned before in the previous chapters, molecular dynamics (MD) simulations have been utilized to investigate mechanical behavior of nanostructured materials in this dissertation. In this regard, this section presents an overview of molecular dynamics (MD) method and related subjects.

2.1 Introduction

Numerical experiments, namely computer simulations, are important tools, today, in scientific research and development efforts. In history, real experiments and theoretical work were the main frames escalating the progress in science. In an experimental study, the system under investigation is subjected to specific boundary conditions and measurement of parameters that are in question are obtained and numerically stored. In a theoretical work, a physical system is represented by governing mathematical equations consisted of driving parameters of the system. In order to validate the mathematical model formed in theoretical study, the stability or predictive capacity of the model should be shown by several simple cases that would allow solvable mathematical equations. However, for the sake of getting solvable mathematical equations, many times complexities of the system disappears which take us away from the real world problems.

Formerly, theoretical models were able to be examined only in limited special cases. For example, in condensed matter physics, intermolecular forces within a selected material could be justified in a diatomic molecule or in a perfect and infinite lattice crystal system. Even under the simplified conditions, further approximations were usually demanded to perform calculations. However, many of physical issues that fall into the both academic and practical interest, such as physics and chemistry of defects, surfaces, organic molecules and so on, cannot be simplified to be investigated by theoretical models.

High speed computers that appeared in the 50s introduced a new player, numerical experiments, in the scientific research area in addition to experiments and theoretical studies.

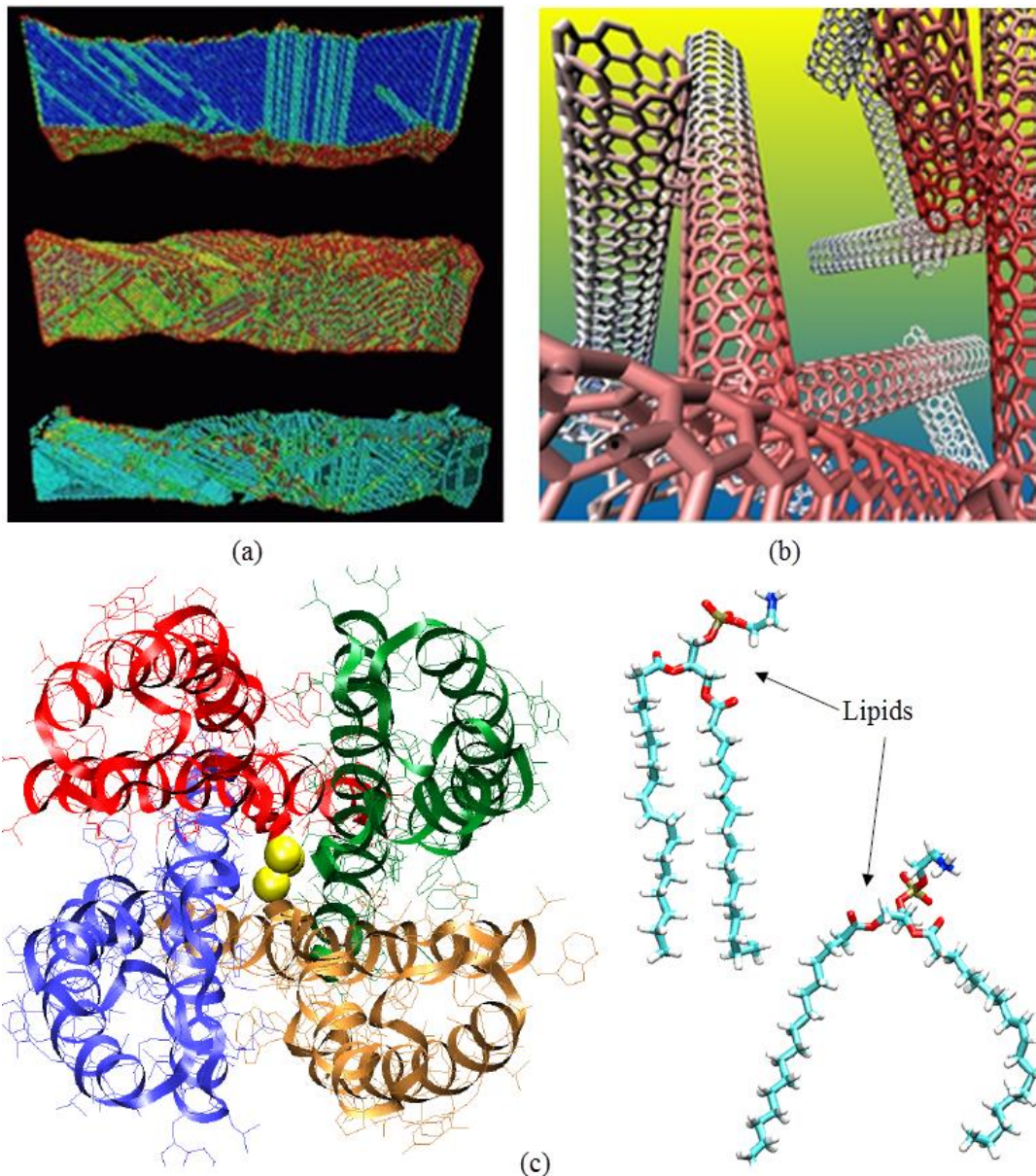


Figure 2.1 : Examples of nanostructures that can be simulated by MD (a) Nanowires, (b) Carbon nanotubes, (c) Bio-molecules [26].

In numerical experiments or in other words computer simulations, a theoretical model that governs the simulation still exists but the calculations are performed numerically by high speed computers under the framework of algorithms developed in an appropriate computer language. By numerical experiments, much more complicated phenomena can be injected into the numerical system, which guide towards investigations of more realistic systems. Numerical simulations conceptually

stand at a position between experiment and theory. The models employed in the computer simulations are just numerical models, not the real physical system, which translates the computer simulations concept towards theory. On the other hand, validation of a numerical model is much more like a real physical experiment in the way of evaluation of simulation results, which conveys the computer simulation concept towards experiments.

In the past, interactions between atoms were calculated by two-body potentials which have uncomplicated analytical forms, e.g., Morse or Lennard-Jones potentials. At present, however, many body potentials, which are obtained numerically by using forces anticipated by first-principle methods, are the examples of much more precise potentials.

Molecular dynamics (MD) method is a computer simulation method to obtain the time trajectories of an ensemble of atoms, which interact with each other, by performing numerical integrations of equations of motions. It is a very effective technique to investigate atomic scale and macroscale properties of nanomaterials such as nanowires, carbon nanotubes or bio-molecules as shown in Figure 2.1.

In MD simulations, atoms are considered as a point mass that are linked by springs. In this idealization, springs represent the bonds between atoms. Force fields, or in other words, potentials are utilized to obtain the time trajectory of atomic positions and velocities.

Molecular dynamics method utilizes the law of classical Newtonian mechanics, named as Newton's 2nd Law, for the derivation of equations of motion:

$$\mathbf{F}_i = m_i \mathbf{a}_i \quad (2.1)$$

Equation (2.1) is defined for each atom i that exists in an atomic system consisted of N atoms. In this equation, m_i is the atomic mass, $\mathbf{a}_i = d^2 \mathbf{r}_i / dt^2$ is the acceleration and \mathbf{F}_i is the force acting on the i^{th} atom resulting from the interaction with other atoms around it. Thus, unlike Monte Carlo method, which basically depends on random sampling of solutions to get numerical results, molecular dynamics is a deterministic method in which the atomic phase space variables at the current time step are calculated by using previous time step.

Trajectory of atoms is calculated in a $6N$ -dimensional phase space consisting of $3N$ positions and $3N$ momenta. Because molecular dynamics is a statistical mechanics method, similar to Monte Carlo method, the MD is employed to attain some of the phase configuration that is distributed based on a statistical distribution function, or statistical ensemble. For example, microcanonical ensemble corresponds to a probability density function that fixes the total energy, E . In macrocanonical ensemble, from the infinite number of states, only states that have a certain energy (E) are selected. It is shown as by dirac function, $\delta(H(\Gamma) - E)$. In this representation H and Γ represents the Hamiltonian and phase space variables (positions and momenta), respectively. So, phase variables are selected so that the Hamiltonian is equal to the specific energy. Another example of statistical ensemble is the canonical ensemble in which the temperature parameter is constant and Boltzman function, $\exp(-H(\Gamma)/k_B T)$, is used as the probability density function.

In statistical physics, based on a selected statistical ensemble (e.g., canonical or microcanonical) for a specific quantity, there exists an infinite number of configurations distributed according to the corresponded ensemble. The physical quantities are identified as the averages over the configurations. Atomistic trajectories established by molecular dynamics simulations are considered as the set of configurations satisfying the ensemble conditions. In this regard, physical quantities can be measured by MD simulations easily by arithmetic averages of values taken at several instants.

Statistical physics maintains the connection between the microscopic properties and thermodynamic properties of a physical system. In theory, it is expected that for infinite simulation times, the phase space obtained by the MD simulation will be completely cover all configurations and the averaging operations will yield thermodynamic properties at that limit time. However, in practice, simulation times are always limited to a finite length, therefore it should be carefully examined whether sufficient sampling has been done or not. By this way, measurement of thermodynamic properties and evaluation of phase diagram of a certain material can be achieved by the MD simulations.

In addition to molecular dynamics simulations, there are other traditional atomistic simulation techniques such as quantum-mechanical methods in which Schrödinger

equation is numerically solved. Quantum mechanical methods are computationally very expensive; therefore, they are combined with other methods to get accelerated solutions. Beside to quantum mechanical simulations which are computationally very intensive, faster simulation techniques such as Monte Carlo and coarse grained models are also used to investigate atomistic structures.

2.2 History and Future of MD Simulations

Alder and Wainwright wrote the first academic paper in 1957 acknowledging molecular dynamics simulation [27]. By employing a hard sphere system through which interactions between the particles are defined as instantaneous collisions, they investigated the solid and liquid regions of the phase diagram of the system. The paper by Gibson et al. published in 1960 is one of the first studies that carry out molecular dynamics simulations of a 500-atoms system utilizing continuous force potentials with a finite difference time integration scheme to investigate the defect generation by the impact of radiation damage [28]. In another well-known study by Rahman in 1964, by using Lennard-Jones potential several properties of liquid Ar were explored with a system consisting of 864 atoms [29].

By using MD simulations, defect formation and their effects on the mechanical behavior in crystalline materials has been a popular subject for a long time [14]. In recent years, investigations on the defects have focused on linear and planar defects instead of point defects. As the potentials are getting improved to describe the interactions between atoms, more realistic systems are being simulated.

Dynamic behavior of biomolecules such as proteins, nucleic acids (DNA, RNA) and membranes, which are large macromolecules, can also be examined by molecular dynamics simulations [30]. Because functional properties of biomolecules are highly dependent on dynamical changes, the MD simulations are quite helpful to extract dynamical response of biomolecules. The MD simulations are also actively employed in pharmaceutical industry to effectively design of drugs.

In the last decade, by the development of Car-Parrinello method, which enables to calculate interatomic forces by solving the electronic structure instead of using an interatomic potential, electronic properties of materials can also be studied by the MD simulations.

The most prominent advantage that the MD simulations provide to researchers is the extraction of all properties about a thermodynamic system which is physically possible to exist. However, the power of the MD is limited to computational power and time-scale range that can be covered.

As the computational power increases day by day, more complex and so more computational intensive problems can be solved numerically. Because the computers are much cheaper than the laboratories, which provide the equivalent testing opportunities, molecular dynamics simulations can save significant amount of money in the development stages of new and novel materials and pharmaceuticals.



Figure 2.2 : Molecular device design examples (a) Gear chain [27] and (b) Planetary Gear [27].

Theoretically, molecular structure of a material, which may be organic or inorganic, can be designed in a numerical environment and its material properties can be determined via computer simulation methods such as the MD simulations. By using numerical specimens with different molecular structures, an optimum molecular structure that satisfies required material properties can be obtained. Following these numerical design iterations, proposed material can be synthesized in the laboratory and further refinements can be done in the laboratory environment.

The approach and procedure summarized above have already been applied in the design of new pharmaceuticals and are very close to being routinely employed in the processing of polymer materials. Day by day this approach is increasingly being realized in all material-related industries such as lubrication, catalysis, electronics and chemical engineering. From this point of view, molecular dynamics simulation method holds very important step to be taken towards novel materials or nano

electromechanical device design (see Figure 2.2). While its usage currently is limited to academic field excluding a few areas such as pharmaceutical and polymer design, in the next 20 years the MD simulation technique is estimated to take the place of today's computational tools , e.g., CFD or FEM in industry.

2.3 Limitations on MD

Although molecular dynamics method is a very useful and effective tool that helps researchers to dive into the atomistic world, there are some limitations that need to be addressed.

The first constraint on the MD technique comes from the usage of classical Newton's Laws instead of much more reliable Schrodinger's equation that can capture the quantum effects. It should be noted that the systems at the atomistic level are governed by quantum laws rather than classical macroscale laws. Classical approximation to the atomistic world can be verified by de Broglie thermal wavelength (Λ) [28] that was defined as

$$\Lambda = \sqrt{\frac{2\pi\hbar^2}{Mk_B T}} \quad (2.2)$$

where M , T , \hbar and k_B are atomic mass, temperature, Planck's constant and Boltzmann's constant, respectively. The classical approach used in the MD can be confirmed if Λ/a is much less than 1, where a is the mean nearest neighbor separation. For the liquids of light elements (e.g., Li and Ar) which are at the triple point that three phases (gas, liquid, solid) coexist at the same time, the ratio of Λ/a is at the order of 0.1. This ratio decreases down for heavier elements. Therefore, classical approximation is not confident for very light elements such as He and Ne. Besides this, as the temperature of any system is adequately low, quantum effects play much more important role which cannot be neglected. In these domains, molecular dynamics simulations should be used with caution.

Another issue with the MD simulations is the calculation of forces. It will not be wrong to state that the heart of an MD simulation is the calculation of forces. Because the interaction between atoms results in the forces acting upon corresponding atoms, which drive the motion of the atoms in the system, calculation

of forces on the atoms as accurate as is very important to capture the real physical response. Forces are generally calculated by the gradient of a potential function which is dependent on the coordinates of the atoms in the system. Therefore, the degree of realism of the MD simulation highly relies on the capacity of the potentials to capture the same response of the material under the boundary conditions that are employed in the simulation.

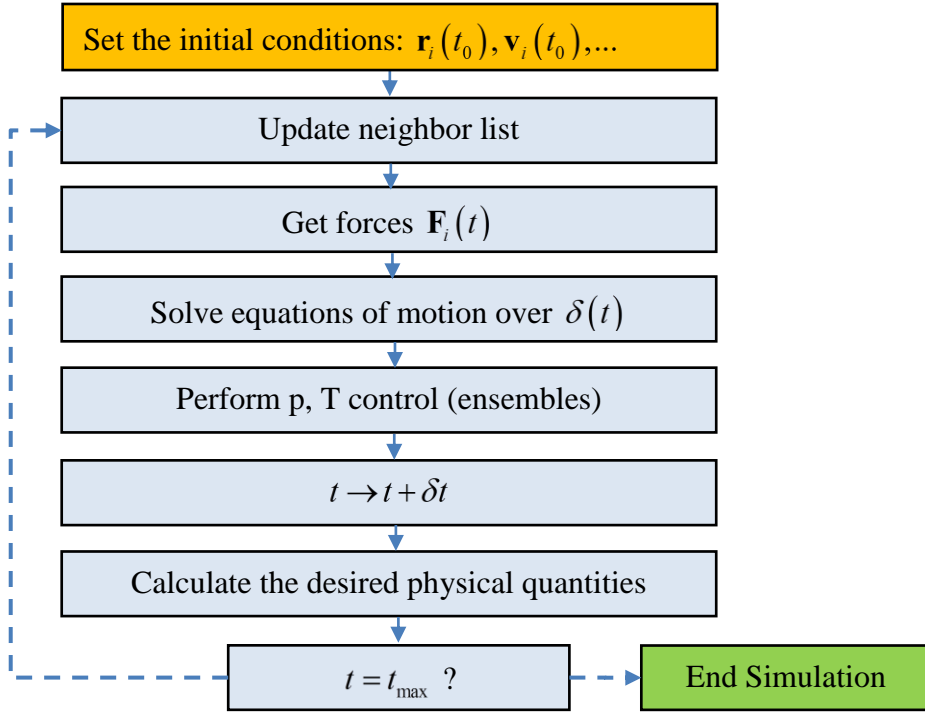


Figure 2.3 : MD simulations workflow.

Molecular dynamics simulations are combined with statistical mechanics to extract macro scale equilibrium (i.e., temperature, pressure and energy) and transport properties (i.e., diffusion coefficient, shear viscosity and thermal conductivity) of a classical many-body system. Figure 2.3 presents the major calculations that are performed in the MD calculations. According to this, three basic steps form the main framework of molecular dynamics. In the first step, initial positions and velocities for each atom in the system are assigned. Then, the particles in the simulation box commenced to interact with each other via a potential function and forces acting upon each atom are calculated based on the potential used. For this reason, the potential employed for the simulation is the key player to determine the degree of realism of the simulation. Due to computational efficiency, potential calculations are not performed between all atoms. Instead of that, by defining a radius of

neighborhood, for each atom, only a number of atoms within the neighborhood are used to determine interatomic forces.

In the second step, the Newton's 2nd law, $\mathbf{F}_i = m_i \mathbf{a}_i$, is utilized to obtain velocities and positions of atoms for the further time steps. Time evolution of atoms results in the motion of atoms in the simulation box yielding a trajectory in space. In the third step, position and momenta of atoms are used to determine physical quantities of the system by profiting from statistical mechanics concepts. As stated above, according to statistical mechanics, macro scale properties of a system is the average of the corresponding quantity over all possible quantum states, which is called the ensemble average. An ensemble can be considered as the fictive set of distinct quantum states, all of which have the same macroscopic properties such as temperature and pressure. In other words, for a defined system there exist different quantum states (i.e, phase space of atomic system) satisfying the same macroscopic properties. An ensemble is the collection of all quantum states that have same macroscopic property. According to the Ergodic hypothesis which declares that the ensemble averages of system properties are equal to time averages. Therefore, by taking the time average of measurements obtained by the MD simulations, macroscopic physical quantities can be achieved.

2.4 Time Evolution in MD Simulation

After assigning initial positions and velocities to particles, trajectory of the particles are determined by integrating the equations of motion numerically. The classical equations of motion can be written as

$$\dot{\mathbf{q}} = \mathbf{G}(\mathbf{p}, \mathbf{r}), \quad \dot{\mathbf{p}} = \mathbf{F}(\mathbf{p}, \mathbf{r}) \quad (2.3)$$

where H is the Hamiltonian, $G(p, q) = \partial H / \partial p$ and $F(p, q) = -\partial H / \partial q$. In classical dynamics, the Hamiltonian has the general form

$$H = \sum_i \frac{\mathbf{p}_i^2}{2m_i} + U(\mathbf{r}_i) \quad (2.4)$$

where \mathbf{r}_i and \mathbf{p}_i are the coordinates of the i^{th} atom and its momentum, respectively.

The first term of the Hamiltonian function, $\mathbf{p}_i^2 / 2m_i$ represents the kinetic energy

while the second term, $U(\mathbf{r}_i)$ is the potential energy resulting from the interatomic interactions.

Because of the reason that the Newton's 2nd law does not depend on time, the Hamiltonian function is also time independent. Furthermore, in the case of an isolated system, the total energy that is the sum of potential and kinetic energies of each atom is conserved.

The total time derivative of the Hamiltonian function given in Eqn. (2.4) is given as Eqn. (2.5) considering that Hamiltonian is not explicitly defined by time, $\partial H/\partial t = 0$.

$$\frac{dH}{dt} = \sum_i \frac{\partial H}{\partial \vec{p}_i} \dot{\vec{p}}_i + \sum_i \frac{\partial H}{\partial \vec{r}_i} \dot{\vec{r}}_i = 0 \quad (2.5)$$

The total time derivative of Eqn. (2.4) for an isolated system is given in Eqn. (2.6).

$$\frac{dH}{dt} = \frac{1}{m} \sum_i \vec{p}_i \cdot \dot{\vec{p}}_i + \sum_i \frac{\partial U}{\partial \vec{r}_i} \dot{\vec{r}}_i = 0 \quad (2.6)$$

When the Eqns. (2.5) and (2.6) are compared, following relations can be realized:

$$\begin{aligned} \frac{\partial H}{\partial \vec{p}_i} &= \frac{\vec{p}_i}{m} = \dot{\vec{r}}_i \\ \frac{\partial H}{\partial \vec{r}_i} &= \frac{\partial U}{\partial \vec{r}_i} \end{aligned} \quad (2.7)$$

Substitution of Eqns. (2.7) into Eqn. (2.5) results in the following relation:

$$\sum_i \left(\vec{p}_i + \frac{\partial H}{\partial \vec{r}_i} \right) \cdot \dot{\vec{r}}_i = 0 \rightarrow \frac{\partial H}{\partial \vec{r}_i} = -\vec{p}_i \quad (2.8)$$

Thus, Hamiltonian equations of motion which are first order differential equation with 6 degree of freedom can be written as follows:

$$\begin{aligned} \frac{\partial H}{\partial \vec{p}_i} &= \dot{\vec{r}}_i \\ \frac{\partial H}{\partial \vec{r}_i} &= -\vec{p}_i \end{aligned} \quad (2.9)$$

There exist many different algorithms for the time evolution of particle dynamics [29]. Here is given one of the basic algorithms to calculate the time history of coordinates and momenta. In this regard, firstly the force is calculated in time-half a

time step forward at the current positions. Then, the momenta in time half a time step forward is obtained. Following this, by using the momenta in time-half a time step forward coordinates in time by a full time step is calculated. After that, forces are recalculated by using the new positions and the momenta are advanced to full time step. The summarized algorithm can be shown as follows:

$$\begin{aligned} p(t + \Delta t / 2) &= p(t) + \frac{\Delta t}{2} F[p(t + \Delta t / 2), r(t)] \\ r(t + \Delta t) &= r(t) + \frac{\Delta t}{2} \{G[p(t + \Delta t / 2), r(t)] + G[p(t + \Delta t / 2), r(t + \Delta t)]\} \quad (2.10) \\ p(t + \Delta t) &= p(t + \Delta t / 2) - \frac{\Delta t}{2} \frac{\partial U}{\partial r}(t + \Delta t) \end{aligned}$$

By using Eqns. (2.10) again and again, trajectory of atoms including atomic coordinates and momenta can be extracted from the initial conditions and potential function defined for the simulated atoms.

2.5 Interatomic Potentials

Interatomic potentials which are used to describe the atomic interactions analytically can be regarded as the heart of molecular dynamics simulations [30]. The most general form of an interatomic potential is given as follows:

$$U(\mathbf{r}_1, \mathbf{r}_2, \dots, \mathbf{r}_N) = \sum_i W_1(\mathbf{r}_i) + \sum_{i,j>i} W_2(\mathbf{r}_i, \mathbf{r}_j) + \sum_{i,j>i,k>j} W_3(\mathbf{r}_i, \mathbf{r}_j, \mathbf{r}_k) + \dots \quad (2.11)$$

In Eqn. 2.11, W_1 defines a one-body potential which represents the external force fields such as gravitational field or external boundary conditions such as a wall function defined for particles in the simulation box.

The other term in Eqn. 2.11, W_2 describes a two-body potential which formulates the dependence of interatomic potential on the distances (r_{ij}) between pairs of atoms (\mathbf{r}_i and \mathbf{r}_j) in the atomistic system as shown in Figure 2.4(a).

On the right hand side of Eqn. (2.11), three-body potential (W_3) as shown in Figure 2.4(b) and higher order potentials add energy into the total potential energy of the system related to the geometry of atomic arrangement in the system.

Interatomic potential functions can be totally in an empirical form or based on numerical quantum mechanical approximations. Meanwhile, semi-empirical

interatomic potential functions are also derived by parametrization of experimental data and ab initio data. Force field calculations are the most time consuming part within the MD simulations taking up to approximately 95% of the total simulation time.

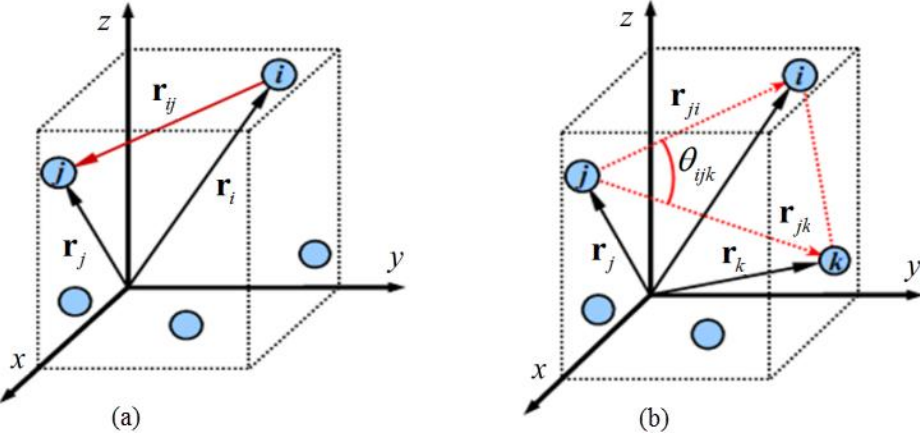


Figure 2.4 : (a) Two-body potential parameters, (b) 3-body potential parameters.

As mentioned before, setting up interactions between atoms or molecules correctly is very important in terms of adding realism into the MD simulations. At the bottom level, interactions are the product of quantum effects in which the electrons and nuclei of atoms come into play. The relationship of electrons and nuclei is not same by nature for different materials, which yields wide variety of behaviors. For instance, in some materials atomic bonding type is covalent while for some other materials it is ionic. However, in some other materials, the interaction type is metallic where the electrons are free to walk around the nuclei without being belong to a certain nucleus or shared by nuclei. As another extreme example in noble gases, electrons are tightly stitched to atoms representing a close-shell structure [31,32]. Apart from these extreme examples, these different quantum behaviors can be observed at different temperature and pressure conditions. For example, at room temperature silicon material is structured as diamond which is a covalent semiconductor, while at temperatures higher than melting temperature ($\approx 1670^{\circ}\text{K}$) silicon material turns into metallic [33]. Similarly, at constant temperature increasing pressure upon diamond material will cause a phase transition and results in a metallic material.

In general, two different approaches can be classified for the adoption of interactions between atoms and molecules. In the first approach, a potential function that depends on the interatomic positions (i.e., relative distances and angles) and some parameters

which are fitted to map the actual properties of the system onto the potential function [34]. In this approach, dynamics of electrons and behavior of electrons are not directly included in the potential functions. However, in the second approach which is theoretically more intellectual but computationally more expensive, electronic structure is taken into consideration and forces on the atoms are calculated based on quantum mechanical behavior. This second approach is the baseline of ab initio molecular dynamics simulations.

Classical molecular dynamics is based on the first approach; thus, the forces on the atoms are derived from the gradients of the potential function with respect to displacements:

$$\mathbf{F}_i = -\frac{\partial}{\partial \mathbf{r}_i} U(\mathbf{r}_i) = -\left(\frac{\partial U}{\partial x_i}, \frac{\partial U}{\partial y_i}, \frac{\partial U}{\partial z_i} \right) \quad (2.12)$$

As mentioned before, in MD simulation techniques it is very important to employ appropriate interatomic potential that will provide proper interaction forces between the atoms in the system. In this regard, force models are the most computationally intensive parts of a molecular dynamics simulation code, taking up to 95% of the total simulation time [36].

2.5.1 Pairwise interactions

As the simplest case, the interatomic potential can be represented as the sum of pairwise interactions:

$$U = \sum_{i=1}^N \sum_{j>1}^N u(r_{ij}) \quad (2.13)$$

where $\mathbf{r}_{ij} = \mathbf{r}_i - \mathbf{r}_j$, $r_{ij} \equiv |\mathbf{r}_{ij}|$ and the summation condition $j > 1$ avoids the summation of double interactions.

2.5.2 Lennard-Jones potential

Lennard-Jones potential whose formulation is given below is one of the most well-known potential utilized for Van der Waals system and initially offered to be used for Argon (see Figure 2.5).

$$u_{LJ}(r_{ij}) = 4\epsilon \left[\left(\frac{\sigma}{r_{ij}} \right)^{12} - \left(\frac{\sigma}{r_{ij}} \right)^6 \right] \quad (2.14)$$

Lennard-Jones potential is the function of two parameters such as ϵ is the scaling parameter that adjusts the magnitude of the energy (so can be called as energy-scale parameter) and σ is a length-scale parameter which affects the change of potential as the atomic distances change [37]. These parameters are selected to fit the certain physical properties of the system.

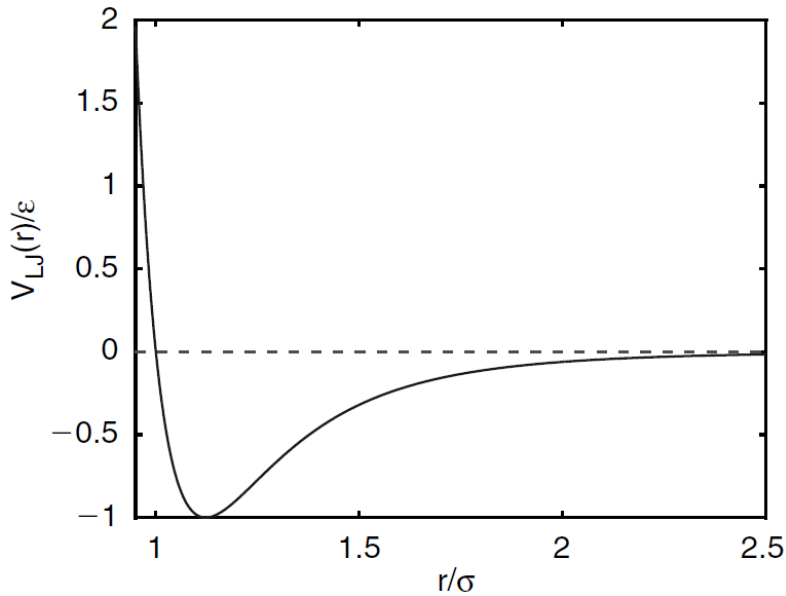


Figure 2.5 : Lennard-Jones potential [33].

Lennard-Jones potential is especially suitable for closed-shell materials such as Neon and Argon liquids where the electrons are confined to each atomic nucleus; therefore, for open-shell systems where strongly localized bonds are observed; it is not fully satisfactory [38].

2.5.3 Embedded atom method

Embedded atom method (EAM) is a semi-empirical model for the description of interatomic interactions and deals with each atom in the simulation box as being embedded in a host lattice environment which is comprised of all other atoms [39]. In this method, the total energy of a pure metal system consisting of N atoms is given by the following relation:

$$E_{tot} = \sum_i^N E_i \quad (2.15)$$

where E_i , energy term for the i th atom in the system is calculated by the following relation which consists of two terms.

$$E_i = \frac{1}{2} \sum_j \phi(r_{ij}) + F(\bar{\rho}_i) \quad (2.16)$$

where the first term $\phi(r_{ij})$ represents the atomic pairwise interaction between atoms is a function of atomic displacements and the second term $F(\bar{\rho}_i)$ that is also named as embedding energy function represents the effect of electron density of the environment in which the atom is embedded. The embedding energy function depends on local electron density $\bar{\rho}$ which is calculated as the summation of pairwise interaction terms $\rho(r_{ij})$:

$$\bar{\rho}_i = \sum_j \rho(r_{ij}) \quad (2.17)$$

Because of the reason that the actual forms of $\phi(r_{ij})$, $\rho(r_{ij})$ and F are not known exactly, their parameterized forms are used [37]. The coefficients of the parameterized functions are obtained by fitting to already known properties such as the lattice parameter, cohesive energy and elastic constants.

2.5.4 Adaptive intermolecular reactive empirical bond-order potential

Adaptive Intermolecular Reactive Empirical Bond-Order (AIREBO) Potential developed by Stuart et al. [40] potential is an empirical potential that is used to model interactions between Carbon and Hydrogen. This potential is an extended version of the Brenner's Reactive Empirical Bond-Order (REBO) potential [41] and non-bonding atomic interactions are included. The basic formula for the AIREBO potential is given by

$$E = E^{REBO} + E^{LJ} + E^{tors} \quad (2.18)$$

As it can be inferred from Eqn. (2.18), the AIREBO is compound of Reactive Empirical Bond Order (E^{REBO}), Lennard-Jones Potential (E^{LJ}) and torsional potential (E^{tors}).

The Reactive Empirical Bond Order E^{REBO} part of the AIREBO is a short range potential and represents the covalent bond interactions.

$$E^{REBO} = V_{ij}^R(r_{ij}) + b_{ij}V_{ij}^A(r_{ij}) \quad (2.19)$$

In Eqn. (2.19), V_{ij}^R and V_{ij}^A represent the repulsive and attractive pairwise potentials and b_{ij} is the bond-order term. Several chemical concerns such as the existence of neighboring atoms and type of hybridization which affect the condition of covalent bonding interaction are elucidated in this term.

Lennard-Jones potential term (i.e., E^{LJ}) employed in the AIREBO potential is expanded in Eqn. (2.20). It consists of conventional Lennard-Jones potential term V_{ij}^{LJ} as well as sine (S) and cosine (C) switch functions.

$$E_{ij}^{LJ} = S(t_r(r_{ij}))S(t_b(b_{ij}^*))C_{ij}V_{ij}^{LJ}(r_{ij}) + [1 - S(t_r(r_{ij}))]C_{ij}V_{ij}^{LJ}(r_{ij}) \quad (2.20)$$

$$\text{where } V_{ij}^{LJ}(r_{ij}) = 4\epsilon_{ij} \left[\left(\frac{\sigma_{ij}}{r_{ij}} \right)^{12} - \left(\frac{\sigma_{ij}}{r_{ij}} \right)^6 \right]$$

Torsional potential term E^{tors} given by Eqn. (2.21) depends on dihedral angle that is produced by four neighboring atoms and includes cosine switches varying from 0 to 1.

$$E^{tors} = \frac{1}{2} \sum_i \sum_{j \neq i} \sum_{k \neq i, j} \sum_{l \neq i, j, k} w_{ij}(r_{ij})w_{jk}(r_{jk})w_{kl}(r_{kl}) \times V^{tors}(\omega_{ijkl}) \quad (2.21)$$

$$V^{tors}(\omega) = \epsilon \left[\frac{256}{405} \cos^{10} \left(\frac{\omega}{2} \right) - \frac{1}{10} \right]$$

In this study, the EAM and AIREBO potentials have been used for the MD simulations of nanoporous metals and carbon nanotube networks, respectively.

2.6 Overview of LAMMPS

The LAMMPS (Large-scale Atomic/Molecular Massivle Parallel Simulator) developed by a cooperative research consortium consisting of two US Department of Energy (DOE) labs and three companies, is an open source classical molecular dynamics code specially tuned for multi-core computer clusters [26]. By using the LAMMPS, several nanoscale systems such as atomic, polymeric, biological, metallic, granular and coarse-grained systems can be modeled with a large library of force field potentials.

Systems with only a small number of particles to millions or even billions of particles can be modeled by the LAMMPS and the models can be run on any parallel machine on which C++ compiler works.

While the earlier versions of the LAMMPS was written in F77 and F90, latest versions of the LAMMPS have been written in C++. Because its programming design has been adapted to be updated by others, researchers can easily modify the code and extend its abilities by adding new force fields, atom types or boundary conditions.

The LAMMPS has a large interatomic potential library including potentials for soft materials (i.e., biomolecules, polymers), solid-state materials (e.g., metals, semiconductors) and coarse grained or mesoscopic systems. Other than atomistic systems, in a general manner as a particle simulator, the LAMMPS can also be employed to simulate any systems that consist of discrete particles, and interactions between particles are described by potentials.

In a common point of view, the LAMMPS realize the numerical integration of Newton's equations of motion for a set of atoms, molecules or macroscopic particles which are in interaction with each other by short or long range forces under several boundary conditions. In order to maintain a computationally efficient solution scheme, the LAMMPS employs neighbor lists to perform force field calculations and these neighbor lists are optimized for systems consisting of particles which are repulsive at short distances. In that way, elevation of local density of particles is avoided. In parallel runs, spatial-decomposition method is utilized to divide the simulation domain into smaller domains that are individually assigned to individual processors.

3. ATOMISTIC MODELLING AND MECHANICS OF NANOPOROUS MATERIALS

3.1 Introduction

Nanoporous materials are one of the classes of nanostructured materials, which already exist in nature both in bulk and membrane forms. Biological cell walls are good examples of nanoporous membranes, which have the ability to permeable selectively owing partially to their nanoporous morphology. As a bulk nanoporous material, zeolites have been used as catalysts in industry for many years. In the recent years, artificial nanoporous (np) materials are also manufactured with precise control on the morphological parameters including pore size, distribution, porosity and chemical properties [42]. Due to their extraordinary physical and chemical properties such as ultra high surface-to-volume ratio, exceptional electrocatalytic ability, strain reversibility and high yield strength, nanoporous materials are highly attractive candidates for medical application devices, i.e., bioartificial organs, implantable drug delivery systems, also for lighweighted structural applications, energy absorption devices and heat sinks [43].

In general, for nanostructured materials the target is to scale down the bulk materials into nanometer scale. However, for nanoporous materials the major interest is the scaling down the pore volume, i.e., empty space within the bulk material instead of bulk material that encapsulates the pore volume. Most of the important practical features of nanoporous materials arise from their structural network of pores, which enable them prominent candidates in applications such as adsorbing, accommodating, sieving and separating molecules. For this reason, nanoporous materials are different than other nanostructured materials due to that the functional properties of nanoporous materials are significantly affected by the characteristics of nanopores or nano cells such as pore size, shape and intensity in addition to the surface and bulk properties of constituent materials.

In most of their application fields, mechanical stability and integrity of nanoporous materials play an important role to sustain their functionality. Therefore, understanding of mechanical deformation mechanisms of nanoporous materials is essential to accommodate them safely within the planned service life in practical applications. Due to high expense of laboratory experiments for a series of tests to be conducted to get simple mechanical properties, computational studies are more favorable in terms of their flexibility to change parameters of numerical experiments and their simpler test setups comparing to laboratory experiments. However, in order to employ computational methods for the numerical experiments of nanostructural materials, there is a need in numerical specimens or in other words atomistic models those represent the morphological characteristics or nanostructural material.

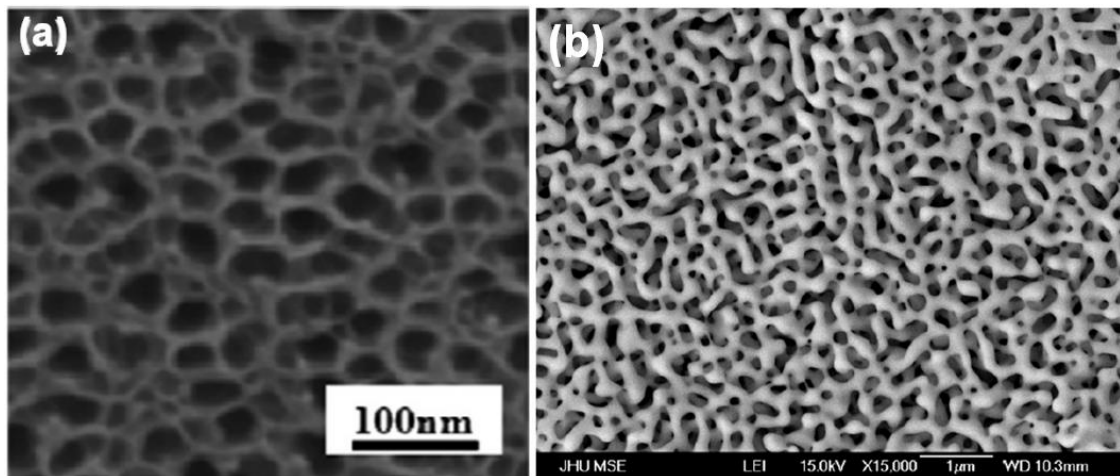


Figure 3.1 : Sample nanoporous material morphologies: (a) Nanoporous Gold [42] (b) Nanoporous Platin [43].

The most important concern for the numerical simulations of nanoporous materials is their complex morphology that consists of randomly intersecting ligaments with non-uniform cross sections. Figure 3.1 shows a few examples of complicated nanoporous structures. Their structure can be considered as a network of ligaments with varying cross sections intersected with each other forming junctions throughout the network. Due to this issues, in literature there are limited number of computational studies taking into account the complex stochastic characteristics of nanoporous materials.

The present chapter demonstrates the computational method developed for the generation of atomistic model of nanoporous structures and their utilization in molecular dynamics simulations to investigate the mechanical behavior of nanoporous materials. Following a detailed literature review of nanoporous

materials, the philosophy behind the atomistic modeling of nanoporous structures is presented by explaining the basic steps of the algorithm. It has been successfully shown that the morphology of nanoporous structures consisting of intersecting ligaments can be formed under spherical cell shape assumption by controlling the porosity. The main idea of the presented algorithm is the generation of ensembles consisting of randomly intersected spheres under certain constraints including maximum number intersections per one sphere and amount of intersection of two spheres. It is also illustrated that the generated foam models resemble conventional cellular structural units such as the ligaments with a non-uniform cross section distribution, junctions at which a number of ligaments are joined and pores on the cell walls with diameters controlled by certain parameters within the algorithm. After providing detailed explanations regarding the atomistic modeling process, results of molecular dynamics simulations performed on the atomistic nanoporous models with different porosity values are presented. According to those molecular dynamics simulations, it is found that softening of an open cell nanoporous structure subjected to tensile loading can be significantly reduced when the size of ligaments and the joints that connect them in the structure is designed to be sufficiently small. It is found by using molecular dynamics simulations that the softening becomes slightly slower with increasing the porosity for the structures with porosity less than or equal to 72%, and stress localization is observed during softening. In contrast, for structures with more than 75% porosity, the softening is much slower, and stress delocalization occurs during softening. It is argued that at relatively high porosity, the softening is governed by both the ligament size and joint size because their compliance becomes high enough to allow the overloading stress due to ligament rupture to be redistributed more effectively throughout the structure.

3.2 Literature Review

Nanoporous materials have been vigorously studied over the past decade. They have caught researchers' attention primarily for chemical characteristics such as catalysis, adsorption, filtration and sensing [42–48], but recently investigations have begun on their mechanical properties. The very low relative density of np materials makes them intriguing candidates for lighter materials in many different applications. However, the decrease in density is accompanied by a decrease in several important

material properties, including stiffness, strength [43] and ductility [44]. The decreases in stiffness and strength are expected because of scaling laws [45] and, in fact, the decreases are less than predicted due to the surface effects [45-47] and size effects [48]; so at present the need is greatest to understand and improve the loss of ductility in np materials. Several theories exist to explain macroscopic brittleness, including the possibility of a narrow ligament size distribution [49] resulting in failure of a large percentage of ligaments at once. In the same vein, a statistical average of ligament size overestimates the ability of the entire ligament network to carry the stress [50] since the weakest link of the minimum ligament size initiates the failure throughout the structure as the stress concentrations intensify. In this study, we present encouraging results of simulations to show that softening of nanoporous materials decreases at large porosities by the diffusion of stress among the entire structure, rather than concentration of stress at failure nucleation sites.

Since the popularity of np materials has increased in recent years, many experimental and theoretical studies have been devoted to investigate the properties of nanoporous materials. Many of these studies focused on np-Au material due to its unique properties and ease of manufacturing.

As an experimental study, Hodge et al. [45] performed nano-indentation tests to investigate the correlation between the yield strength, relative density and ligament sizes of open-cell nanoporous foams. Utilizing np-Au samples with different relative densities and ligament sizes, they constructed a Hall-Petch-type relation between the yield strength and ligament size by modifying the Gibson and Ashby's yield strength equation derived for open-cell macrocellular foams [42].

Recently published two papers [46, 47] focused on the mechanical properties of nanoporous gold (Au) materials by using atomistic MD simulations. In both studies, open-cell microstructure of nanoporous gold material is obtained by employing the phase field method which mimics spinodal decomposition of a binary fluid mixture of two constituents. Farkas et al. [47] investigated both tensile and compressive response of nanoporous numerical test samples and reported a significant tension/compression asymmetry in the yield strength, which was explained by the initial compressive state of the system emerging from surface stresses that favors the compression. Importantly, they also observe densification of the foam with the amount of ~15% under tensile deformation of 30%. This densification is interpreted

as the result of decrease in pore diameter that realizes by plastic deformation of ligaments.

Sun et al. [48], on the other hand, performed only uniaxial tensile simulations preferring to concentrate on the atomistic physical mechanisms behind tensile deformation of nanoporous gold. They reported the formation of stacking fault accumulations along the tension direction in the ligaments and at the ligament junctions together with the Lomer-Cottrell locks at the junctions. Modifying Gibson and Ashby's scaling law of the Young's modulus derived to link the bulk Young's modulus and foam Young's modulus, Sun et al. presented a relationship between the effective Young's modulus and relative mass density of nanoporous materials.

3.2.1 Theoretical and semi-empirical models for macroporous foams

Cellular solids, or commonly foams, can be defined as the assembly of three dimensional randomly distributed cells which are constructed by interconnected struts and/or plates. Struts enclosing the cells are beam-like structural members and intersect with the other struts to form the main frame of a cell. Intersections of struts form the vertices or junctions in the cellular solids. Cellular solids are classified as open cell and closed cell foams according to the material distribution along the edges of the cells. In the open cell foams, cells are interconnected with each other and plate-like faces closing the faces of the cell do not exist. In contrary to open cell foams, cells throughout the closed cell foams are not interconnected with each other due to plate/shell like walls between the cells. The material properties of cellular solids basically depend on the base material that establishes the foam structure, the relative density, mean cell diameter and the type of the foam (i.e., closed cell or open cell) [42]. In this dissertation, main focus is on the open cell cellular materials due to that most of nanoporous metals have interconnected open cell architectures. The book "Cellular Solids" by Gibson and Ashby [42] provides a solid background on the experimental and theoretical studies on macroporous (mp) solids.

In literature, there are numerous theoretical studies for the modeling of macroporous foams. Using repetitive idealized unit cell models to get homogenized behavior of foams is one of the techniques that have been employed in literature so far. These idealized unit cells used to set up cellular networks are selected to be in different shapes such as cubic [46], tetrakaidecahedral [49], tetrahedral [50] or bubbles [51].

In most of these micromechanical models, initial elastic constants (i.e., the Young's modulus E^* , shear modulus G^* and Poisson's ratio ν^*) have been aimed to be captured by the unit cell models considering the ligaments of the cells as structural beams and employing the descriptions of elastic constants in the classical strength of materials. One of these unit cell models to account for the mechanical properties is the widely employed cubic unit cell model developed by Gibson and Ashby [42]. In this cubic unit cell model, the scaling equations that maintain a relationship between the Young's modulus, yield strength and relative density of the foam are provided as follows:

$$\frac{E^*}{E_s} = C_1 \left(\frac{\rho^*}{\rho_s} \right)^2 \quad (3.1)$$

$$\frac{\sigma_{pl}^*}{\sigma_{ys}} = C_2 \left(\frac{\rho^*}{\rho_s} \right)^{3/2} \quad (3.2)$$

where ρ^* and ρ_s represent the density of the foam and density of the bulk solid material of which the foam is made, respectively. In the same manner, E^* and σ_{pl}^* are the Young's modulus and yield strength of the foam respectively, while E_s and σ_{ys} are the Young's modulus and yield strength of the solid material, respectively.

As it can be noticed from Eqns. (3.1) and (3.2), the key parameter that governs the mechanical properties of macro porous foams is the relative density of the foam (ρ^*/ρ_s). In this regard, as the relative density decreases the general trend is the cutback of the mechanical properties such as the stiffness, strength and ductility [52-53]. The coefficients C_1 and C_2 in Eqns. (3.1) and (3.2) are established to be equal to 1 and 0.3 [46], respectively, by adjusting the equations to the experimental data. It should be noted here that Eqns. (3.1) and (3.2) are valid for foams with low relative density values. The basic deformation mechanism at low relative density or equivalently at high porosities is the bending of cell walls [48, 52]. As the relative density increases, the modified material distribution around the cell walls results in different mechanical properties [48]. The yield strength equation, Eqn. (3.2), that is applicable for high porosities was modified by Gibson and Ashby to include

corrections for the description of mechanical behavior of foams at higher relative density values as follows:

$$\frac{\sigma_{pl}^*}{\sigma_{ys}} = C_2 \left(\frac{\rho^*}{\rho_s} \right)^{3/2} \left(1 + \left(\frac{\rho^*}{\rho_s} \right)^{1/2} \right) \quad (3.3)$$

In general, macroporous metallic foams demonstrate three distinguishable deformation stages under compressive loading. The first regime is controlled by the bending deformation mode of cell walls and forms a linear elastic region in parallel to conventional stress-strain curves. By its classical definition, the Young's modulus of the foam E^* can be calculated at this regime as the slope of the linear curve. The next stage following the linear elastic region is the long plateau region in which the cell wall bending deformation mechanisms ceased and collapsing of cells occurs. After this plateau regime, the final stage presents a sudden stress increase and densification of the foam. Densification is resulted from the collapsing of the cell faces upon each other and so is a sign of destruction of the cells to transform a solid material without any void. Therefore, the slope of the stress-strain curve at this regime is equal to the Young's modulus of the solid material of the foam; in other words, during compression loading of a cellular solid, the characteristic is dominated by the demolition of the cells foam structure transforms into the bulk solid material.

3.2.2 Experimental studies on nanoporous foams

Practical usage of cellular materials in some cases results in a requirement of mechanical stability of the material as in the cases of actuators and sensors. Therefore, investigations on the mechanical behavior of open cell nanoporous materials are vital to improve their role in the practical applications. In literature, there is an abundant number of experimental studies focusing on the yield strength and elastic modulus of nanoporous materials. The values reported in these studies for the yield strength and elastic modulus were shown to vary from 11MPa to 240MPa and 3GPa to 40Gpa, respectively [39, 53-56]. Within the comparisons between nanoporous gold (Au) and bulk Au, it is shown that nanoporous Au may be stronger than its bulk counterpart of which the yield strength depends on the load history and ranges between 10MPa to 200 MPa [56-61]. This superiority of nanoporous Au over

its bulk counterpart may enable a new class of material to show up itself in the high strength materials area.

Nanoporous (np) materials demonstrate a completely distinct behavior than their bulk counterpart materials. As an example to this important phenomena is that although bulk Au material show a ductile fracture failure under tensile loading, nanoporous form of Au presents a brittle behavior under tensile stresses. In addition to that, nanoporous materials exhibit typical properties of porous materials under both compressive and tensile loading. However, the scaling Eqns. (3.1) and (3.2) developed for the prediction of the Young's modulus and yield strength of macro porous materials are not applicable to nanoporous materials, which directed researchers to investigate new scaling equations to describe nanoporous materials.

As mentioned previously, Eqns. (3.1) and (3.2) that were developed by Gibson and Ashby were derived by directly comparison of experimentally measured Young's modulus or yield strength values at different relative density values. These equations can be used for all types of open cell macro porous foams disregarding the material types.

Indentation tests are one of the popular experimental methods to realize measurements for cellular solids. Generally, for bulk materials the hardness values (H) obtained from indentation test are related to the yield strength values as $H \sim 3\sigma$ relations [62]. On the other hand, this relationship between the hardness value and yield strength for cellular solids with the low relative density ($\rho^*/\rho_s > 0.3$) is assumed to be $H \sim \sigma$ relations [63]. Under a compressive loading, a cellular solid does not expand in the directions transverse to the loading direction; therefore, effective Poisson's ratio is assumed to be approximately zero. Indentation tests are also applied at nano scale by taking the name of nanoindentation and similar to macroscopic case the relationship between hardness value and yield strength is defined as $H \sim \sigma$ relations.

One of the first experimental studies on nanoporous materials performed by Rong Li and K. Sieradzki [53] was focused on the ductile to brittle transition in nanoporous Au. They showed that as the ligaments get thinner they do not behave in brittle manner. In another study, Khang et al. had reported that ratio of the specimen size to the element strength distribution at random porous structures plays a significant role

on the ductile-to-brittle transition [64]. In their study, Li and Sieradzki employed nanoporous Au that was specified as “highly porous” gold and concluded that their study would be a sample system for the determination of physical properties in the future works.

Following those studies mentioned above, by using different methods, mechanical properties of nanoporous materials have been studied. The majority of the studies performed on the nanoporous Au employed the nanoindentation techniques to determine the mechanical properties, i.e., the yield strength and Young’s modulus. In this regard, in the next sub-sections, the first review is given on the elastic modulus of nanoporous materials under compressive loading. After that, experimental studies which had utilized nanoindentation tests to study the yield strength properties is discussed. In the meantime, the results obtained through other techniques than nanoindentation is presented. Finally, the literature review was performed considering the studies that were focused on the tensile properties of nanoporous materials.

3.2.3 Studies on the Young’s modulus of nanoporous materials

Based on the results obtained from the studies on the elastic modulus of nanoporous materials, as the sample or microstructural geometry size decreases, an accompanying decrease in the Young’s modulus is not an anticipated behavior [52]. In this regard, Volkert et al. [65] carried out a series of uniaxial compression tests on nanoporous Au columns by using test specimens with different diameters to investigate the effect of sample size on the elastic modulus. They determined the Young’s modulus as 7 GPa by using the unloading portion of the true stress-strain curve of the samples under small plastic strain [66]. Beside this, elastic modulus of nanoporous Au was determined by Biener et al. [67] to be in the same order of magnitude by employing nanoindentation tests with depth sensing. The Young’s modulus of nanoporous Au obtained by several experimental techniques can be compared with the analytical predictions that could be provided by Eqns. (3.1) and (3.2). For this purpose, the Young’s modulus of single crystal Au which is in the range of 57-85 GPa [56] and porosity value of 36 % or relative density of 0.64 were used as input values into Eqns. (3.1) and (3.2). As a result, scaling equations yielded elastic modulus values of 7-11 GPa which match well with the experimental results

obtained from [67] and [68]. Moreover, in the outcome of experimental studies, no dependency of measured Young's modulus on the specimen sizes was noticed.

However, in contrast to the results obtained from the studies [66] and [56] that were mentioned above, in the study performed by Hodge et al. [45], they found out inconsistency between their experimental Young's modulus measurements, that were measured for foams with relative density in the ranges of 0.25 to 0.41, and analytical results calculated by the scaling equation in which the relative density exponent is equal to 2, i.e., $n=2$. On this issue, they provided an explanation saying that primary reason behind this inconsistency was that scaling equations developed by Gibson and Ashby were valid for foams with low relative density where the size of ligaments are less than the size of pores. On the other hands, the foams employed in their experiments with relative density ranges of 0.25-0.41, ligament and pore sizes are comparable to each other, which results in considerable contribution of ligaments into the overall deformation mechanism [68].

Another conflicting result was obtained by Mathur and Erlebacher [60] on the issue of size effects on the elasticity modulus. In their study, their results indicated that the Young's modulus of the nanoporous structure is influenced from the microstructural length scale changes. They reported that when they decreased the ligament size from 12nm to 3nm, four times less than the initial values, they observed four times increase in the Young's modulus of nanoporous Au. They used a buckling based method for the mechanical testing of stress free nanoporous Au films through which ligament sizes range from 3nm to 40nm. According to their results, size dependency of elastic modulus is much more apparent when the ligament sizes are smaller than 10nm. For the ligament sizes larger than 10nm, the effect of size dependency is not as considerable as the ligament sizes less than 10nm. Comparisons made between the Young's modulus values obtained from nanoindentation measurements [69-71] and values calculated by Gibson and Ashby scaling equation, Eqn. (3.1) resulted in good agreement for the ligament sizes larger than 12nm of nanoporous Au. Four times increase in elasticity modulus of nanoporous Au films in case of ligaments smaller than 10 nm was explained by several factors such as surface stress effect. Another explanation was related with the morphology of the nanoporous structure stating that porous networks consisting of smaller size ligaments contain large number of ligaments comparing with porous networks having larger ligaments, so less

ligaments. As a result of increasing number of ligaments, total bending stiffness of the porous network became larger than the network consisted of larger ligaments. However, these results are not incompatible with the other experimental findings which reported that the elasticity modulus of nanoporous materials is not affected considerably by size effects [72]. For instance, in the experimental study given in Ref. [73] it has been shown that elastic modulus of both Au nanowires, which represent the ligaments of nanoporous Au, and bulk Au material do not depend on the diameters of specimens.

So far all the studies given here are related with the dependency of elastic modulus of nanoporous materials on the size effects. In addition to these studies, there are also studies investigating the effects of residual contents within the nanoporous structure. For example, in one of these studies [74], effects of residual Ag content on the Young's modulus of nanoporous Au materials were investigated. They noted that during the de-alloying process of Au-Ag alloy, in order to generate ligaments smaller than 30nm, diameter surface diffusion should be suppressed which causes an increase in the concentrations of residual Ag content. As a result of increasing amount of residual content, density of the yielded material also increases, which in turn causes the Young's modulus to increase. This change in the Young's modulus due to the density increase can also be deduced from the Gibson and Ashby's scaling equation, Eqn. (3.1), which indicates that an increase of relative density will also provoke the raise of the Young's modulus of any kind of foam. In the guideline of the results obtained in this study, stiffening effect of ligaments smaller than 12nm that was observed in Mathur and Erlebacher's work [60] can also be explained by the existence of residual content in small sized ligaments.

3.2.4 Studies on the yield strength of nanoporous materials

Previously it was mentioned about that indentation had been proven to be an acceptable method to measure the yield strength of macro porous foams. However several concerns including the densification and indentation size effects should be handled to verify this measurement technique. For the densification issue, both nanoporous and macroporous foams face with a similar case in which the area of porous media contacting with indenter is compressed and densified locally while the other regions outside the indenter diameter range are not affected from the densification [75]. In the study presented by Andrews et al., several indentation tests

were conducted on macro porous aluminum (Al) foams to show the indentation size effects [76] and effect of sample size with respect to the cell size on the mechanical behavior was investigated. According to the results obtained by this study, a decrease in hardness values was observed in the form of an exponential function which has variables of cell size and indenter size. Similar results were reported by Hodge et al. [68] for nanoporous Au in the case of nanoporous materials. Andrews et al. [76] also reported that the yield strength values extracted from both compression and indentation tests for low density macro porous foams are comparable with each other. In the same manner, for the verification of nanoindentation tests, Chen et al. [77] provided validation of nanoindentation method by comparisons between nanoindentation test results with the results from bulge test measurements. They also presented another comparison between nanoindentation results and finite element solutions of mechanical response of thin nanoporous polymer films and showed that the values were in good agreement [77].

Experiments conducted via nanoindentation tests on nanoporous materials with low relative density pointed out the high strength capability of nanoporous foams. In one of those studies, namely Biener et al. [71], nanoporous Au specimens with 0.42 relative density and ligament length of 100nm were utilized in hardness measurements and hardness values obtained as a result of experiments were 10 times higher than the hardness values estimated by the scaling equation developed by Gibson and Ashby. They also demonstrated by the SEM (Scanning Electron Micrograph) images which are shown in Figure 3.1 that the type of governing deformation mechanism in a nanoindentation test realized on nanoporous Au is ductile or in other words plastic densification. Likewise, Volkert et al. [66] used ligaments of nanoporous ligaments with 15 nm length and established that the yield strength of those ligaments are close to the strength values of bulk gold material. For that purpose, they first determined the hardness value of 100 MPa through an experimental stage and then this hardness value is substituted into the scaling equation, Eqn. (3.2) with the relative density of 0.36. As a result, the yield strength of individual ligaments of nanoporous Au material predicted as 1.5 GPa which is in good agreement with the anticipated theoretical shear strength of Au which presents a state in which the neighbor atomic layers slide on another plane without the effect of dislocations [78].

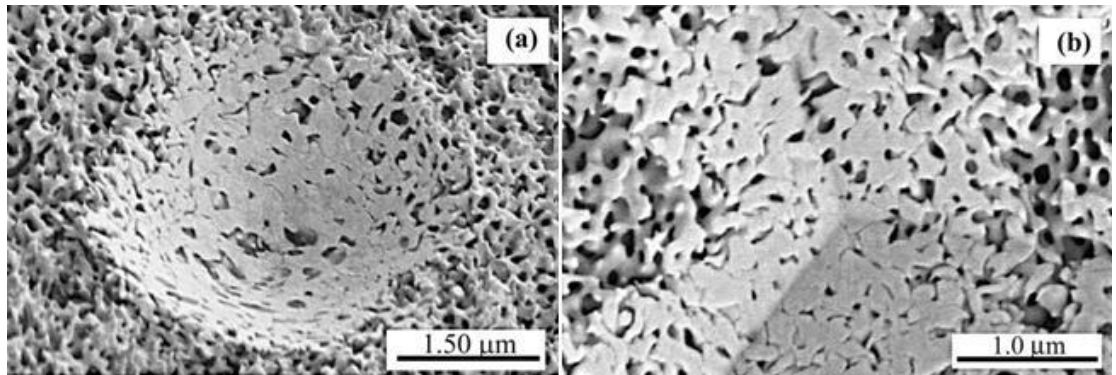


Figure 3.2 : SEM micrographs of 8000-mN indentations on a fractured surface of np gold: (a) conospherical tip with a tip radius of 0.1 mm, and (b) Berkovich tip with a curvature of 200 nm. Ductile densification is observed for both probes. Note that the plastic deformation is confined to the area under the indenter, and adjacent areas are virtually undisturbed [5].

High yield strength results obtained from the nanoindentation tests, which were mentioned above, was a surprising outcome of the experimental studies comparing with the results related with size effects which were expected to play much more important role in the mechanical behavior of nanoporous foams. In this regard, studies reported in the last years provided a thorough illustration of sample and grain size effects on the plastic deformation response of nanostructured materials. Dominant role of size effect on the mechanical characteristics of materials at nano length scale were demonstrated via both experimental studies and numerical simulations (e.g., molecular dynamics). For instance, Hodge et al. [68] investigated the dependency of the yield strength of nanoporous Au foams on the microstructural length scale by performing nanoindentation tests on the samples with relative density values ranging from 0.2 to 0.42. Figure 3.2 shows their comparison made between their experimental results with the values calculated via scaling equation given by Gibson and Ashby. It can be inferred from the figure, that as the ligament size decreases, the yield strength of np-Au having the same relative density also decreases. This result is in contradiction with the results provided by other studies on macro porous foams in which the ligament size is greater than $1.0\mu\text{m}$ and the predictions determined by the scaling equation of Gibson and Ashby which do not include the size effect dependency of mechanical properties for a fixed relative density. As the size of ligaments gets closer to $1.0\mu\text{m}$, the results obtained from nanoindentation experiments converge to the values calculated by the scaling equation.

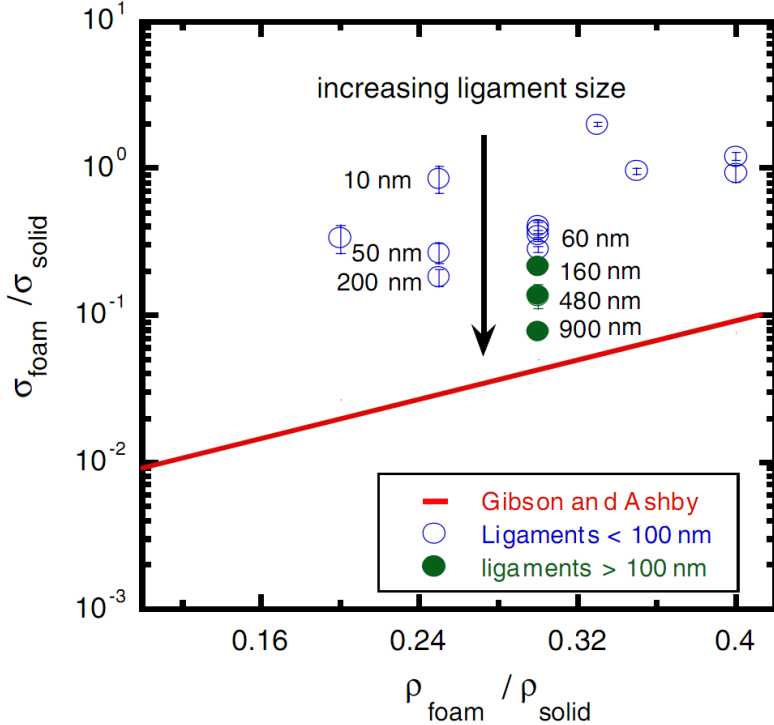


Figure 3.3 : Experimental values for foam yield stress for samples of np Au with relative density ranging from 20% to 42%, normalized by the yield stress of fully dense Au. The solid line presents the Gibson and Ashby prediction for a gold foam [79].

Effect of ligament sizes on the yield strength of nanoporous materials was also studied by Hakamada et al. [58] by carrying out nanoindentation tests of nanoporous Au specimens that were manufactured by dealloying method. By using the experimental results, they formed a relationship between the yield stress and ligament sizes as follows:

$$\sigma_{ys} = Kd^m \quad (3.4)$$

where d , K and m represent the ligament size, a constant and the power of size dependency, respectively. The value of m in Eqn. (3.4) is determined as -0.20 from the plot obtained by experimental results. This value obtained for m shows similarities with the values in analogous equations developed for the face centered cubic (fcc) metallic nanowires [79] in literature, which can be deduced that the deformation mechanisms in both cases are also comparable with each other. Upon this deduction, in their study, Hakamada et al. [58] mentioned that several microstructural alterations due to size effects observed in fcc metallic nanowires such as a decrease in the number of defects in grains, the repression of emission and

reabsorption of dislocations may also be resulting mutational mechanisms due to the length scale effects.

On the other hand, still there is not a certain agreement about the length scale dependent governing mechanisms that drive the deformation modes of nanoporous Au together with nanowires and columns of Au. Despite the lack of such a consensus on this issue, most of the studies in literature followed the path of comparing the results belong to the mechanical behavior of ligaments in np-Au with the results of columns and nanowires of Au. In the studies [80] and [81], experimental results provided by indentation tests on nanoporous Au and nanomechanical measurements conducted on submicron Au columns and nanowires were evaluated. Dependency of the yield strength to the length scale as discovered in nanoporous Au was also observed for the micropillars or nanowires of Au. As a matter of fact, the yield strength values of microcolumns and nanowires which have very small crystal structures yielded very high values. Moreover, in another study reported by Geer and Nix [82] the length scale dependency of the yield strength established in np-Au was proved to exist also for submicron Au columns and concluded that theoretical yield strength could be maintained as the diameters of Au columns were reduced below a few hundred nanometers.

In the study performed by Volkert and Lilleodden [67] micropillars of Au which were made from large grained Au sheets using a focused Ga^+ beam were subjected to nanoindentation tests to measure the yield strength. Based on the experimental results, an exponential law, d^{-n} describing the relation between the yield strength and the diameter of columns, d employed in the experiments similar to Eqn. (3.4) was derived. The exponential term of this relation, n was found to be 0.61. Because these results are in good agreement with the relationship between the yield strength and ligament diameter which was also observed by Eqn. (3.4) for np-Au, it can be concluded that the deformation mechanisms of nanoporous Au and micropillars of Au may have similarities.

Explanation of the length scale effect on the mechanical properties of nanostructured material is attributed to the existence of free surfaces which confines the number of dislocation nucleations. Biener et al. [72] in their study noted that because the ligaments of nanoporous-Au are related to the Au microcolumns, as the size of the ligaments decreases within nanoporous-Au, the stress values at which the

dislocations are activated to move increase as well until the theoretical shear strength is reached. In this regard, their results indicating the dependency of nanoporous Au to the length scale effects are in the same scope with the results obtained from compression tests performed on micro columns of Au. Several factors such as modified internal stress fields, changes on the active dislocation size and number of dislocation sources are shown as the reasons of increasing of dislocation activation stress [83]. Many of the studies which demonstrated that the yield strength of ligaments in np-Au approaches the theoretical shear strength are also satisfied with this explanation provided for micro columns of Au; therefore, Biener et al. [67] referred nanoporous Au as the three-dimensional network of defect free ultra high strength Au nanowires.

All the studies given so far mentioned about similarities between deformation mechanisms of nanoporous Au and Au nanowires or microcolumns. However, in the study presented by Dou and Derby [70] showed that the deformation mechanisms of these two nanostructure groups may differ from each other. In this regard, in order to focus on micro-mechanisms of deformation in nanoporous Au ligaments, they investigated the deformed structure following an indentation by using the TEM. According to their results, they reported that there was no considerable distinction between the results obtained by the use of np-Au ligaments and 3D macroscopic samples due to that the deformation mechanisms of both np-Au ligaments and bulk np-Au consisted of comparable ligament sizes are similar. According to the studies performed by Gibson and Ashby, it had been suggested that due to localized plastic deformation at the intersection of ligaments, namely junctions, plastic collapsing of macro porous foams occurred by bending of ligament. With this conclusion reported by Gibson and Ashby, localized plastic deformation through ligament bending also observed by surface steps noticed in the TEM images presented in the study of Dou et al. [84]. Moreover, around the junctions where the ligaments are met, Shockley partial dislocations and micro twins were observed to exist. However, in the deformed structure of np-Au ligaments, no perfect dislocations were found, which is compatible with strengthening models based on strain gradient hardening [84]. Strain gradient hardening models are basically continuum scale deformation mechanisms-based models claiming that geometrically essential strains block further deformation yielding a strengthening effect on the mechanical behavior of the material. The TEM

images provided by Dou et al. [84] demonstrated the generation of complex microtwins by propagation and interaction of Shockley partial dislocations. They also claim that the basic difference between the compressive deformation mechanisms of nanowires and np-Au ligaments is the primary bending mode observed in nanoporous structures.

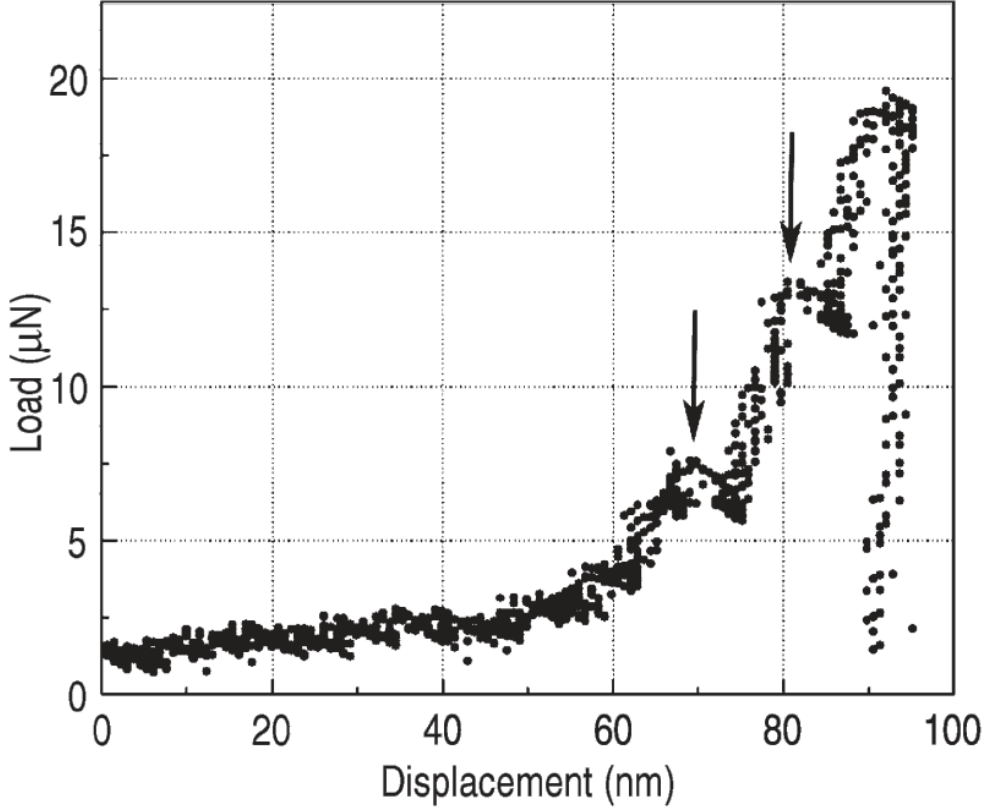


Figure 3.4 : The load-displacement curve recorded during in-situ TEM nanoindentation of a 150 nm np-Au film. It appears that the load drops (marked by arrows) corresponding to collective collapse of a layer of pores [67].

One of the experimental techniques that is exhibited in the last years and named as in-situ nanoindentation method was utilized by Sun et al. [46] to study on the deformation mechanisms of nanoporous Au thin films. In their study, they used np-Au thin films 150 nm in thickness consisting of ligaments with diameters in the range of 10 to 20 nm [46]. As noted, they investigated the microstructural characteristics of deformation by employing the TEM during the operation of nanoindentation. By this way, they had visualized the deformation process, and so by using the TEM images they stated that in the initial phase of nanoindentation, deformation of np-Au was noticed to occur readily by compressing of the ligaments just under the indenter while the rest of the structure below this region stayed

uncompressed. In the further time of the nanoindentation process, as the indenter moves forward, head of the compressed region moved in front of the indenter resulting in collapsing of neighboring ligaments.

Two local maximum points which are separated approximately by a distance of size of a pore on the displacement versus load curve as shown in Figure 3.3 indicate the compression and then collapsing of a layer of cells in which the ligaments enclosing the cells buckle, at the same time yielding a sudden decrease in the load value applied by the indenter. In addition to that, by the help of the TEM images tracing of dislocations showed that dislocations spanned the ligament width. It was also noticed that the transportation of dislocations throughout the ligaments and at junction regions where the ligaments are intersected, dislocations are entangled with other dislocations coming from other ligaments.

Although there are huge amounts of studies focusing on the size effects and high yield strength characteristics of nanoporous materials, there are limited numbers of studies which presented the strain hardening properties of nanoporous materials. The main reason for this is the difficulty of evaluating the complicated strain history generated by nanoindentation technique. In the most of the experimental research, nanoindentation method is employed due to its simplicity compared with other mechanical testing methods. However, as a result of nanoindentation test, complex strain history avoids interpretation of strain hardening characteristics of the material. Figure 3.4 shows the true stress-strain curve of np Au ligaments obtained through uniaxial compression tests, which were demonstrated by Volkert et al. [67]. As it can be inferred from Figure 3.4, there is a substantial strain hardening behavior of nanoporous Au columns, which approaches approximately two times of the yield strength progressing up to 30% strain. It is also noticed that each strain hardening region is followed by a plastic flow region.

By using thin nanowires of np-Au through nanoindentation tests, strain hardening characteristics of np-Au were also studied in Ref. [85]. In this study, strain hardening property observed even at small strain values was attributed to the contacts between the ligaments of high relative density foams.

Nano pillar micro-compression testing technique is another experimental method that is less complicated than nanoindentation test for the measurement of nanoporous-Au.

In their study Biener et al. [61] performed uniaxial compression tests of np-Au columns by using the procedure provided by Uchic et al. [86]. Micro columns of Au specimens employed in that study were manufactured by focused ion beam technique with approximate length-to-diameter ratio of two. Strain hardening behavior of the micro columns was not captured from the true stress-strain curve in which a constant flow stress was observed following approximately 2.5% strain (see Figure 3.5). On the other hand, as also obtained in nanoindentation measurements, in the compression tests carried out in this study yielded high yield strength values, which in turn indicates that the type of the testing method is not the reason behind the results of high yield strength values of np-Au.

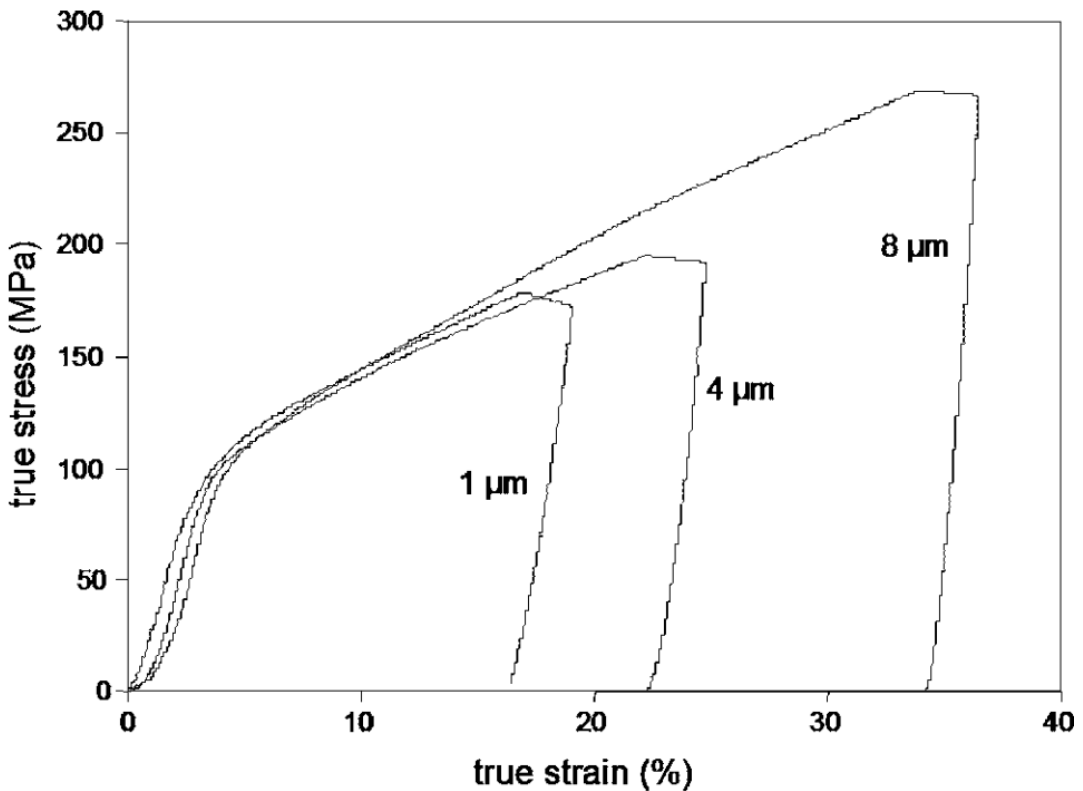


Figure 3.5 : True stress-strain curves from 1, 4 and 8 μm diameter nanoporous Au columns [66].

Even though there are many studies having reported the remarkably high yield strength of nanoporous Au that were presented in the previous paragraphs, there are also some other studies which demonstrated considerably different values of yield strengths. For example in Ref. [87], the obtained value of yield strength for np-Au is approximately one order less than the values reported in the studies where nanoindentation experiments were performed on the samples. In that study, np-Au samples were generated by a different method that was introduced by Jin et al. [88].

In general, dealloying manufacturing method yields np-Au samples which show unexpected mechanical failures due to their volumetric shrinkage tendency such as stress corrosion cracking and brittle fracture [89]. Crack formation during manufacturing of nanoporous Au was able to be avoided and thus crack free samples were able to be manufactured by Jin et al. [88]. Because the volumetric shrinkage percent during the manufacturing process is less than 2%, their samples were crack free. Their compression test results showed that their samples exhibit outstanding ductile behavior in the way that without any fracture almost all of the structure was able to be compressed. Plastic deformation distribution across the sample section was shown to be homogenous by electron backscatter diffraction (EBSD) maps, which conflicts with conventional observation of deformation bands propagating through the sample. The other discrepancy of this study is the low yield strength values that are not consistent with other studies which had employed nanoindentation tests for the yield strength measurements and equated the yield strength value to hardness value ($H \sim \sigma$) for only low density foams [89].

The other reason underlying the noticeable distinct results may be due to the manufacturing method which causes different morphology formation. Their micro structure formed by a long-range coherent crystal lattice system where each grain consists of billions of nano ligaments that have the same set of crystallographic slip planes [90]. From their EBSD maps, it was observed that during the deformation process the grain structure of the ligaments did not change which was evaluated as that a collective shear of ligaments occurred along shared slip planes and in the same directions contrary to the known low density foams [91]. The other studies is worth being mentioned in this section considered that macroscopic strength of nanoporous materials could be driven by the joint relation of relative density and size dependency of ligaments; however, in this study another aspect of deformation mechanism which is the interrelated deformation of individual ligaments, was presented to be accounted for the understanding of deformation mechanism of np materials.

3.2.5 Studies on the Tensile Behavior of Nanoporous Materials

Number of studies on the tensile fracture behavior of nanoporous materials is not too many in comparison with the number of studies on the compressive deformation behavior. Brittle tensile characteristics of Au-Ag alloys under corrosive conditions

had been demonstrated in the earlier studies [92] focusing on the stress corrosion crack formation on Au-Ag alloys. The results presented in these studies were consistent with the film-induced cleavage model according to which crack generation is encouraged by the formation of thin layer of np-Au during the dealloying process and propagation of the crack is through the new formed dealloyed layer towards not corroded bulk material [93]. As mentioned before, although bulk Au material exhibits ductile fracture characteristics in tensile loading, it has been demonstrated that macroscopic tensile failure mode of np-Au materials is remarkably brittle [94]. Due to this brittleness of np-Au materials, handling of np-Au test specimens were reported to be so difficult. In addition to those, Li and Sieradzki [63] presented that considerably larger test specimens comparing with their ligament/pore size yield more brittle fracture behavior. Because of these properties of nanoporous materials, their tensile mechanical testings are very challenging to perform.

Dealloying process of nanoporous metals causes high ratios of volume shrinkage as well as tensile built stresses embedded into the structure [95]. As the content of Ag in the Ag-Au alloy that is employed in the dealloying process increases, the degree of brittleness of the structure also increases. For instance, samples generated from $\text{Ag}_{80}\text{Au}_{20}$ alloys by dealloying are quickly fail to keep their structure without destruction due to inherent tensile stresses from dealloying process, while the samples generated from $\text{Ag}_{70}\text{Au}_{30}$ alloys survive their integrity. The study [96] performed on the nanoporous Au nanowires that were made from $\text{Ag}_{82}\text{Au}_{18}$ (i.e., with high content of Ag) established a significant result which stated that nanowires as well as nano thin films are more resistant to tensile built stresses that emerge due to dealloying process than their macroscale counterparts, because of the reason that their volumetric shrinkage is not very effective.

Biener et al. [71] in their detailed study conducted three-point bending tests to investigate the fracture characteristics of np-Au. It was observed that test specimens were catastrophically failed in the tensile stress region rather than compressive zone following a crack propagation phase, showing that the structure is more susceptible to compressive loadings. Because there was no traceable plastic flow before the failure, it was concluded that the failure of the material occurred after a crack propagation phase which is in brittle nature. On the other hand, ductile failure of individual ligaments through nanoporous Au was presented by the SEM images of

the microstructure showing the necking behavior due to plastic deformation. Besides these, MD studies on Au nanowires [71] demonstrated that elongation of ligaments is 100%, which was an expected result due to that gold is the most malleable metal.

As also reported by an earlier study by Khang et al. [64] for a random network model, macroscopic brittleness is considered to be the result of narrow ligament-strength distribution through the network. Based on their explanation to the brittle behavior, failure of the weakest ligament initiates the crack propagation in the network of ligaments by causing extra straining and overloading of closest ligaments. The route of the crack propagation is the direction in which the resistivity of the structure is the lowest. Therefore, Khang et al. [65] defined the total strength of the network as the largest critical defect resulting in the highest stress concentration. As stated in Ref. [72], amount of Ag component increase in the grain boundaries of Ag-Au alloy that would be used in the dealloying process activates the generation of higher porosity material while creating 2D like voids. These voids are the root cause of the crack formation and then propagation due to elevated stress concentrations. In this content, they noted that the mechanical behavior of np-Au could be enhanced by introducing wider ligament strength distribution.

In another study [97], test specimens were tested within a customized testing setting and comparable fracture behavior of np-Au could be obtained through a serial experimental work. In this study, digital image correlation (DIC) method was utilized to perform strain measurements, which makes it possible strain measurements without any contact with the capacity of full-field advantage. In addition to those, this method of which the details are provided in [98] also enables the calculation of the Poisson's ratio. Due to macroscopic brittle behavior of nanoporous Au deformation, test specimens did not show any plastic flow in tensile loading. Following the initial elastic phase in the tensile deformation, a crack initiation and then propagation phase is ceased by a quick failure which occurs on the plane perpendicular to the tensile loading axis indicating the brittle fracture behavior. As it can be noticed from the SEM images they provided, they also stated the plasticity of the individual ligaments causing the ductile failure of the samples. The plastic deformation of the ligaments was reported to be considerably localized due to that neighbor ligaments stayed intact while 1 or 2 ligaments that are in the crack surface region are subjected to plastic deformation. This phenomenon was explained in their

study by the situation that ligaments cannot store the dislocations which move to the surface and then escape.

3.3 Atomistic Modeling of Nanoporous Materials

In this section, complexity of nanoporous structures are introduced and then the algorithm developed to generate nanoporous atomistic models is presented along with several examples of atomistic models generated by the proposed method.

3.3.1 Random network nature of nanoporous materials

As mentioned previously, the most challenging part of investigating nanoporous materials via numerical simulations is the generation of atomistic models which represent the basic morphological properties in consistent with real geometrical features of nanoporous structures. For this reason, the number of studies regarding computational evaluation of behavior of nanoporous materials is limited to small numbers.

Major complexity of nanoporous systems, or more generally porous systems, emerges from their random nature topology that can be considered as a network consisting of intersected ligaments. Lengths of ligaments throughout the network distribute inhomogeneously while their cross-sectional shapes and areas change unpredictably along their length. Ligaments and their junctions encapsulates void volumes which are called cells within the network. However, current preprocessor capabilities of atomistic simulation codes only allow to model atoms in basic geometrical design shapes.

As shown in Figure 3.1, especially nanoporous metals that are manufactured by dealloying process depicts remarkable topological complexities such as randomness, bicontinuous features with very high degree of negative, positive and saddlepoint curvatures [99].

Because of complex morphologies of nanoporous materials, it is difficult to obtain their representative numerical models, which in turn avoids increment in the number of computational studies. The complexity of structures of nanoporous materials comes from their inherent cellular structures that consist of irregularly interconnected ligaments along which the mass is distributed non-uniformly. For the purpose of modeling nanoporous materials as close as to the real morphology, random nature of

porous network should be reflected in the numerical model by adding randomness into the several geometric variables such as cell locations and cross sectional area of ligaments.

3.3.2 Algorithm for generation of nanoporous models

Atomistic modeling of the nanoporous structures in this study is based on an earlier work used to model microcellular carbon foams [62] as shown in Figure 3.6 where the cell sizes within the foam structure are in the micron scale. However, in case of nanoporous materials, the range of cell size decreases below 100nm. The principle assumption made for the developed method is the spherical cell shape assumption, which results in spherical void volumes within the porous network.

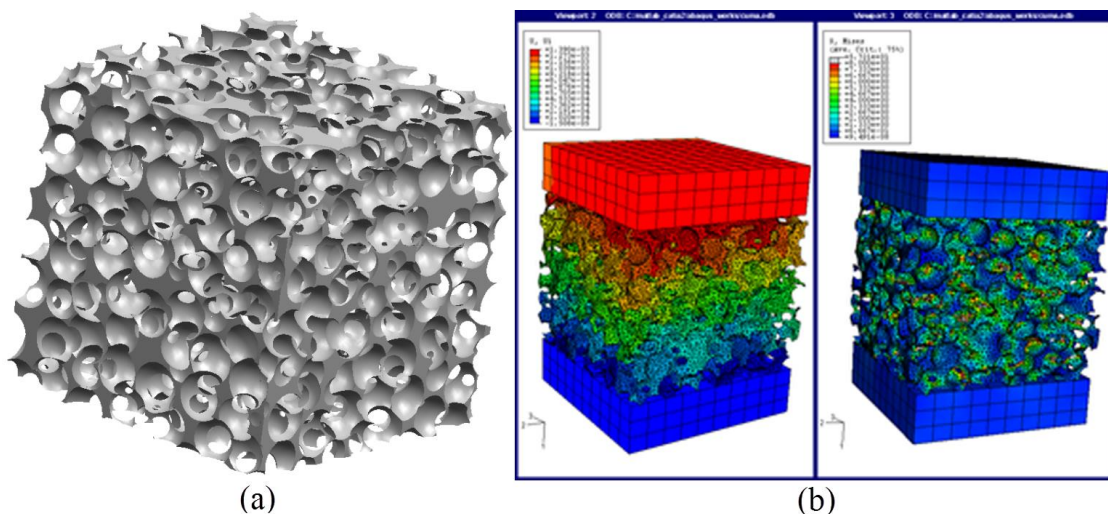


Figure 3.6 : Foam models employed for the mechanical response of carbon foams
 (a) Computer Aided Drawing (CAD) model, (b) FEA results of foam models [62].

The basic idea of the generation method is to create an ensemble of spheres, which consists of spheres intersected with a number of other spheres. Before going further into the explanation of the technique utilized to obtain nanoporous atomic structure, main definitions that are used in the algorithm scheme will be given. One of these is the ‘target sphere’, which is the identity of the sphere on which a specific number of other spheres are placed intersecting with it. These spheres that are placed onto the target spheres are named as ‘neighbor spheres’. See Figure 3.7 (a) for the illustration of the target and neighbor sphere concepts.

The algorithm explained in this section is coded by using Matlab programming language. The Matlab code generates several outputs that are utilized to create

atomistic nanoporous models. One of these outputs is the central coordinates and radii of spheres that form an ensemble consisting of interconnected spherical network. The other important output from the code is the identities of the neighbor spheres for each target sphere, which provides the statistical characterization of the spherical network in terms of number of neighbors per target. The code also generates the LAMMPS script file which utilizes the central coordinates and radii of spheres in the generation of atomistic porous structure.

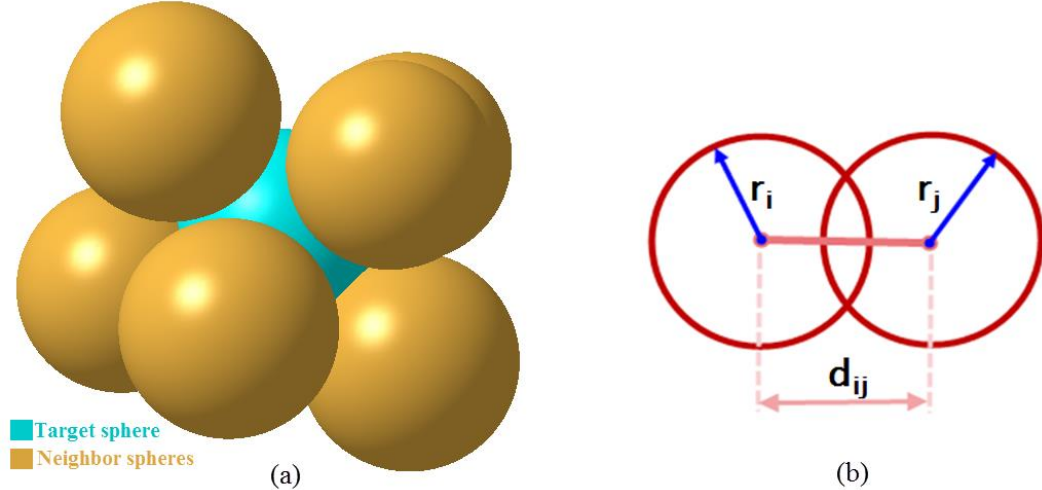


Figure 3.7 : (a) Representation of a target sphere and its neighbor spheres and (b) Parameters used for overlapping and non-overlapping ratio calculations.

The other two concepts defined within the algorithm is the overlapping and non-overlapping ratios, which are used to manage amount of intersection and minimum distance between neighbor spheres of the same target sphere, respectively. ‘Overlapping ratio’ denoted by c_o is defined as the ratio of the distance between the center of the two intersected spheres and the sum of their radii. ‘Non-overlapping ratio’ denoted by c_{no} is defined as the ratio of the distance between the center of the two non-intersected neighbor spheres and the sum of their radii. While the overlapping ratio parameter is employed for intersected spheres, non-overlapping ratio is used for non-intersected neighbor spheres located around the same target sphere. Figure 3.7(b) presents the parameters that are used to calculate overlapping and non-overlapping ratios by Eqn 3.5.

$$c_o = \frac{r_i + r_j}{d_{ij}} \quad (3.5)$$

$$c_{no} = \frac{d_{ij}}{r_i + r_j}$$

In Eqn. 3.5, r_i and r_j are the radii of spheres which are considered for the overlapping and non-overlapping ratio calculations, and d_{ij} is the distance between central coordinates of corresponding spheres.

The algorithm used to generate ensemble of randomly intersected spheres starts with the creation of a sphere randomly located in the design space and issued as the target sphere to generate neighbor spheres intersected to the target sphere. After completing the maximum number of neighbor spheres on the target sphere, a new target sphere is selected amongst the neighbor spheres and creation of the neighbor spheres progresses to be located on the new target. As the new spheres intersected with existing spheres are created, ensemble of spheres grows to larger sizes. When the required size of the ensemble, which depends on the size of the specimen that will be tested numerically, is reached, creation of spheres is ended.

The central coordinates of neighbor spheres (x, y, z) are calculated by using the central coordinates of the target spheres (x_0, y_0, z_0) in the spherical coordinate system as shown in Eqn. 3.6.

$$\begin{aligned} x &= x_0 + r \sin \theta \cos \phi \\ y &= y_0 + r \sin \theta \sin \phi \\ z &= z_0 + r \cos \theta \end{aligned} \tag{3.6}$$

In Eqn. 3.6, ϕ and θ are angular components of the spherical coordinates and are selected randomly from specific ranges. In this regard, ϕ is randomly chosen from 0 to $\pi/2$ and θ is randomly chosen from 0 to π . The other parameter r represents the distance between the target sphere and corresponding neighbor sphere. It is determined by the overlapping ratio defined as a preliminary for the numerical model. If the neighbor sphere, which is selected randomly by these stochastic spherical coordinates, does not satisfy the constraints which are defined by overlapping and non-overlapping ratios, a new random neighbor sphere is generated until all the constraints are satisfied.

As mentioned above, central coordinates of neighbor spheres are generated in a stochastic manner. However, for the purpose of controlling certain properties of the nanoporous structure such as porosity and ligament size distribution, several design parameters are maintained to be adjustable in the random sphere generation

algorithm: One of these design parameters is the range of diameter values of spheres that are generated. So, by this way the radii of spheres can be selected randomly from a pre-defined array in the process of sphere generation. By controlling the size of spheres, cell sizes in the porous structure can be kept under control.

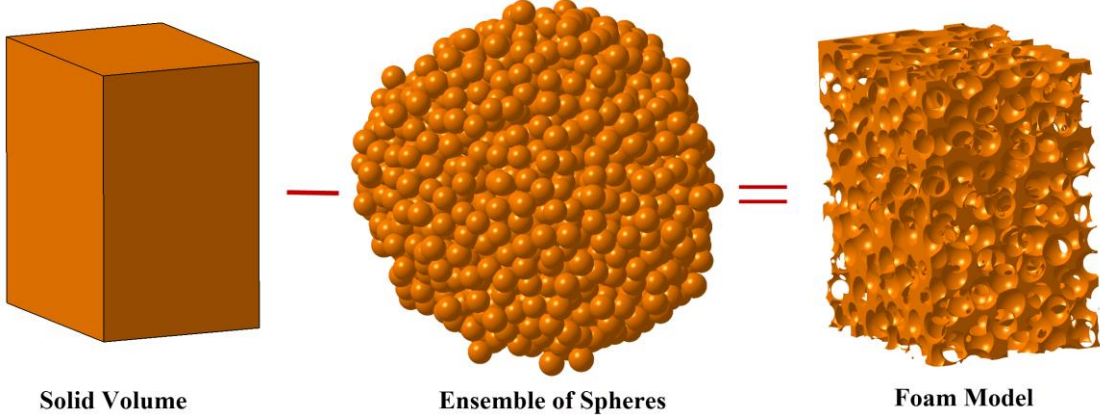


Figure 3.8 : Generation of a CAD foam model by spherical ensemble approach.

The other parameter that is controlled within the generation process is the maximum number of neighbor spheres intersected with a target sphere. This parameter affects the porosity as well as the degree of interconnectivity of the porous structure. Beside these parameters, overlapping and non-overlapping parameters which have been defined previously are varied to generate porous structures with different porosities. In the mean time, some of these are interrelated with each other. For example, as the overlapping ratio is increased, the number of neighbor spheres per target sphere should be decreased accordingly due to the reason that the surface area reserved on the target sphere for one intersection increases. Similarly, as the non-overlapping ratio is decreased the number of neighbor spheres per one target can be increased. Because, non-overlapping ratio is a measure of minimum distance between the neighbor spheres located on the same target; thus, decreasing this distance enables to place more spheres on the target. For these reasons, while setting these initial parameters, the inter-relationships between these parameters should also be considered.

Non-overlapping ratio values are kept above 1 to avoid any possible intersections between neighbor spheres around the same target sphere. The volume between non-intersected spheres defines the ligaments and junctions (see Figure 3.9). Therefore, varying the overlapping ratio enables to alter ligament and junction sizes.

As shown in Figure 3.8, the foam structure with spherical cell shape is obtained by removing the unified volume of spherical ensemble from the bulk volume of material with desired shape. In Figure 3.8, the final foam model is obtained in the same volumetric shape of the solid volume from which the ensemble of spheres are subtracted.

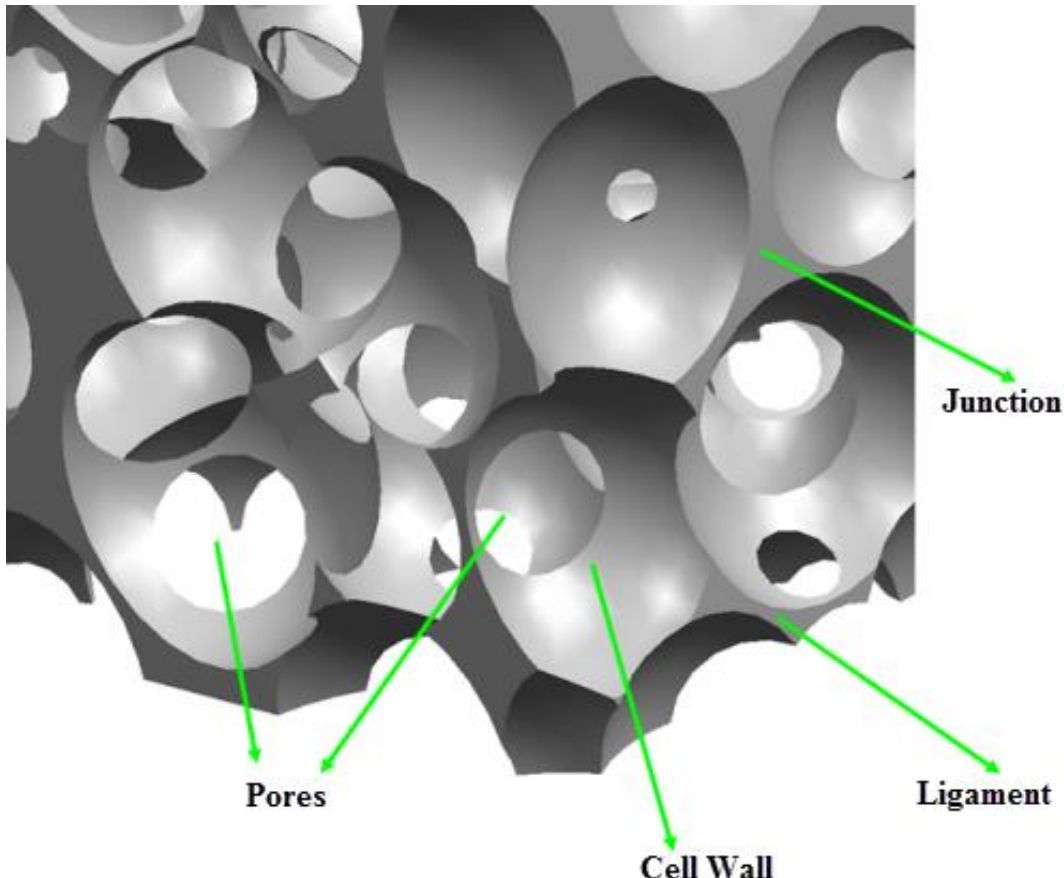


Figure 3.9 : A close view of the CAD model of a sample porous structure.

In summary, porous structure with spherical cell shapes can be generated in two main steps. In the first step, an ensemble of spheres is constructed by initially creating randomly generated spheres that overlap with each other. After generating sufficient number of spheres to cover the desired model space, sphere generation is ended and the final porous structure is obtained through a volumetric subtraction process as shown in Figure 3.8 by corresponding CAD models. Finally, basic structural items of a cellular solid obtained through foam generation process are illustrated in Figure 3.9. According to that, pores, cell walls, ligaments and junctions are clearly distinguished from in the figure.

Pores on the cell walls are formed due to intersections between the spheres. As the overlapping ratio increases, pore sizes also increase. Ligaments, on the other hand, is

formed by the volume retained between the non-intersecting neighbor spheres. Therefore, non-overlapping ratio value that control the minimum distance between neighbor spheres of a target sphere controls the ligament size in the porous network. Formation of junctions is due to joining of ligaments at common locations.

In Figure 3.8, transformation of a spherical ensemble into a CAD foam model is presented. Transformation of a spherical ensemble data into an atomistic porous structure is not so different in the manner that spherical ensemble volume, this time, is subtracted from an atomic crystal system instead of a solid volume. In other words, the atomistic models of nanoporous materials are generated by removing atoms which are encapsulated by the volume of spherical ensemble. The resulting structure is a sponge-like cellular system through which the ligaments are randomly oriented and located. Figure 3.10 demonstrates several examples of nanoporous systems with different porosity values.

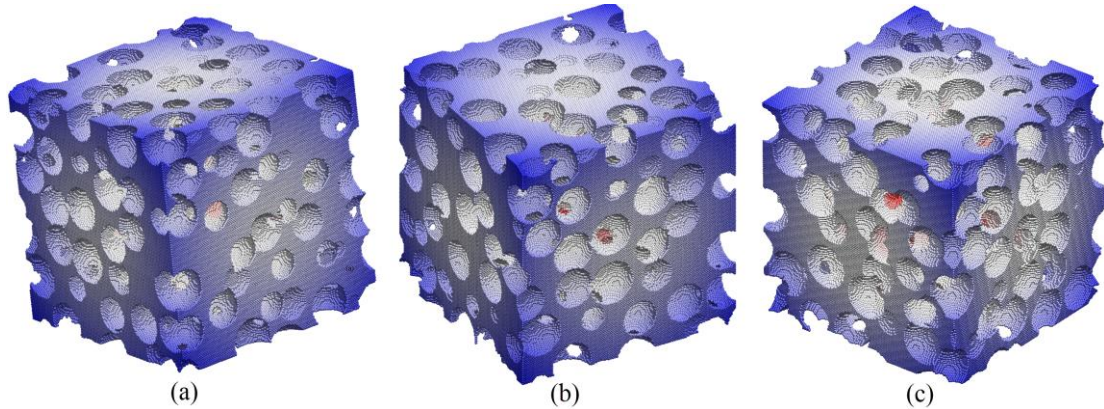


Figure 3.10 : An example of nanoporous models with different porosities (a) 66% porosity, (b) 70% porosity and (c) with 72% porosity.

In summary, the main idea in the generation of porous atomic structure, after the central coordinates and radii of spheres in the spherical ensemble are obtained, is the deletion of group of atoms from a pristine solid block of atoms which are created within a specific lattice system. The group of atoms that would be removed is determined by the spherical volumes intersected with each other and located in the main pristine block. LAMMPS code, which has been used for MD simulations, enables users to create the pristine solid block of atoms and then to remove the group of atoms staying inside spherical volumes defined by central coordinates and radii.

3.4 Numerical Experiments

By employing nanoporous generation method described in the previous section, several test specimens with different porosities were generated to investigate the mechanical behavior of nanoporous structures. In this regard, six different nanoporous models with porosities 0.66, 0.70, 0.72, 0.75, 0.77 and 0.78 were generated by varying overlapping ratio parameter which control the amount of intersection between spheres as explained in the previous section. Parameters that were employed in the generation process of the nanoporous specimens are given in Table 3.1 together with the characterization results of the specimens. According to that, radii of the spheres used in the porous network varies between 2nm and 30nm. The other important parameter not shown in Table 3.1, non-overlapping ratio, was kept constant with the value of 1.1 for all specimens. Beside this, the minimum number of neighbor spheres placed on each target spheres was set to 5 for all samples.

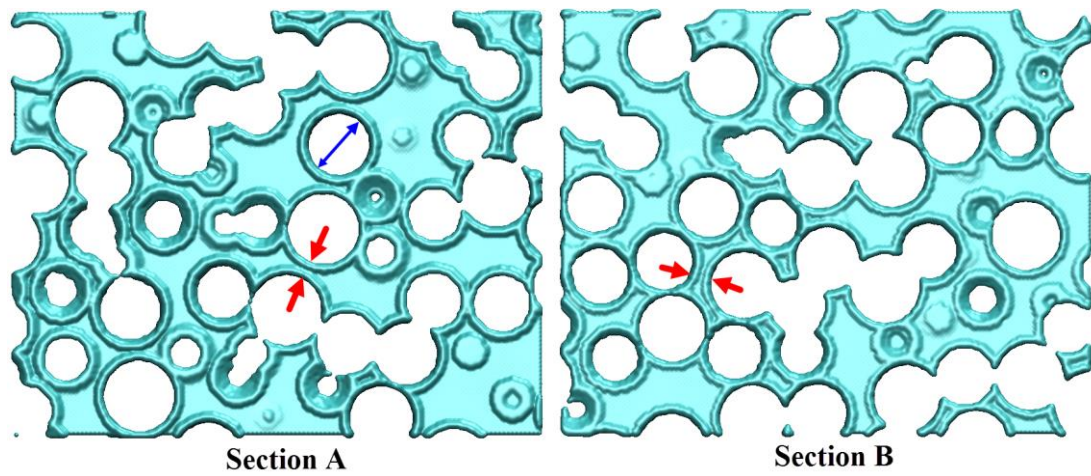


Figure 3.11 : Sectioning characterization of nanoporous samples at different sections.

Generated nanoporous samples were subjected to characterization by serial sectioning and measuring the ligament thicknesses on each sections. Resulting from this characterization study, it was concluded that as the porosity value increases, as interpreted from Table 3.1, the minimum and maximum ligament sizes through the network decreases as well.

The most direct way of varying ligament size, defined here as the smallest width of a ligament, is to vary the range of the overlapping ratio in the algorithm while fixing other parameters. Note that a porosity of 78% represents the upper limit below which a nanoporous structure can be generated without any pre-existing broken ligaments in the structure.

The main objective of this study is to investigate the mechanical response of different nanoporous morphologies varied by modifying porosities instead of investigating a specific nanoporous material under tensile loading. Therefore, as a dummy material type, Aluminium (Al) was selected to be used to construct the atomistic models. Availability of interatomic potentials developed for Aluminium was also a plus factor to select that material as the bulk material. Tensile experiments were conducted numerically on the specimens that was generated with different porosities so with different nanoporous morphologies. For this purpose, MD simulations were employed to simulate the tensile loading on the nanoporous single crystal Al block by using the LAMMPS code [29]. The interactions between Al atoms were modeled by the embedded atom method in interatomic potential [39].

Table 3.1 : Parameters employed in the random sphere generation algorithm.

Pore radius (Å)	Overlapping ratio	Porosity (%)	Minimum ligament width (Å)	Maximum ligament width (Å)
20–30	0.82–0.95	66	105.89	158.84
	0.80–0.93	70	93.33	139.99
	0.78–0.91	72	80.97	121.46
	0.74–0.87	75	55.60	83.40
	0.70–0.83	77	33.22	49.83
	0.65–0.78	78	4.47	6.71

The MD simulations of tensile experiments consist of mainly three steps. In the first step, atomic coordinates are read and energy minimization is performed. In the second major step, the system is equilibrated at a finite temperature to impose thermal vibrations into the system. Lastly, tensile displacements are applied to one end of the atomic structure while the other end is fixed as shown in Figure 3.12(a).

Within the MD simulation of tensile loading applied to the each atomistic specimen, before the application of tensile loading, an energy minimization process is activated to minimize total energy of the system to find equilibrium configurations of atoms. After performing energy minimization on each initial nanoporous specimen, the system was equilibrated at 300°K using the Langevin thermostat for a total of 10 ps at a time step size of 0.5 fs.

Uniaxial tensile loading was subsequently applied to the [1 0 0] direction as the displacement boundary condition on one side of the structure over 5 cubic lattice units (CLUs) with a strain increment of 0.1% that was held constant for 1 ps at 300°K. The other side of the structure was held fixed while periodic boundary conditions were employed on the other sides of the structure. To smooth the noise due to thermal fluctuations, stresses were computed based on atomic forces averaged over 200 time steps spaced uniformly within each strain increment. Calculated averaged atomic forces are summed to find the total force at the cross section of the specimen. By this way, total force (P) as shown in Figure 3.12(a) is calculated for each loading step. Classical continuum equations for stress and strain (i.e., Figure 3.12(b)) are employed to calculate stress and strain values at each load step to generate stress-strain curves for the test specimen.

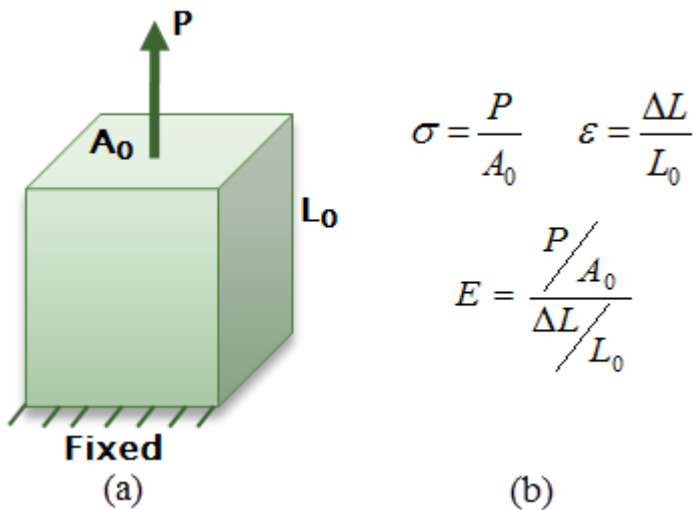


Figure 3.12 : (a) Boundary conditions applied on the specimens and (b) Classical continuum stress-strain relationships where P , A_0 , L_0 are total cross-sectional force, cross-sectional area and length of the specimen, respectively. σ , ε and E are stress, strain and Young's modulus, respectively.

Since size effects have large influence on mechanical behavior, dimensions of the model were selected to be at least ten times the length scale of the largest microstructural feature [100], which was the sphere diameter in this case. Based on this criterion, and considering the sphere sizes and the overlapping ratios employed (see Table 3.1), a block size of 80 x 80 x 80 CLUs was chosen. Convergence was ensured as the stress-strain curves match well for three different nanoporous

structures generated randomly with the same parameter values for the largest overlapping ratios in the algorithm described above.

3.5 Results

As described in the previous section, stress and strain values were calculated by employing classical continuum equations (see Figure 3.12(b)) at each load step. The stress-strain curves obtained for the nanoporous specimens with various porosities under tensile loading are shown in Figure 3.13(a). One of the first observations in these plots is that the slope of the initial linear portion of stress-strain curve, which is called as the Young's modulus, increases as the porosity decreases. Similar behavior is also observed for the yield and ultimate tensile strength values of test specimens, which is also consistent with the general mechanical behavior of macroscopic porous structures [101-103]. Another result that can be interpreted from the stress-strain curves of nanoporous specimens is that the less-stiff behavior emerges following the maximum stress point. This softening behavior observed in all the present simulations after reaching the peak stress is also consistent with previous experimental results reported on nanoporous -Au [104,105]. In their study Biener et al. [61], interpreted the softening behavior as “macroscopic brittle but microscopic ductile behavior,” where the weakest ligament undergoes necking, and its subsequent rupture overloads the adjacent ligaments, ultimately leading to catastrophic failure of the nanoporous-Au structure. In order to investigate the softening region of stress-strain curves, softening rates for each specimen were taken into account quantitatively. In this regard, softening rates or in other words the postpeak tangent modulus were determined from the peak stress point of each stress-strain curve in Figure 3.13(a) and all postpeak tangent modulus values were plotted against the porosity in Figure 3.13(b).

The most surprising observation from Figure 3.13(b) is that the material softens more slowly with increasing porosity from 66% to 72%, but softens much more slowly when porosity reaches to 75% and beyond. This behavior gives a general idea that structures with porosity less than or equal to 72% fail according to the same mechanism, while structures with porosity higher than or equal to 75% fail according to another mechanism. In other words, nanoporous structures with porosities less than 75% demonstrate a different deformation mechanism than the nanoporous

structures with porosities higher and equal to 75% after the peak stress point on their stress-strain curves. In the following paragraphs, the main causes of this difference in softening behavior will be questioned.

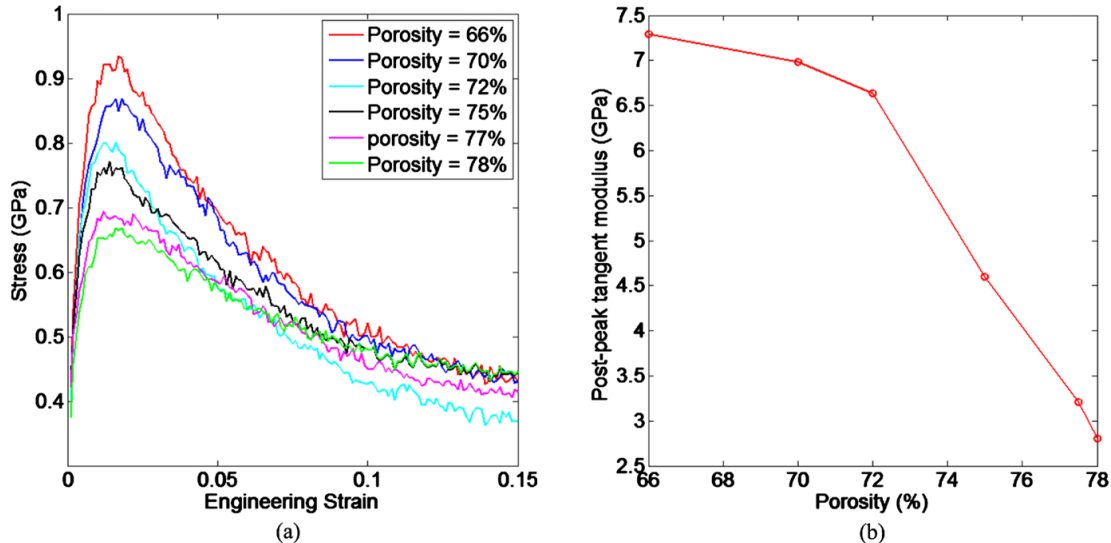


Figure 3.13 : (a) Stress-strain curves for nanoporous aluminum with various porosities; (b) postpeak tangent modulus as measured from the ultimate stress point of the corresponding stress-strain curve in (a).

At first sight, as a morphological comparison ligament thicknesses can be compared to understand the discrepancies in post-peak deformation mechanisms between different porosity regimes. Table 3.1 presents the variation of maximum and minimum ligament widths with respect to sample porosities. According to that, as the porosity increases the the ligament widths logarithmically decrease and, by 75% porosity, the maximum ligament width decreased to below 10nm which is approximately half of the sample with 66% porosity. In this regard, a decrease of ligament widths may be a factor in the softening rate decrease. However, effects of thinner or slender ligaments on the mechanical deformation process in comparison with wider ligaments should be comprehended.

In order to identify the underlying deformation mechanisms responsible for the observed behavior, the von Mises stress on each atom was computed based on the virial theorem for the various structures. The virial theorem introduces the atomic stress concept which is generally employed in the calculation of stresses in discrete particle systems. The atomic virial stress consists of two parts. The first part is the kinetic part, which depends on the mass and velocity of atomic particles. The second part, on the other hand, is the potential energy part that is dependent on the

interatomic forces and atomic positions. Although there is not a consensus about that the atomic virial stress is equivalent to continuum Cauchy stress, virial stress values have been employed to present stress states of nanoporous samples at different strain values only for the purposes of comparison. Calculations of virial stress values were performed within LAMMPS.

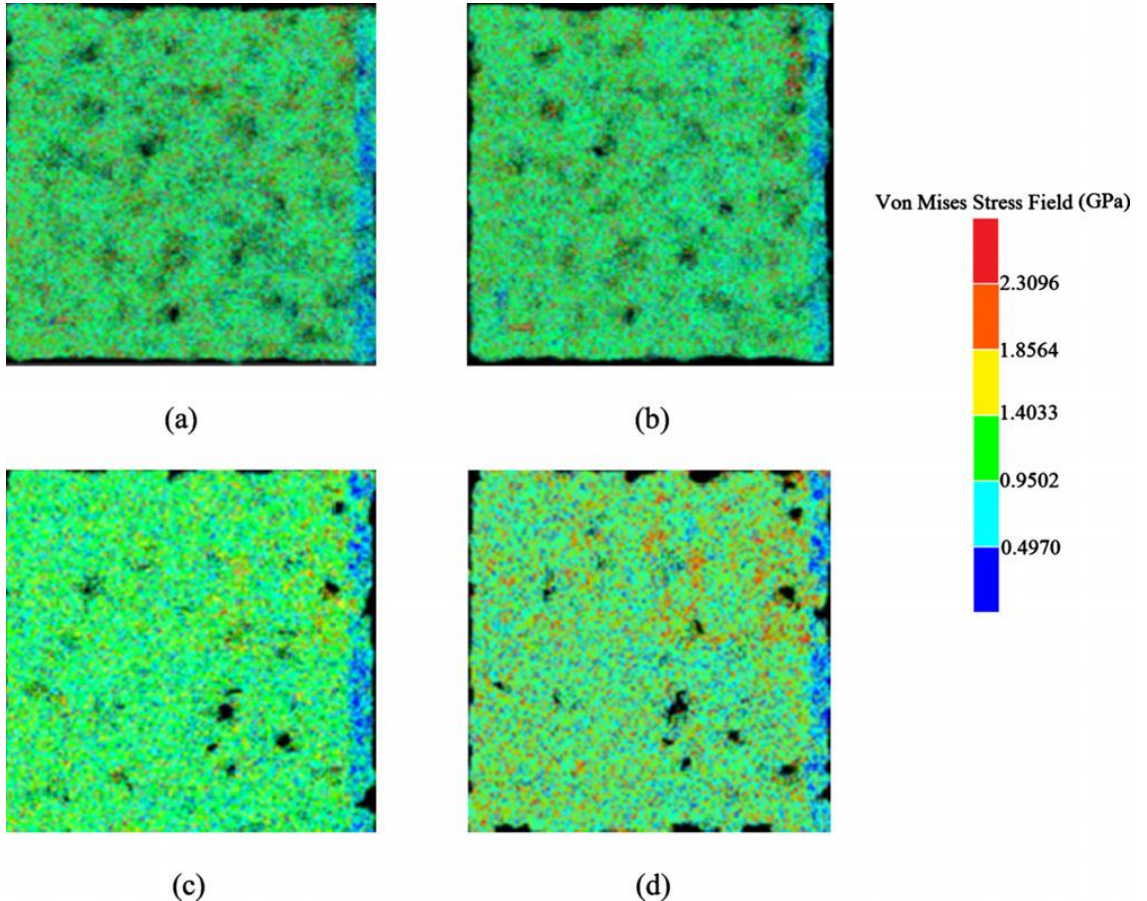


Figure 3.14 : Local von Mises stress field during tensile loading of nanoporous -Al structure with 72% porosity at (a) 1% strain level, (b) 5% strain level, structure with 78% porosity at (c) 1% strain level and (d) 5% strain level.

The local stresses for the structures with 72% and 78% porosities are shown in Figure 3.14 at strain levels of 1.0% and 5.0%, respectively. In the structure with 72% porosity at 1.0% strain level (see Figure 3.14(a)), stresses localize in a small region near the upper right corner as indicated by the red dots. The stresses become greater and more localized in that region as the strain increases to 5.0% (see Figure 3.14(b)). During this time, the smaller ligaments were observed to neck and rupture in the localized region, which causes the larger ligaments to shear, neck, and rupture, finally leading to a crack opening up. In other words, first local failure appears to occur at relatively thinner ligaments by localization of stress around those thinner

ligaments. The reason why the number of stress localized regions is less is that the compliance between the junctions and ligaments are low. Due to low geometrical compliance between ligaments and junctions, the stress flow through junctions to other ligaments is limited, which in turn results in highly localized stress regions in a few areas close to the load application region. Therefore, the stress flow cannot diffuse into the inner regions away from the load application region.

However, in the structure with 78% porosity, the local stresses distribute in a very different manner. As shown in Figure 3.14(c) the number of spots with high local stress, red spots in the figure increases near the upper right corner. As the applied strain increases further, the number of spots with high local stress continues to increase away from the upper right corner, while the stresses in these spots also increase (Figure 3.14(d)). At the strain level of 5.0% where the material has undergone some softening, some ligaments have already undergone necking and ruptured at various isolated locations. This behavior can be explained with the geometric compliance between the ligaments and the junctions in contrast to the case in lower porosity of 72%. As the porosity increases, the degree of compliance between ligaments and junctions increases as well. For this reason, the stress flow through the porous network is more homogenous comparing to the lower porosity structure. Because junctions and ligaments in 75% porosity structure are more compatible, the stress flow is not confined to a limited region and diffuses into the inner regions away from the load application area as shown in Figure 3.14(d) with more evenly distributed red spot areas. At 5% strain, the spots with high stresses scatter throughout the structure (see Figure 3.14(d)), while the rupture of ligaments finally leads to the crack opening in the upper right corner for increased strains.

Because tendency of stress localization is higher for lower porosity nanoporous structures due to less compliant ligament-junction pairs, the stress values should be higher than the values in the nanoporous structure with higher porosity. To confirm this deduction quantitatively, local stress distributions at 5.0% strain, at which the overall stress is approximately equal for the 72% and 78% nanoporous structures, are plotted in Figure 3.15 for comparison. The key evidence is that the tail of the stress distribution of the 72% nanoporous structure is heavier than that of the 78% structure, and the extreme stress values are almost 2 GPa higher in the 72% nanoporous structure.

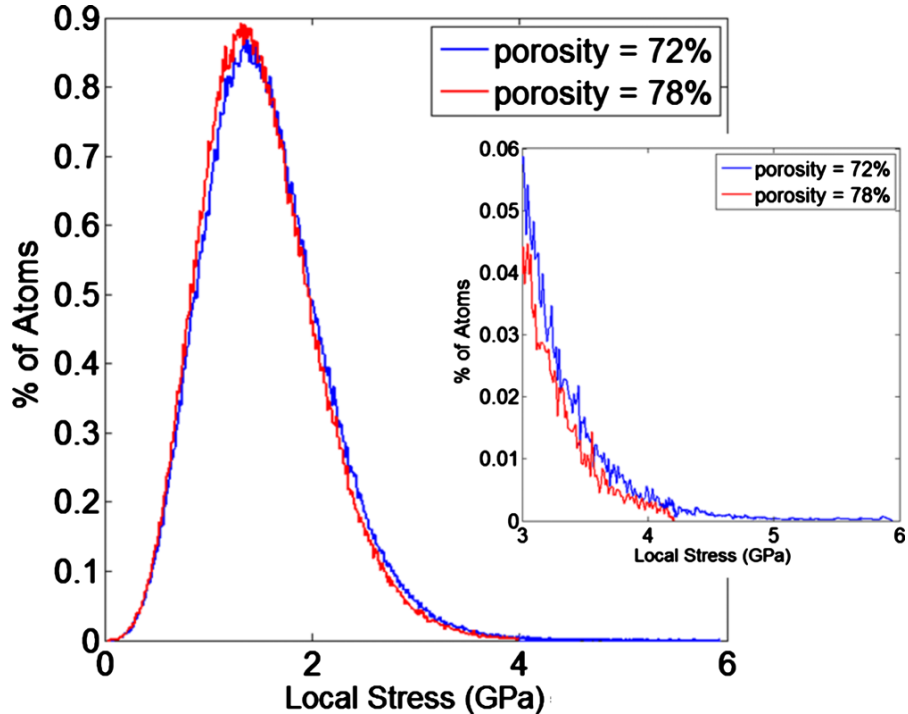


Figure 3.15 : Local stress distributions of the structures with 72% and 78% porosities at 5% strain level.

From the local von Mises stress analysis above, it is clear that stress delocalization is the main cause for slowing down softening once porosity reaches to 75%. The ability to delocalize stress increases with the compliance of the ligaments and their joints, so that stresses can be distributed more effectively throughout the structure. In turn, the compliance of the ligaments and joints increases as their size decreases with increasing porosity. Aside from this main cause, a secondary reason for the slowing of the softening concerns the amount of energy released upon the rupture of a ligament. The smaller the ligament is, the smaller amount of energy is released upon its rupture for the adjacent ligaments to bear, thus reducing the postpeak tangent modulus. The effect of this secondary cause on the softening behavior can be most clearly seen in Figure 3.13(b) by observing that the slope of the postpeak tangent moduli remains relatively constant until the porosity of the structure increases to 72%. In both of these cases, stress localization was observed in their local von Mises plots. This effect is overshadowed by stress delocalization when the structure becomes sufficiently compliant when the porosity increases beyond 72%, and the postpeak tangent modulus becomes greatly reduced (see Figure 3.13(b)).

The findings above were obtained based on np-Al structures generated by varying the overlapping ratios while fixing the other parameters in the sphere generation

algorithm (see Appendix). To verify these findings more comprehensively, structures with different sphere size ranges (20–30, 30–40, and 40–50Å) but almost identical porosities (within 0.01% porosity difference) were tested by using the MD simulations. In addition, all these tests were repeated with tensile loading in the [1 1 1] direction to check the influence of crystallographic orientation. The findings in all these tests were found to be consistent with one another.

3.6 Summary and Conclusion

Nanoporous materials are subset of conventional cellular materials having typically pore diameters in the range of 1-100nm with the porosity generally higher than 40%. The most significant property of nanoporous materials is their ultra-high surface area-to-volume ratios, and combined with their lightweight, they are extraordinary candidates for applications such as catalyzing, sensing, filtration and adsorbing.

Due to their complex morphology, numerical modeling of their atomistic structure is the most challenging point for the numerical investigation of their properties. Because of this issue, a number of numerical studies focusing on the behavior of nanoporous materials was published in literature. In this regard, one of the contributions of this chapter is the introduction of an algorithm for the generation of atomistic models of nanoporous structures.

Nanoporous structures can be considered as the random network of ligaments which are joined with each other at the junctions. In the algorithm developed for the generation of random network of ligaments, cell shapes are assumed to be spherical. The main principle of the proposed algorithm is the creation of an ensemble of spheres in which the spheres are intersected with each other in a controlled manner. Radii and central coordinates of spheres within the ensemble are utilized to remove atoms from a bulk crystalline structure and eventually a porous structure that consists of randomly intersected ligaments. As a product of overall generation process, randomly oriented ligaments with non-homogenous mass distribution along their length are formed and the porosity control on the random network is achieved. Different nanoporous specimens with different porosity values were generated to investigate the mechanical behavior of nanoporous materials.

By employing randomly structured numerical atomistic models with five different porosity values, tensile loading experiments were conducted via MD simulations to examine the deformation mechanism of nanoporous materials. As a result of tensile simulations performed on the specimens with 5 different porosity values, it was found that the Young's modulus, yield and ultimate strength increase as the porosity of the specimens increases. As a further observation from the stress-strain curves of the corresponding tensile simulations, after reaching the peak stress point, all the specimens demonstrate softening behavior with a decreasing rate as the porosity increases. According to this, it was noticed that after a certain porosity value, which is 75%, the softening rate decreases significantly comparing with lower porosity specimens, which in turn indicates a different deformation mechanism at higher porosities. In order to seek the reason behind this difference, von Mises stress distributions at different strain states for two specimens with different porosities were plotted. By the comparison of stress plots, it was shown that the stress distribution was more even at higher porosity specimen comparing with lower porosity specimen. It was concluded that at higher porosity values, ligament and junction sizes become more compliant resulting in more homogenous stress distribution and therefore maximum stress values are less than lower porosity samples. In other words, due to more compliant ligaments and junctions within higher porosity specimens, the load is able to be distributed to higher number of ligaments and junction instead of localizing to a restricted region, which results in lower stress values and lower softening rates.

In summary, by using MD simulations, the softening of nanoporous Al structure under tensile loading was observed to slow down significantly when the width of the ligaments and size of the joints become small enough. In this regime, the relatively compliant ligaments and joints act to spread stress out and prevent it from localizing, so that softening becomes slower. Therefore, ligaments and junctions should be compatible with each other in a way that the stress flow should be free from concentrating or localizing at constrained regions. Considering this finding, mechanical behavior of nanoporous structures can be improved in terms of lower softening rates. In this regard, the results obtained from this study can be employed to better design open cell nanoporous structures to prevent catastrophic failure.

4. STOCHASTIC MODELING AND MECHANICS OF CARBON NANOTUBE NETWORKS

4.1 Purpose

Carbon nanotubes (CNTs) are one of the presents of nanotechnology being investigated due to their extraordinary mechanical, thermal and electrical properties. Carbon nanotube networks feed the idea that the CNTs can be used as the building blocks of new advanced materials utilizing the superior characteristics of CNTs. In this way, nanoscale features of the CNTs can be scaled up to even continuum proportions. In the first stage of this study, 2-D and 3-D CNT network generation methods were introduced by which the geometrical parameters, such as CNT length, chirality, intersection angle and junctional density, can be controlled and a random CNT network is obtained. Then, MD simulations were used to create covalent bonds between the intersecting CNTs, which allow the investigation of the mechanical, thermal and electrical properties of random CNT networks. In the second stage of the study, tensile and shear loading experiments performed on the atomistic models of CNT networks were conducted by the MD simulations to investigate mechanical behavior of 3-D CNT networks that consist of covalently bonded CNTs.

4.2 Literature Review

Carbon nanotubes (CNTs) are one of the extraordinary nanomaterials that are promising candidates for thermal, electrical and structural applications due to their unique properties [106]. Since their discovery by Iijima (1991), thousands of studies, so far, have been adopted to their exceptional high strength and unusual electrical and thermal properties, displaying the desirable nature of their multifunctional capability. Due to combination of remarkable mechanical, thermal and electrical properties of CNTs, they have potential applications in different fields such as material reinforcement, field emission panel display, chemical sensing, drug delivery and nanoelectronics. On the other hand, there are already development studies by NASA for the usage of the CNTs at space applications where lightweight materials

with high strength/stiffness-to-weight ratio are very important to design cost effective structures. In this regard, composite materials reinforced by the CNTs represent higher strength-to-weight ratios than any other presently known materials [107]. Beside that, several companies, Samsung and NEC among others, that are known as electronic device manufacturers have already employed the CNTs in field emission displays [4] resulting in remarkable quality increase in their products and are determined to continue to the investments in this field. Meanwhile, due to their high compatibility to biological medium and their high strength, the CNTs are also exceptional candidates for biomedical applications. For example, conventional composite materials such as fiber-based composites have shown to be inadequate in the replacement of bone and teeth due to insufficient mechanical properties and most importantly due to interfacial instability in biologic conditions causing degradation of the materials. However, it is well known that carbon based materials shows high resistivity against degradation in chemical environments that exist in the body. In this regard, CNT based artificial muscle [6] recently developed is one of the steps towards biomedical applications of the CNTs that offers superiorities over conventional technologies. Moreover, the CNTs can also be employed as drug delivery devices because they could be integrated into the biological tissue locations where the drug delivery would be carried out without any tissue damaged.

Table 4.1 : Experimental studies on the determination of the Young's modulus of CNTs.

Author (s)	Modulus (TPa)	Deviation (TPa)	Test Method	Type
Treacy et al. [108]	1.8	1.4	Thermal vibrations	MWNT
Wong et al. [109]	1.28	0.6	Cantilever bending	MWNT
Krishnan et al. [110]	1.3	0.5	Thermal vibrations	MWNT
Salvetat et al. [111]	0.81	0.41	3 point bending	Bundles
Salvetat et al. [111]	1.28	0.59	3 point bending	MWNT
Tombler et al. [112]	1.2	-	3 point bending	SWNT
Cooper & Young [113]	0.78-2.34	-	Raman spectroscopy	SWNT
Yu et al. [114]	0.27-0.95	-	Tension	MWNT
Lourie & Wagner [115]	2.8-3.6	-	Raman spectroscopy	SWNT
Lourie & Wagner [115]	1.7-2.4	-	Raman spectroscopy	MWNT
Yu et al. [114]	0.32-1.47	-	Tension	Ropes

In the applications where mechanical characteristics of the CNTs play decisive role in the functionality of nanodevices or nanostructures, it is vital to understand the mechanical properties of CNTs. In this regard, there are numerous studies in

literature being both theoretical and experimental focusing on the determination of mechanical properties such as the Young's modulus and Poisson's ratio.

Table 4.1 and 4.2 summarize the literature results for the Young's modulus of different types of the CNTs obtained through experiments and atomistic simulations, respectively. Excluding the studies presented by Yakobson et al. [116], Halicioglu [117] and Zhou et al. [118], all the studies listed in Table 4.2 considered the wall thickness of a CNT as 3.4\AA that is the separation distance between the neighbor walls of a MWNT. Different results for the Young's modulus obtained by experiments as shown in Table 4.1 can be partly attributed to the low resolution at the length scale in which the measurements were made. On the other hand, the Young's modulus calculated through atomistic simulations is approximately 1TPa and the scatter around this value in different studies is not considerable. Yakobson et al. [116] proposed that because modeling of CNT wall buckling phenomena is well described by the assumption of wall thickness as the π -bond length that is 0.66\AA , that value would be more appropriate for the CNT wall thickness.

Table 4.2 : Numerical studies on the determination of the Young's modulus of the CNTs.

Author (s)	Modulus (TPa)	Thickness (\AA)	Poisson's ratio ν	Potential/Method
Robertson et al. [119]	1.06	3.4		Brenner & LDF
Yakobson et al. [116]	5.5	0.66		Brenner
Yakobson et al. [116]	1.07	3.4	0.19	Brenner
Cornwell and Wille [120]	1	3.4		Brenner
Halicioglu [117]	0.5	6.8		Brenner
Lu (MWNT) [121]	1.11	3.4		Universal force field
Lu (SWNT) [121]	0.97	3.4		Universal force field
Hernandez et al. [122]	1.24	3.4		Density funct. theory
Yao and Lordi [123]	1	3.4		Universal force field
Ozaki et al. [124]	0.98	3.4		Tight binding O (N)
Van Lier et al. [125]	1.09	3.4	0.11	Hartree-Fock
Zhou et al. [118]	5.1	0.71		Electronic Band Theo.
Belytschko et al. [126]	0.94	3.4	0.29	Modified Morse

Remarkable mechanical properties of the CNTs such as high axial stiffness and strength as well as significant radial flexibility have been demonstrated by many theoretical and experimental studies. Due to these exceptional properties, the CNTs are expected to be utilized in many nanotechnological applications including composite material reinforcement and nanoelectromechanical device (NEMS) manufacturing.

Another interesting property of CNTs, which is commonly confirmed, is that as the CNTs are subjected to mechanical deformation, their physical and chemical characteristics change significantly. Consequently, in order to understand their exact physics and utilize them in nanotechnologic applications, their deformation mechanisms should be clearly identified and perceived.

In the following subsections, review of several studies which have been reported in the recent years focusing on the mechanical behavior of the CNTs is presented.

4.2.1 Elastic modulus of CNTs

As mentioned before, the CNTs are the most strongest and stiffest material type amongst other known materials on earth. Studies performed so far on the Young's modulus of the CNTs demonstrated values on the order of TPa and showed that the CNTs can sustain high strains without any failure while having highest tensile strength.

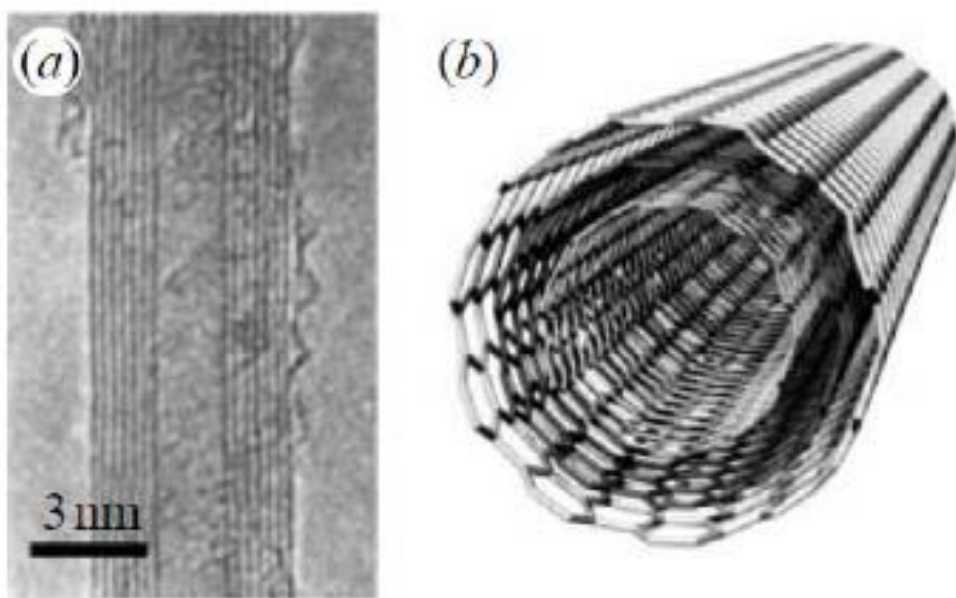


Figure 4.1 : (a) TEM image of a multiwalled carbon nanotube and (b) Schematic of a multiwalled carbon nanotube [108].

Treacy et al. [108] in their study conducted first experiments on the elastic modulus of MWNTs which are shown in Figure 4.1. In their experiments, eleven different nanotubes were tested, and as an average value of the measurements, 1.8 TPa was obtained as the Young's modulus. The individual values of the Young's modulus for different nanotubes ranged from 0.4 to 4.5 TPa. Because of the troubleshooting in

determining precise values of several parameters such as inner and outer radii of the tubes and their lengths etc., a large scatter of the experimental data was observed. Despite the large scatter on the elastic modulus values of CNTs, this study is the first demonstration of that CNT nanomaterials have extraordinary high stiffness. The other experimental and theoretical studies concentrated on the Young's modulus of the CNTs so far presented another interesting finding which notifies that as the diameter of the CNTs increases, the Young's modulus values tend to decrease.

Following the study reported by Treacy et al. [108], by using the same experimental technique, Krishnan et al. [110] performed tensile tests on isolated single-walled nanotubes to determine their Young's modulus. In their study, an ensemble of 27 test specimens, which is larger than the one employed in the study by Treacy et al. [108], was used and the average value of the measurements was reported as 1.25 TPa, which is very close to the in-plane stiffness of graphene layers.

4.2.2 Tensile strength of CNTs

There exist several difficulties in the strength determination experiments. One of these is the issue of precise measurement of the stress on nanoscale structures. The other problem is to obtain high-grade defect-free carbon nanotubes with sufficient length to be tested. Due to this kind of difficulties, experiments to measure tensile strengths of nanotubes are very intriguing.

First experimental study focusing on the determination of ultimate tensile strength and strain values of MWNTs, which were manufactured by arc-discharged techniques, was performed by Yu et al. [114]. In their work, they conducted tensile loading experiments of the CNTs by appending two opposing tips of the CNT specimen to the atomic force microscope (AFM) tips and then pulling the CNTs from the tips until the fracture of the specimen was noticed. In most of the pulling attempts during the experiments, approximately 50% of attempts, tensile testing was ended due to separation of the CNT and AFM tips from each other before the failure of the CNT specimen, which had indicated the severity of the technical difficulties. Despite these problems, Yu et al. were able to complete tensile tests of 19 different MWNTs. As a result of the tensile experiments of MWNTs, it was observed that the failure of the nanotubes occurred at the outermost layer of the nanotubes, which were directly attached to the AFM tips while the inner walls of the CNTs were not affected by the

tensile loading and came out of the outer wall after the failure of the outer wall as if a sword was pulled from its sheath. Therefore, this kind of failure was named as sword-in-sheath mechanism. The ultimate tensile strength and strain values were reported to be varied in the range from 11 to 63 GPa and between 3 and 12%, respectively. The large scatter in the experimental data was attributed to the differences in the content and the number of structural defects in the outermost layers of MWNT specimens.

Tensile experiments on carbon nanotubes have shown that their tensile failure occurs at strain value of approximately 15% at room temperature. However, in practice where structural defects exist on the CNT structure, failure strain values decrease to 6%. In contrast to these values at room temperature, at higher temperatures above 2000°K, ultimate tensile strain values of the SWNTs go up to the strain values of 280%, which can be called as superplastic deformation or super-elongation. This ductile characteristic can also be noticed at double and triple-walled carbon nanotubes by the strain values of 190%. Hence, even though carbon nanotubes are brittle at room temperature, at high temperatures they represent super ductile characteristics.

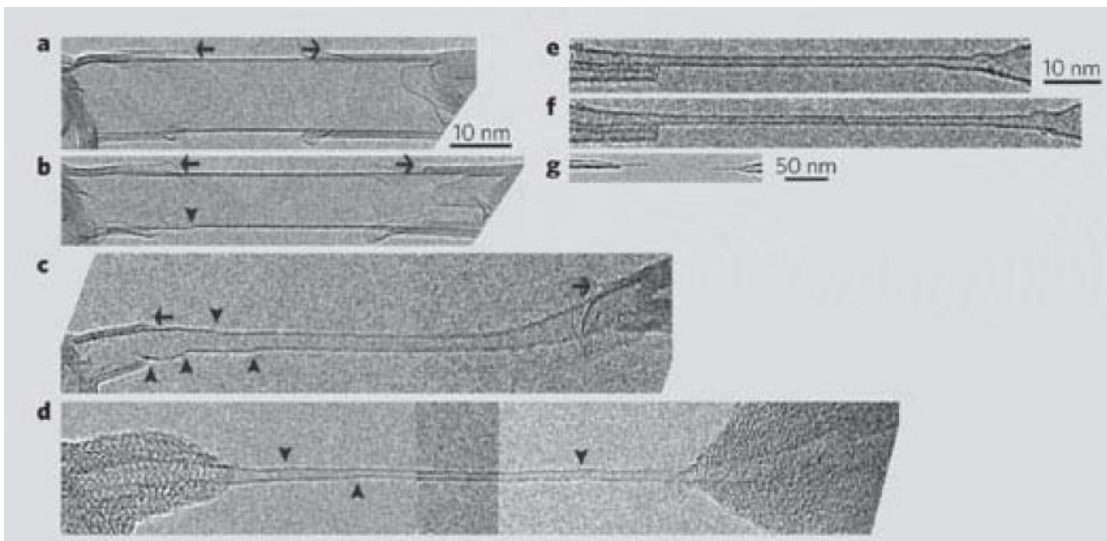


Figure 4.2 : Visualization of tensile loading of a single-walled carbon nanotube by TEM (a-d) Tensile deformation of a SWNT at high temperature. Kinks are showed by arrowheads. (e-g) Tensile loading of a SWNT with initial length of 75nm (e) at room temperature, (f) length after elongation, (g) length at the failure which is 84nm [127].

In their study Huang et al. [127], presented a confirmation of such a remarkable ductile behavior as shown in Figure 4.2 (a-d). As a result of their tensile experiment,

the ultimate tensile strain was determined as 280% with an initial length of 91nm. Beside this, the diameter of the nanotube was decreased from 12 to 0.8nm, showing a decrease of 15-fold. In order to increase the temperature of the nanotube during the tensile loading, the SWNT was heated by a contact bias voltage, so as a result the temperature was increased to 2300°K. Without any addition of heat, in other words at room temperature, the tensile deformation failure was given as shown in Figure 4.2 (e-g).

One of the ways of explanation of superplastic deformation of nanotubes at high temperatures is the formation and longitudinal propagation of kinks which are the geometries resulted from the sudden changes in diameter of the tube. During the tensile deformation of nanotube, some kinks are noticed (Figure 4.2 (b-d) and then they propagate along the tube and vanish at the tube ends. During the propagation of the kinks, the places where the kinks passed narrow just after the transition of kinks. The formation of the kinks was attributed to the existence of structural defects such as 5-7 paired defects, which is also consistent with the theory provided by Yakobson et al. [116].

4.2.3 Buckling and bending of carbon nanotubes

Strength of the CNTs under compressive loading is not as high as their tensile strength due to their high aspect ratio and cavity shape. In this regard, there are many studies focusing on the buckling properties of CNTs. Among these studies, Yakobson et al. [116] presented a numerical study for the buckling behavior of the CNTs shown in Figure 4.3, which yielded critical buckling strain as 0.05 under uniaxial compressive loading. They presented that, under large compressive deformations, morphology of the CNTs changed into reversible patterns which were explained by a continuum shell model. The changes in the morphology were attributed to the sudden energy releases which were noticed in the stress-strain curve as singularity points.

Bending loading of the CNTs also yields interesting deformation mode shapes. For example, a pure bending load applied to a CNT results in change in the shape of the CNT cross section from circular shape to an ellipsoidal shape. As the bending deformation advances, two typical deformation mode characteristics emerge which are ‘kinking’ and ‘rippling’ as shown in Figures 4.4 and 4.5, respectively.

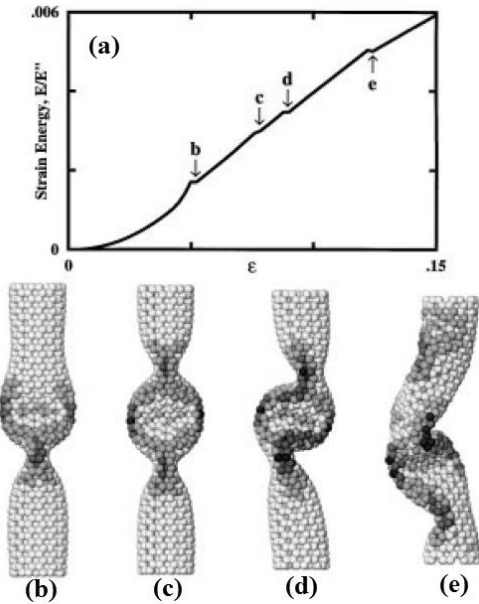


Figure 4.3 : Uniaxial compressive loading of a SWNT with 6nm length, 1nm diameter and armchair chirality of (7,7) [116].

In the study reported by Iijima et al. [128], flexural behavior of both single-walled and multi-walled CNTs under mechanical loads was investigated through HREM visualizations and atomistic simulations. They demonstrated the single and multiple kink formations at high bending angles. The formation of kinks were explained in a quantitative manner by employing atomistic simulations performed with realistic many-body potentials. Moreover, in their study bending deformation was showed to be fully elastic up to very large bending strain even though kinks were formed with high strained regions. And this property was attributed to the ultra-high flexibility of the hexagonal network of carbon atoms in which the resistance to the bond breaking and bond switching up are significantly high to very high strain values.

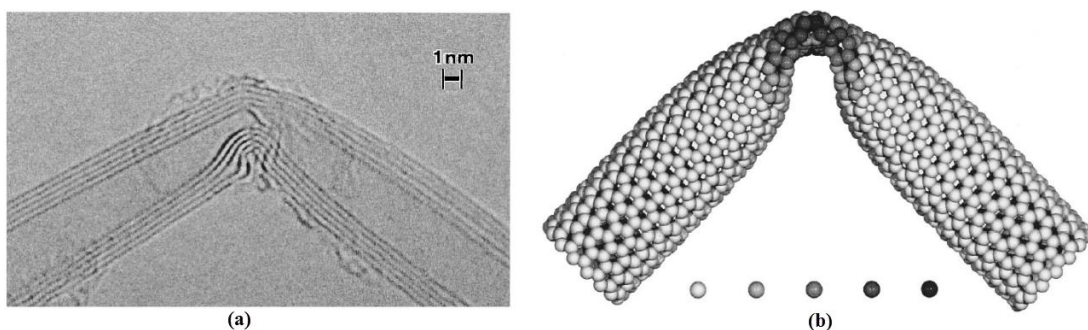


Figure 4.4 : (a) HREM image of kinking formation of a MWNT with 8nm diameter and (b) Atomic configuration of a SWNT with a single kink formation simulated under bending loads [116].

Arias and Arroyo [129], in their study, described the nonlinear elastic behavior of multi-walled CNTs in bending deformation as well as torsional deformation and built-up a power-law relationship to describe distinct deformation regimes including the complicated rippling mechanics.

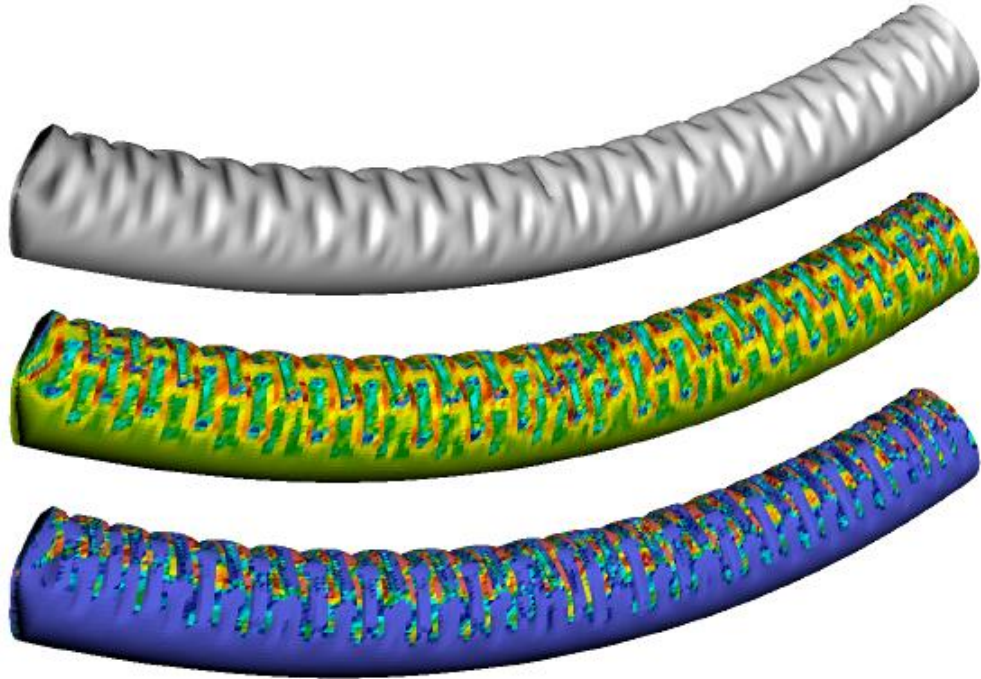


Figure 4.5 : Bending of multi-walled CNTs exhibiting rippling modes of deformation [129].

4.2.4 Studies on CNT Network Materials

In the recent years, the usefulness of the CNTs has been enormously extended by their use as CNT networks through which the CNTs are self-intersected in two or three-dimensional space [130]. Because of their strong electrical conductivity with high light transmittance, CNT networks are attractive alternatives to silicon based macroelectronic devices [131]. Initial studies on 2-D CNT networks deposited onto flexible and polymeric substrates have focused on their electronic and sensor properties [132-133]. Several CNT network based thin films have been proposed to obtain lightweight, unbreakable displays and other flexible electronic devices [134]. Bottom-up controlled production of such networks can also enable them to be used in applications such as sensors, filters, composites and electromechanical actuators [135]. However, CNT networks also display the charming mechanical abilities of individual CNTs to macro-mechanical applications such as nanocomposites, similar to CNTs that are used as reinforcing units in nanocomposites, CNT networks can

also be employed in nanocomposites for both reinforcement and damage detection purposes [136]. In this study, a self-controlled algorithm for generating a 2- or 3-D CNT network consisting of randomly oriented and intersected CNTs is introduced, and a heat welding method is applied to sample networks to obtain covalently bonded networks by MD simulations.

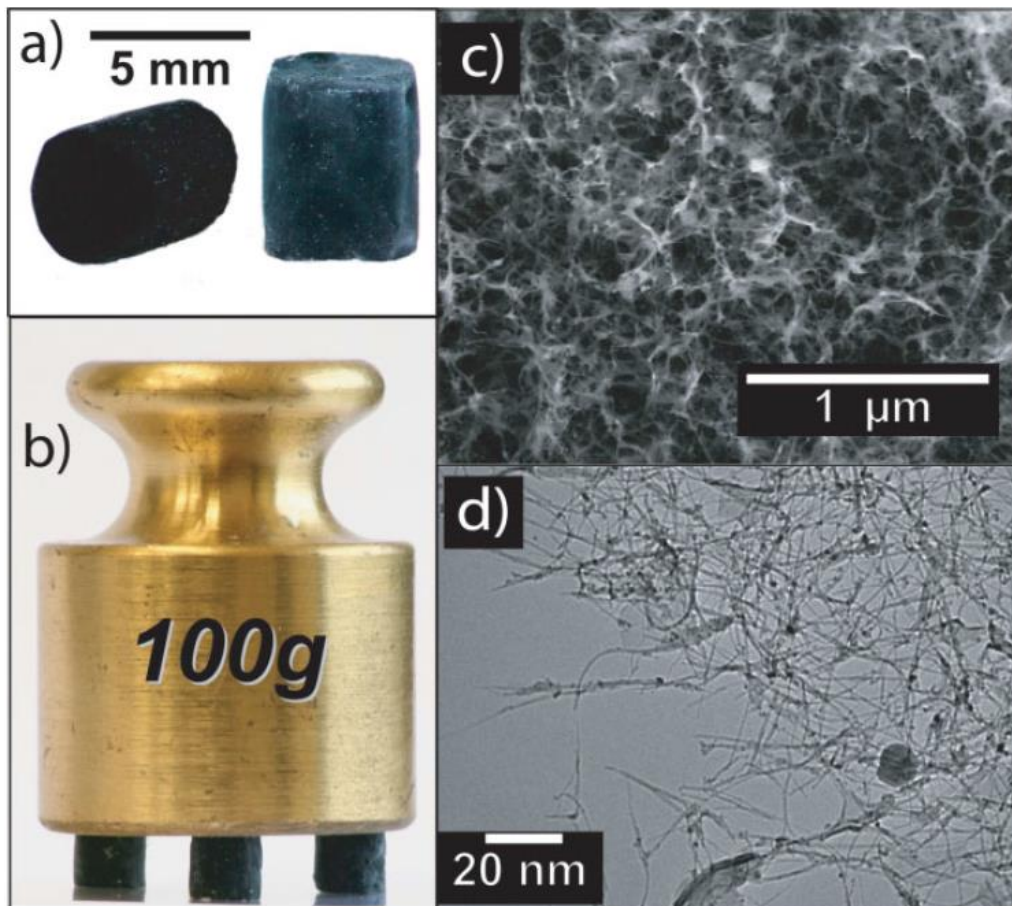


Figure 4.6 : Images of CNT aerogels: (a) Macroscopic pieces of 7.5 mg mL⁻¹ CNT aerogels, (b) Three polyvinyl alcohol (PVA) reinforced aerogel pillars supporting 100g, (c) SEM image of open porous structure of aerogel and (d) TEM image of CNT aerogel [137].

Furthermore, a recently developed CNT aerogel [137] (see Figure 4.6) material that is nanostructured by self-intersecting CNTs forming a random network at the continuum scale is one of the important examples displaying an ultra-high stiffness-to-weight ratio material with conductive properties. Instead of having a reinforcement role in nanocomposites, this material enables the CNT network to constitute a bulk material on its own.

Aerogel materials are generally manufactured by applying critical-point-drying (CPD) or freeze-drying methods on the wet-gel precursors to get rid of liquid content

without destroying the interconnected network structure. Aerogel materials have a cellular structure with very high porosity and ultra-low density. Due to their microstructural characteristics such as being composed of a flimsy network of ensemble nanoparticles, they have very high strength-to-weight and surface-area-to-volume ratios. So far most of the aerogels are manufactured from silica [137] or pyrolyzed organic polymers [137]. Silica aerogels are especially attractive due to their potential applications as ultralight structures, radiation detectors and thermal insulators. Polymer aerogels have potential usage areas such as battery electrodes and supercapacitors [138]. In their study, Bryning et al. presented a new class of aerogels, named as CNT aerogels that consist of percolating networks of CNTs [137]. They demonstrated that an ensemble of CNTs with small diameters including single and a few walled CNTs can be used as a precursor to obtain CNT aerogels which are electrically conductive. Individually CNTs are highly stiff [123] and effectively electrically conducting nanostructures. Therefore, an ensemble of CNTs forms an attractive precursor for the generation of aerogels. As shown in Figure 4.6(b), 3 pieces of polyvinyl alcohol (PVA) reinforced CNT aerogel pillars with total mass of 13mg can support 100g weight which is 8000 times their weight.

Unquestionably, the electrical, thermal or mechanical properties of CNT networks depend on the density of junctions between the CNTs as well as junction properties and impurities throughout the network. It has been shown that electrical conductance and mechanical strength of the junctions may be enhanced by manipulating the junction area, i.e., by increasing the crossing area [139]. In this manner, the algorithm proposed in this study will provide complete control on the junction properties and all the other geometrical features (e.g., CNT length, diameter and CNT intersection angle), which will enable the exploration of CNT networks theoretically or numerically by using much more realistic models.

Generally, CNT networks can be formed randomly by depositing the CNTs locally on the catalyzed substrates by CVD or depositing from CNT embedded polymeric suspensions remotely by using spin coating, spray coating, or vacuum filtration techniques [125-127]. With deposition on the catalyzed substrates, alignment of long CNTs can be more evenly created with directional control, but growth temperatures are high and unwanted byproducts may also be accumulated [128]. Therefore, deposition from solutions with suspended CNTs is much more popular due to the

ability to produce them at ambient conditions, despite the time-consuming steps such as purification and dispersion of CNTs.

Most studies investigating the properties of CNT networks are carried out experimentally following a corresponding production phase. For instance, the thermal stability of CNT networks produced by the dielectrophoresis method on microelectrodes is studied experimentally to predict their uses in electrical applications [140]. Similarly, Wang et al [130] investigated the electrical and mechanical properties of CNT networks with measurements taken *in situ* inside the TEM. In another experimental study, CNT networks are used as reinforcing materials in composites and compared with composites reinforced by dispersed CNTs [141]. Thostenson and Chou studied the damage and strain-sensing capabilities of CNT networks utilized in glass fiber-epoxy composites and have shown through tensile testing that conductive percolating CNT networks can detect the initiation and progression of damage [142]. Several other studies [143-145] exist in literature on the electrical, thermal or mechanical properties of CNT networks carrying out experimental investigations, which, as the other aforementioned studies, inherently require equipment of manufacturing and testing. On the other hand, the majority of computational studies focused on the investigation of individual CNTs and their nanocomposites [146-149]. Due to the lack of a proper method for the generation of random CNT networks and computational limitations, there is a limited number of studies that use numerical models and computational methods for the investigations of CNT networks. Moreover, existing studies [147] that employ numerical network models mostly use ordered networks which do not include the geometrical irregularities and other possible imperfections, such as bond re-arrangements, at junctions. Furthermore, in these models, only one type of junctions are modeled. A recently published study [150] investigates the mechanical behavior of short single-walled CNT (SWNT) aggregates composed of randomly dispersed non-intersected CNTs by molecular mechanics.

In the first stage of this section, a quasi-random self-intersected CNT network generation algorithm that enables the control of behavior decisive parameters, such as the CNT length scale, density of junctions and relative angular position, is presented and several example networks with different parameters mentioned above are generated. Following the generation of a CNT network in which the CNT units

are so close together that heating to certain temperatures can yield a covalently bonded network, the MD simulations are carried out to obtain bonded networks. As a result, parameter-controlled covalently bonded CNT network models can be further used within the MD simulations to investigate mechanical, thermal and electrical properties of CNT networks and their co-operating systems (i.e., nanocomposites).

In the second stage, numerical atomistic models, which were generated by the method introduced in the first stage, have been employed in the MD simulations to look into the mechanical characteristics of CNT networks under tensile loading. In order to examine the effect of cross-link density per CNT on the mechanical response, different CNT network models with different cross-link densities have been prepared and used in the tensile loading simulations.

4.3 Atomistic Modelling of Heat Welded CNT Networks

Carbon nanotube network materials such as CNT aerogels consist of carbon nanotubes randomly oriented and physically interrelated with other CNTs existing in the network. Orientations and interrelations of CNTs in these materials are randomly organized. Therefore, a stochastic algorithm is required to generate representative numerical models. In this chapter, general principles and main steps of such a stochastic algorithm developed within the scope of this study is given. In order to show the applicability of the proposed method, several examples of numerical atomistic models have been demonstrated. Moreover, numerical atomistic models have also been characterized statistically to validate that controlled design parameters are reflected into the models correctly.

4.3.1 General Concepts

The process of generating random networks can be introduced as a process of configuring the network items (in this case, randomly intersected CNTs) randomly in the design space. The placing of network items is carried out under constraints in a random nature. The algorithm explained here is also employed for the generation of random porous networks with spherical cells which is used to model microcellular carbon foams [62].

Before explaining the process of the algorithm, some important concepts that will often be used in the explanation should be defined. First of those, the *design space* is the volume where the CNT items are placed randomly. In 2-D network applications, it is defined as a plane with a thickness that encapsulates the CNT units normal to the plane. The other definition, *library*, is just a conceptual library comprised of all the different types of items (CNTs) that are placed into the design space. Regarding this definition, the CNT units used in the random network can differ in length and chirality (diameter). As a result, distinct CNT items can be reserved in the library and chosen randomly before the placement. Another concept, *target*, which is important when putting the selected item into the design space is the item (CNT) on which other items are closely placed to create an interconnected network. Each target element has a number of *cross-linked CNTs* which are welded on the target element. Finally, the CNT items selected from the library can be placed into the design space only if they satisfy certain *design constraints* imposed on the welded network generation. Without satisfying the constraints, the CNT item remains as a *candidate* for the network and it is called a candidate CNT.

4.3.2 General Algorithm

Network generation is a typical cyclic procedure. At each step of the loop, a new CNT item that satisfies the constraints is placed into the design space. At each step, a number of candidate CNTs are created consecutively and tested against the design constraints until a suitable candidate is found. There are two loops in this procedure. The first loop is for continuation of the generation of the CNT items while the second loop is the sub-loop for generation and validation of candidate CNTs. When one of the CNT candidates satisfies all the design constraints in the sub-loop, the generation process continues with the selection of a CNT from the library in the main loop. The main procedure can be summarized in 5 steps.

- 1) Taking from the library: A candidate CNT item is chosen randomly from the CNT library where multiple CNTs having different lengths and chiralities are stored. For each chirality, the diameters of corresponding CNTs are calculated.
- 2) Rotation and Translation: After randomly selecting CNTs from the library, they are randomly rotated and translated in the design space.

- 3) Checking Constraints: After rotation and translation, the design constraints are checked on the candidate CNT.
- 4) Making a decision: If the constraints are satisfied, the candidate CNT is placed into the design space. Otherwise, the procedure is restarted from the beginning.
- 5) Writing the LAMMPS input data file: Atomic coordinates of each CNT item are written into different files instead of storing them in the memory. Using these files (atomic coordinates), the LAMMPS input data file is written to another file.

4.3.2.1 Line segment representation of CNTs

To save computational time, CNTs are represented by 3-D line segments passing through the central points of the CNTs' cylindrical geometry as shown in Figure 4.7.

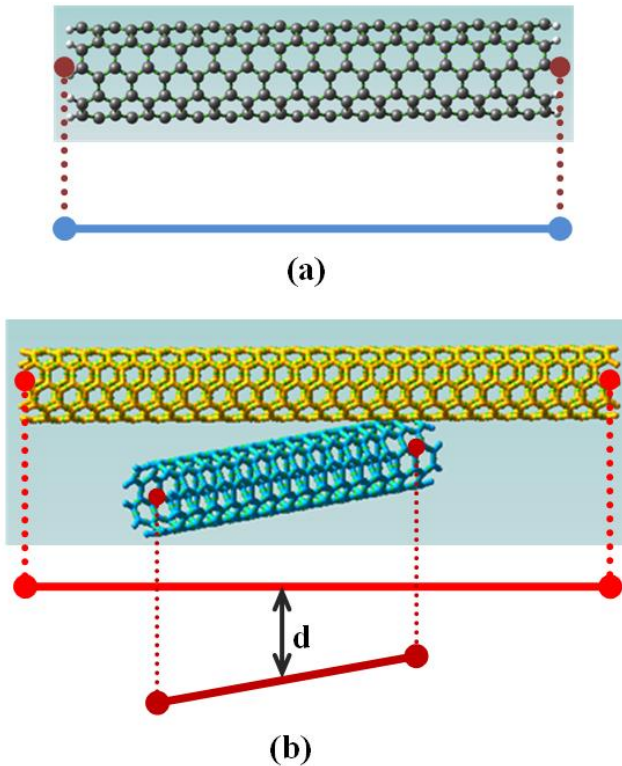


Figure 4.7 : (a) Line segment representation of CNT, (b) Minimum distance between CNTs by using line segment representation.

Each line segment is represented by the coordinates of end points, which are the central points of the circles at the CNTs' end. During the generation process, end point coordinates are also stored and written to a file. Rotation and translation operations are also applied to end points, while all distance and angle calculations are done via the line segments instead of atomic coordinates.

The random points on the line segments are generated via parametric line equations as shown in Eqn.(4.1) where $\{x_0, y_0, z_0\}$ and $\{x_1, y_1, z_1\}$ are the tip coordinates and t is the parameter varying in range [0,1] that describes the line segment between the tip coordinates.

$$x = x_0 + t (x_1 - x_0)$$

$$y = y_0 + t (y_1 - y_0) \quad (4.1)$$

$$z = z_0 + t (z_1 - z_0)$$

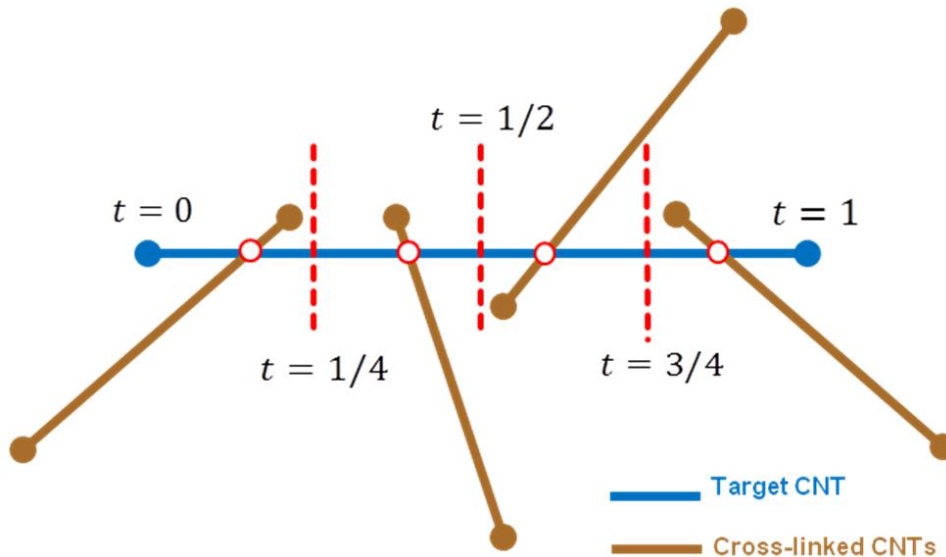


Figure 4.8 : Segmentations of line segments by dividing the segment domain by the number of cross-links which is four in this example.

The line segment parameter t is also used for the further segmentation of line segments to position the candidate CNTs on the target CNT more evenly as represented in Figure 4.8. For instance, a constraint of n cross-links on each target CNT is maintained by dividing the interval of t by n . Thus, the k^{th} cross-link is positioned on the target in the interval of $[(k-1)/n, k/n]$.

4.3.2.2 Target based approach

After putting the first CNT into the design space, it is assigned as the target on which a certain number of other CNTs should be placed so as to create an interconnected network. As a result, the CNT item that is assigned as the target will host cross-linked CNTs. All subsequent CNTs created after the target assignment should be cross-linked with the target until the number of cross-links reaches the maximum value, which is predefined as a parameter. After the placement of all cross-linked

CNTs for a specific target is completed, a new target is assigned and new cross-links are created for this new target.

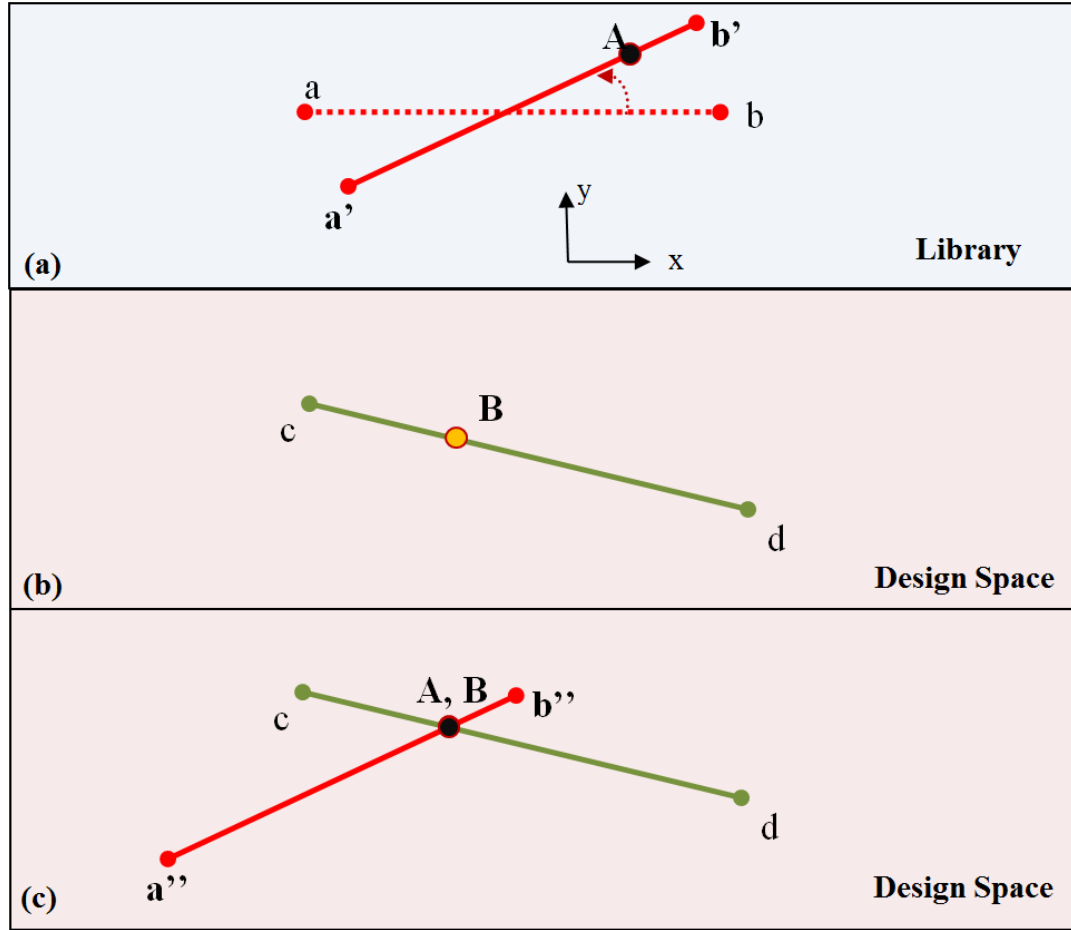


Figure 4.9 : Process of placing CNT candidates into the design space : (a) Rotation of the candidate CNT in library, (b) Target CNT in the design space waiting for intersecting CNT coming from library and (c) Design space after translation.

The target based approach explained above is the philosophy behind the translation operation. Instead of throwing the CNTs into the design space randomly, the translated CNTs are placed in the region close to the target using a systematic method. After rotating the candidate CNT in the library, a guide point (A) is determined randomly on its representative line using parametric functions of that line segment (Eqn. 4.1) as shown in Figure 4.9. Similarly, another guide point (B) is determined on the target line randomly. After determining points A and B, translation is done in the direction of the **B-A** vector. In Figure 4.9, only the 2-D representation is shown. For a 2-D network, since the CNTs are rotated in the same plane, i.e., xy-plane, translation in the direction of B-A vector results in overlapping of atoms in the intersection region. In order to avoid overlapping, an additional

translation (in z-direction) is required to keep the CNTs away from each other in a controlled way. For a 3-D network, it is not necessary to do the additional translation in a specific direction.

Using this approach, the probability of a candidate CNT being accepted is much higher. Thus, the number of candidates generated for the new cross-link in the sub-loop is decreased and so the time consumed is highly decreased.

4.3.2.3 Checking constraints

There are certain constraints for generated candidate CNTs. If the candidate CNT satisfies these constraints, it is accepted as the cross-linked CNT of the target and its atomic coordinates are written to a separate file named with its identification number. The constraints for candidate CNTs are listed below:

1) The candidate CNT should be within a specified range of distance to the target so as to be a cross-linked CNT. It should not be closer than a specified distance to the target, and to the other CNTs created before, in order to maintain a stable welded spot between the target and the cross-linked CNTs. Controllability of the alignment of CNTs during the manufacturing phase by changing the electrical field applied to CNTs [151] highlights the importance of managing the alignments of CNTs in the numerical network model. For this reason, the angle between the candidate CNT and the target CNT, which determines the junction type between two intersecting CNTs, is randomly selected in a predefined range. Line segment representation of the CNTs, as previously explained, are employed to realize the distance and angle constraints for a more controlled network topologies. Mechanical and electrical behavior of different junction types is different as reported in [152-156]. Thus, controlling the type of junctions throughout the network is vital to capture the main characteristics of the network.

2) A specific distance range between the intersection points can also be predefined and set as a constraint. This distance between the cross-links on the same CNT item is an important parameter to determine the flexibility of the CNT segments between cross-links similar to cross-linked polymer networks [157-161]. For this constraint, line segment parameter t is used to control the position of cross-linked CNTs on the target CNT so that cross-linked CNTs can be evenly distributed on the target as shown in Figure 4.9.

Along with these constraints, another constraint can be defined such that the number of the cross-links interconnected with the target CNT should not be less than the specified value. This constraint can be relaxed during the generation process. Due to geometrical difficulties and/or other constraints, sometimes it may be impossible to place a cross-linked candidate CNT around the target. For this circumstance, this constraint is relaxed only for the corresponding target to expedite the generation process. After placing the required number of candidate CNTs on the current target, a new target CNT is selected among the existing CNTs already generated until the number of CNTs in the design space exceeds the predetermined value.

All the constraints which will affect the topology of the network can be arranged in the future according to the detailed characterization results of CNT network materials. Therefore, the proposed method allows experimental characterization data to be employed in computer simulations of the materials behavior. Alternatively, the constraints can be set independently to investigate the effects of several topological parameters such as CNT lengths between two intersection points, the frequency of intersections through the network or the angularity of the intersecting CNTs.

4.3.2.4 Making decision

If one of the constraints explained in the previous section is not satisfied, another candidate CNT is selected from the library, rotated, and translated within the design space before being checked against the constraints. This sub-loop is kept active until a suitable candidate satisfying the constraints is found, while the main loop is active until the specified number of CNTs in the design space is created.

4.3.3 Sample Networks and Welding Procedure

In this section, some examples of 2-D and 3-D CNT network models generated by stochastic target based algorithm explained elaborately in the previous sections are presented. In the network models ultra thin CNTs with (5,0) chirality are employed to ensure the junction formation following the annealing process. In Figure 4.10, the network generation process is shown by increasing the number of CNT units in the design space.

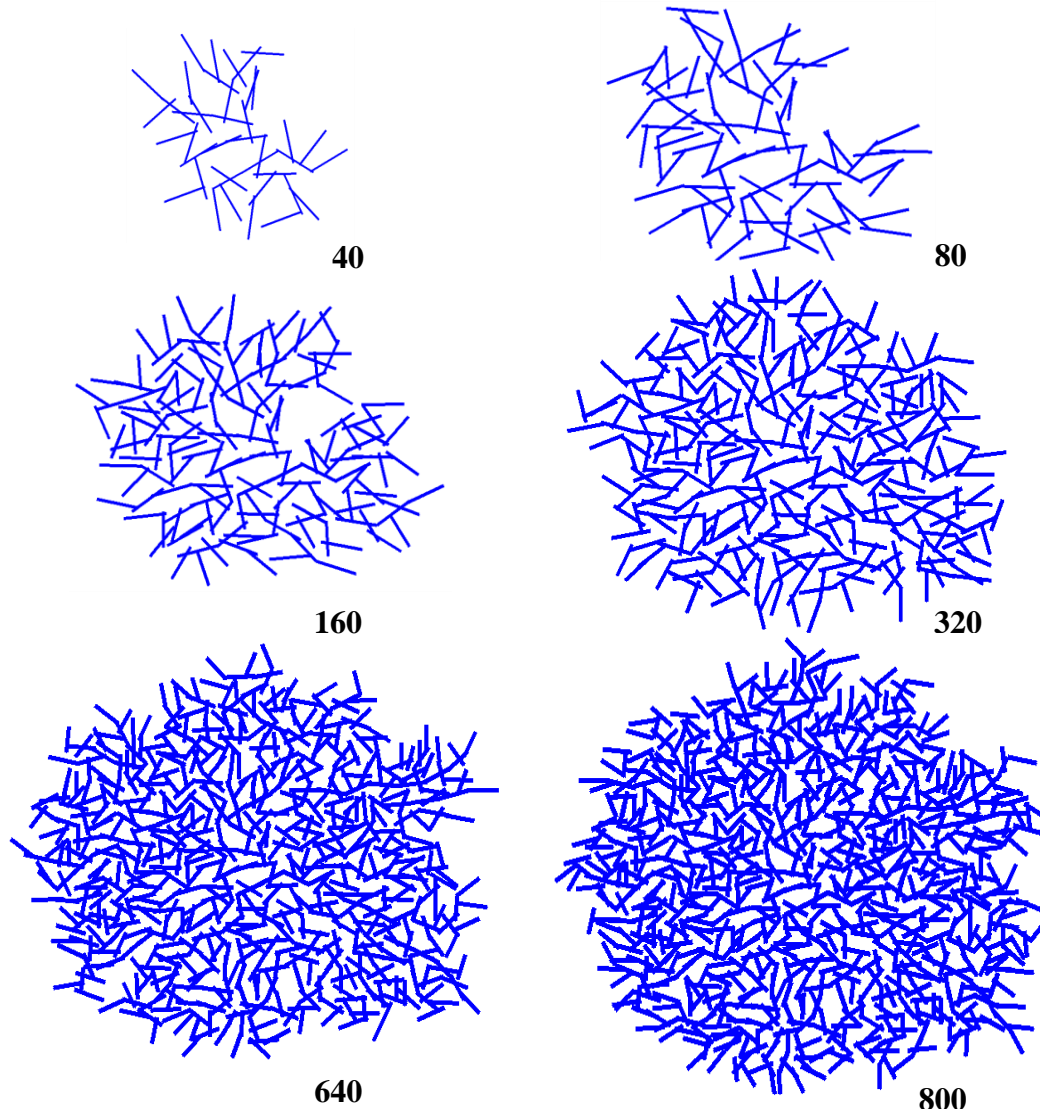


Figure 4.10 : 2-D network samples with increasing number of CNT units.

The network properties can also be changed by modifying the parameters such as the minimum number of junctions per target CNT, minimum distance between cross-linked CNTs and length of the CNT units. Consequently, this controllability of tuning enables to generate CNT networks in different natures. As can be seen in the Figures 4.11-14, several types of junctions (X, Y or T) that play important role on the behavior of CNT networks [162-165] can be observed within the networks randomly. Intersected CNT units are separated before the welding with a wall-to-wall distance (about 4 Å) to avoid van der Waals interaction so that unstable junctions at higher temperatures can be prevented [100, 106].

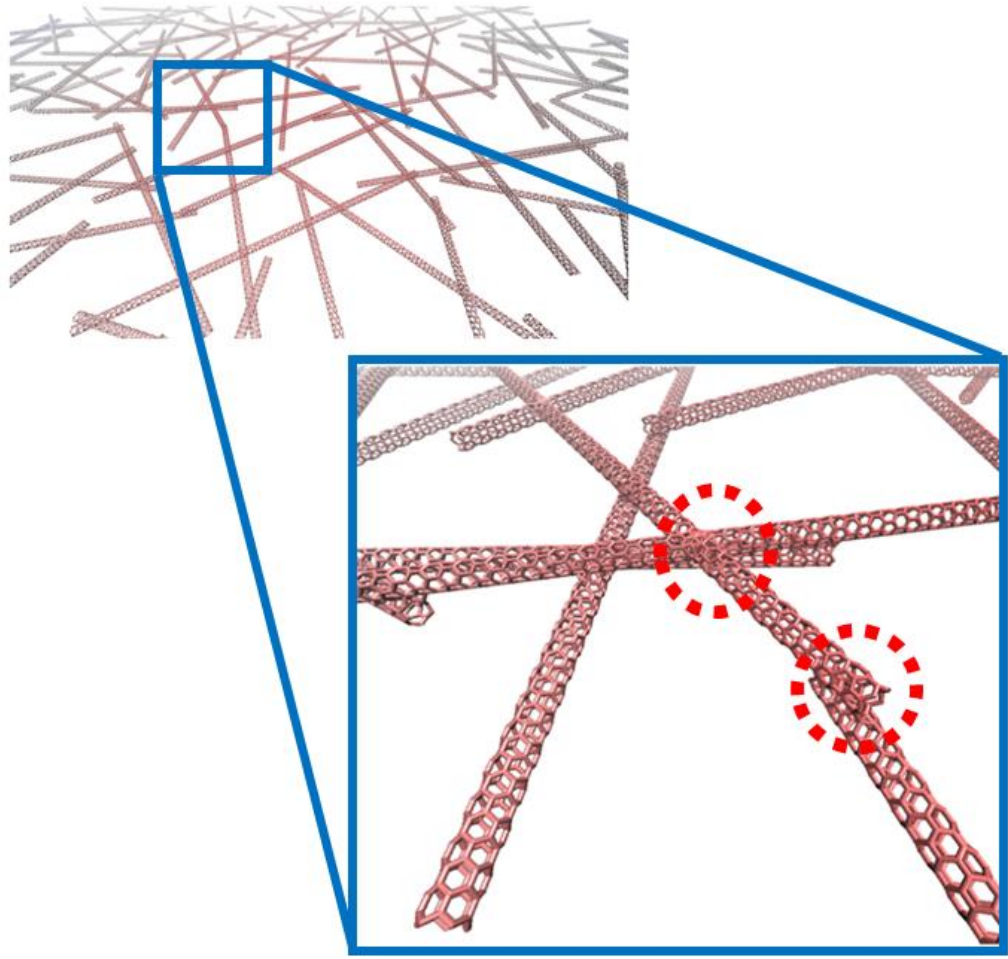


Figure 4.11 : 2-D network sample showing different junction types and spot areas.

The MD simulations in this study are carried out with the LAMMPS code [26]. Interaction between the carbon atoms is modeled by using the Adaptive Intermolecular Reactive Empirical Bond Order (AI-REBO) interatomic potential [41] due to the fact that it allows breaking and formation of covalent bonds. The thermal equilibrium of the system is maintained by Nose-Hoover thermostat and canonical ensemble (NVT) is assigned to the system as thermodynamic characteristic. In order to encourage junction formation at lower temperatures than the referenced temperature values ($2500 - 3500^{\circ}\text{K}$) for heat welding procedure [166], small ratio of atoms in the spherical volume centered at the intersecting points is removed to create dangling bonds and the system is relaxed at 300°K to 600°K . Initially, thermostating is applied to only these spherical welding spots, and then the network is relaxed at room temperature. By this way, stability of bonds formed at junction regions is examined. In literature [167], it is reported that without introducing any imperfections such as vacancies or interstitials, covalent bonds can still be generated but in longer computational time.

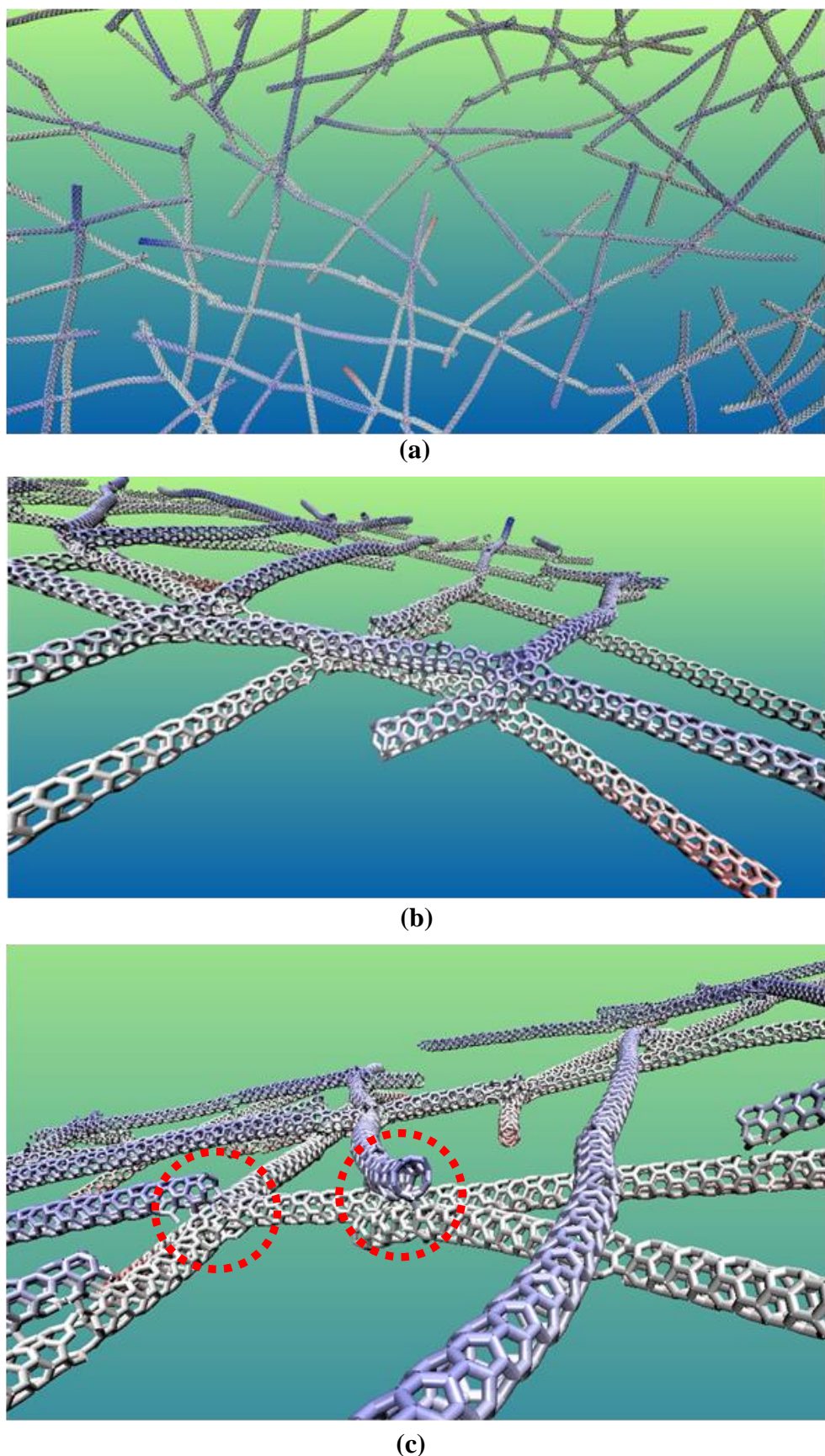


Figure 4.12 : (a) Top view of a welded 2-D network, (b)-(c) Junctions formed after annealing.

Initially straight and non inter-bonded CNTs (Figure 4.11) become curved with the effect of thermal vibrations and stable covalent bonds are formed (Figure 4.12).

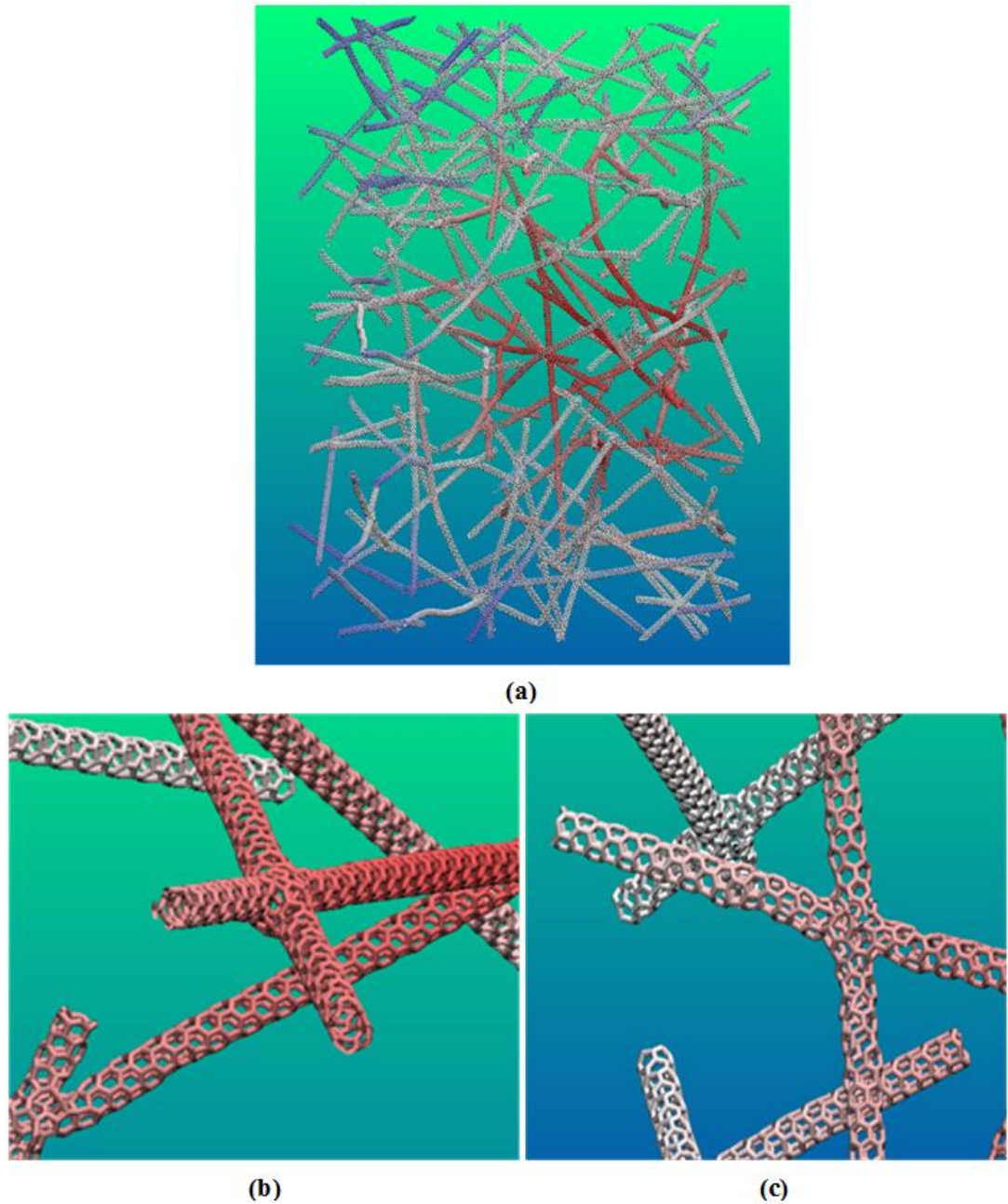


Figure 4.13 : (a)Perspective view of a 3-D CNT network, (b-c) Snapshots of junctions.

Figures 4.13 and 4.14 present some examples of cross-link regions in 3-D CNT network samples after application of welding on the cross-links. As can be noticed from the figures, different types of junctions have been formed following the heating process applied by MD simulations. After heat welding, the atomistic models can be used for the numerical experiments by MD simulations for any purpose.

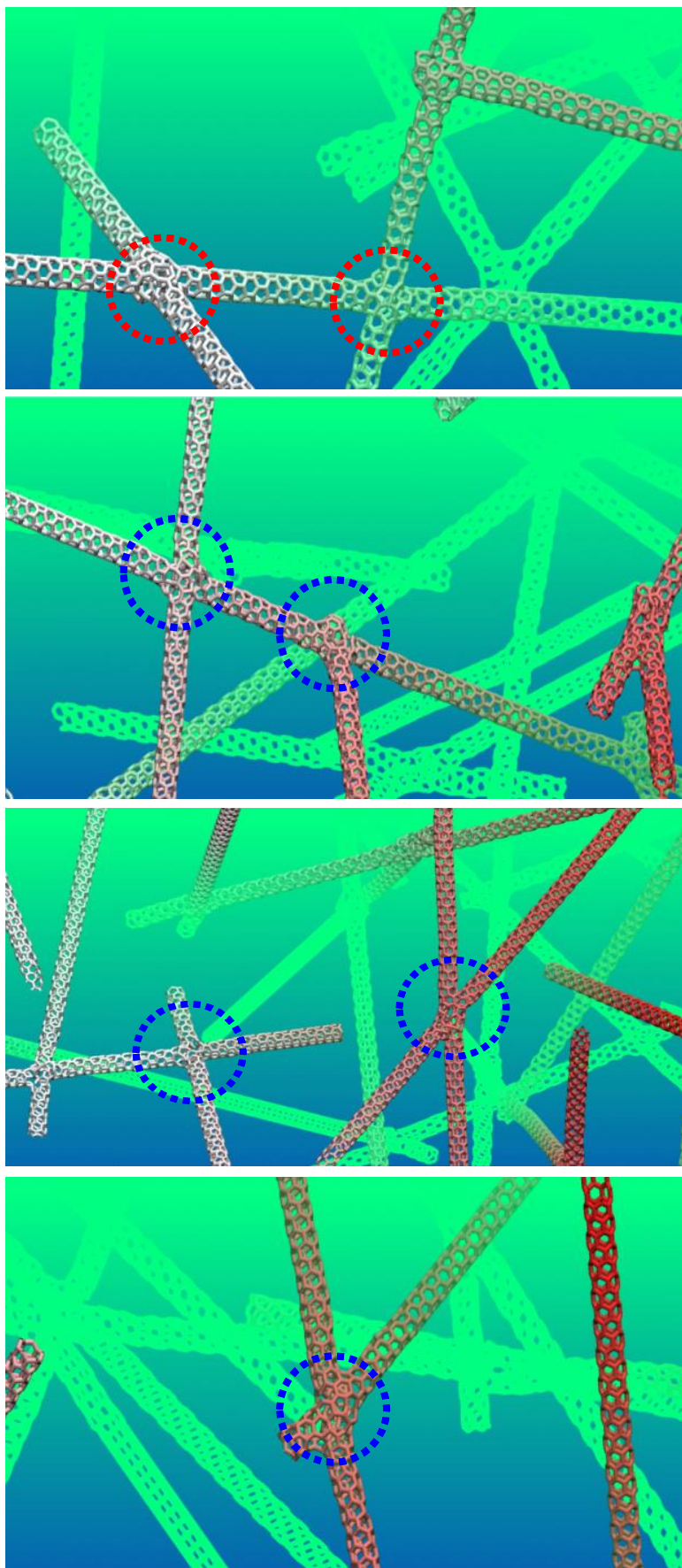


Figure 4.14 : Example of junctions throughout 3-D CNT network.

The proposed method can also be applicable to continuum scale analysis. Employing the line segment representation of the CNTs in the method, the generated network model can be easily converted to a CAD surface or line models, which will enable researchers to carry out finite element (FE) simulations. In this regard, equivalent shell or beam models [168-170] for representing the CNT items can be employed to perform continuum scale analyses. In this way, the time and length scale limitations of classical molecular dynamics simulations can be overcome.

As shown in Figure 4.15(b), CAD cylindrical surface data can be obtained from the line segments of the CNTs and this surface data can be employed to create FE model of the CNT network. The welding at the intersection region can be modeled by beam elements having suitable stiffness values which can be found in literature [171].

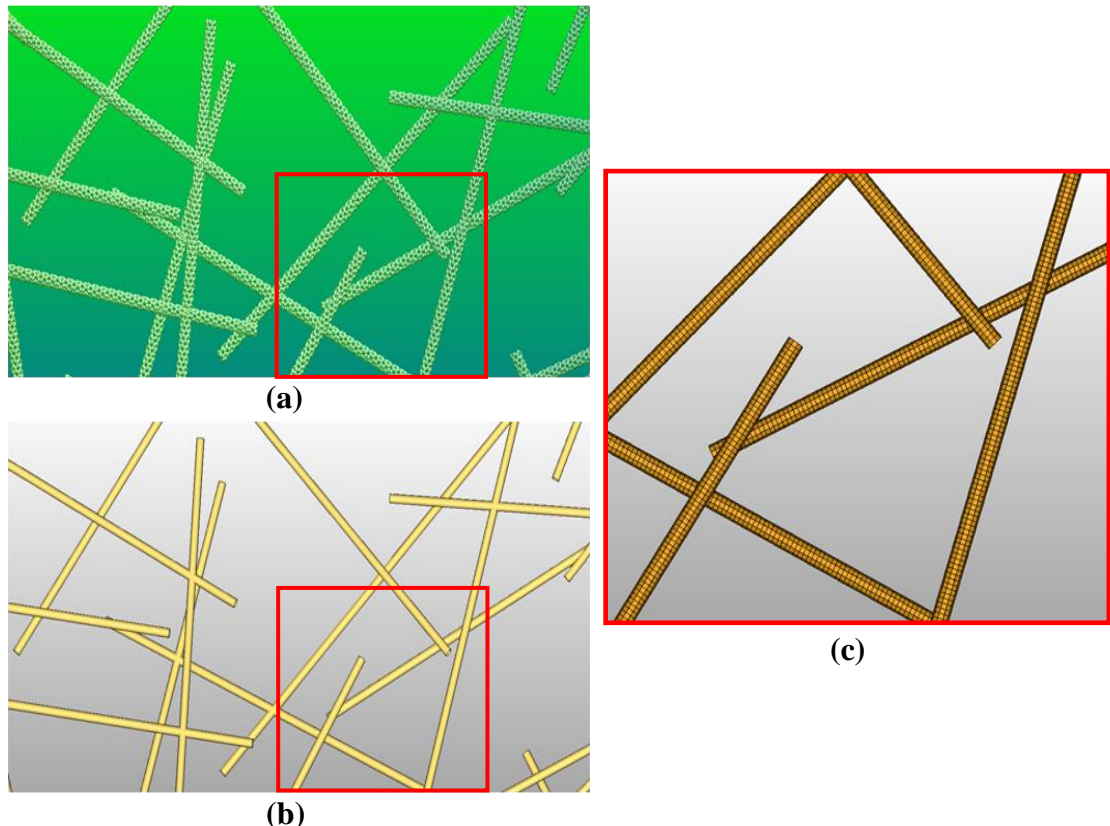


Figure 4.15 : (a) Atomistic view of 2-D network, (b) Surface CAD drawing view of atomistic model and (c) Equivalent FE model of the atomistic model.

4.3.4 Statistical Characterization of Random Networks

In order to verify the effectiveness of the proposed stochastic generation method, we generate 100 2-D CNT networks and check the morphological parameters controlled in the method against the relevant statistics collected from the generated networks.

These parameters include the cross link density, angular orientation of cross-linked CNTs, and distance between two adjacent cross-links. In the verification process, 100 2-D network samples consisted of 100 CNTs of 20 nm in length are realized and statistically characterized.

Cross-link density, as explained in Section 4.3, is controlled by the parameter that specifies the expected number of CNTs cross-linked with a target CNT. For the generated network samples this parameter is chosen to be four for the 20 nm long CNTs.

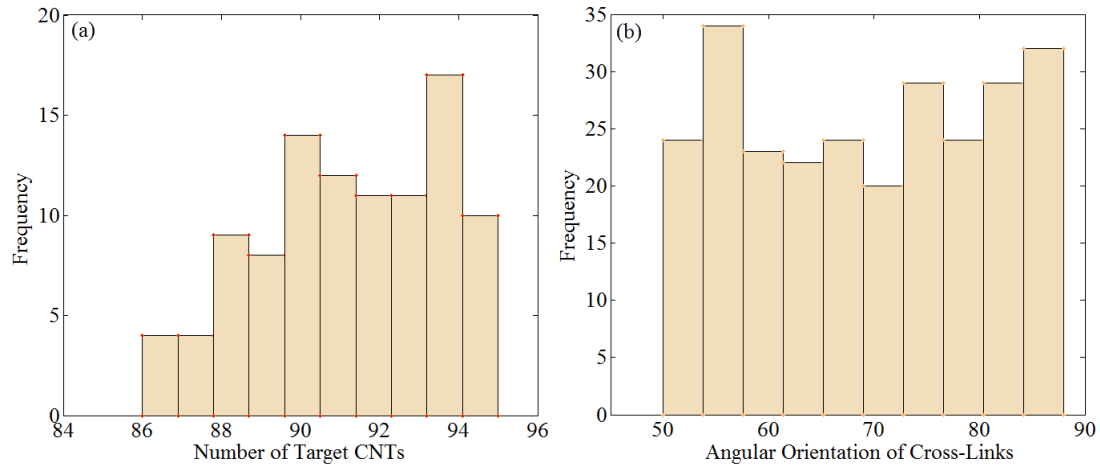


Figure 4.16 : (a) Distribution of the number of target CNTs which are completely cross-linked by 4 CNTs for 100 samples, (b) Distribution of acute angles (in degree) between cross-linked CNTs in a single sample of network.

In Figure 4.16 (a), for the 100 networks generated, the distribution of the number of target CNTs that are cross-linked by four other CNTs in each network is presented. As mentioned before, when geometrical impossibility emerges during the CNT generation process, the controlled parameter of four cross-links per target CNT is relaxed in order to continue to the subsequent steps in the network generation. Therefore, the maximum number of CNTs that have four cross-links will be less than total number of CNTs (i.e., 100 in this case). In the current characterization, the minimum and maximum number of fully covered CNTs are determined to be 86 and 95, respectively, for the 100 CNTs as shown in Figure 4.16 (a). Based on these results, with the proposed stochastic method, it is shown that the cross-link density defined as a design parameter can be maintained fairly well in the generated networks.

For the generated CNT networks, another parameter that is being controlled is the angular orientation of cross-linked CNTs relative to each other. The angular

constraint for these samples is applied in two stages. In the first stage, attempts are made to keep the angles between 65 and 75 degrees. In the event of impasse during the CNT generation process, the first stage constraint is relaxed gradually to the second stage constraint predefined as the range of 45 to 90 degrees. Figure 4.16 (b) illustrates distribution of the acute angles within a network generated is shown to be within the range of 50 and 88 degrees quite evenly between cross-linked CNTs, which shows that the angular constraints can be utilized correctly and efficiently. Consequently, successful application of the angular constraints will yield typical CNT junctions (e.g., X, Y or T).

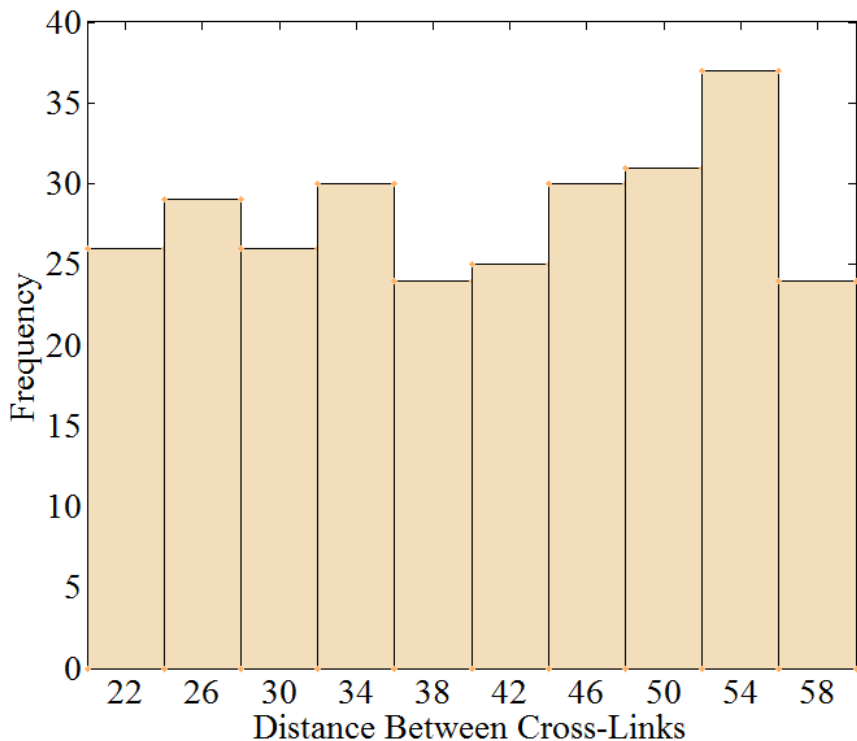


Figure 4.17 : Distribution of distances between cross-links on the same CNT for one of the sample network.

Additionally, the distance between the adjacent cross-links on the same CNT is maintained to be within a predefined range of 20 to 60 nm. The distribution of the distance values of adjacent cross-links on the same CNT within a network sample is given in Figure 4.17 and shows a pseudo-uniform distribution between 20 to 60nm. In accordance with this result, all the cross-link distances can be kept within a specified range.

Figure 4.18 (a) and (b) shows distribution of mean values of cross-link angles and mean values of cross-link distances, respectively, for 100 2-D network samples. While the respective mean values are defined to be 70 degrees and 40 nm, those

obtained from the generated networks are 68.9 degrees and 39.8 nm, respectively. As can be observed from the figures, the scatter around the mean values is very small. Therefore, it can be concluded that the objective mean values can be captured with high precision.

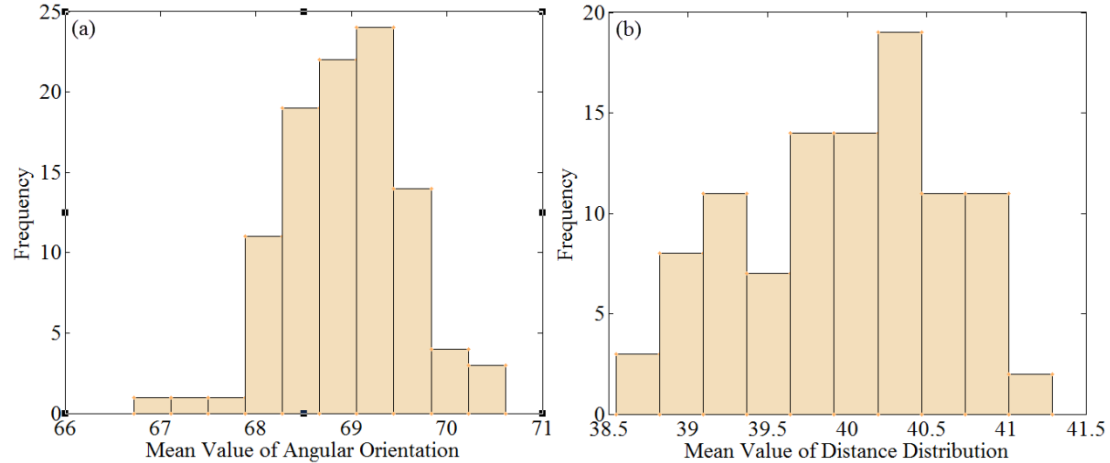


Figure 4.18 : (a) Distribution of mean values of cross-link angularity through 100 samples and (b) Distribution of mean values of cross-link distances through 100 samples.

The above characterization results have demonstrated the effectiveness of the proposed random network generation method. Hence, networks with tailored morphology can be accurately generated by setting the parameters controlled in the method to the appropriate values.

4.4 Investigations on the Mechanical Behavior of CNT Networks

In this section, the studies performed to elaborate the mechanical response of CNT network materials under tensile loading are given. In this regard, numerical specimens which are generated by the stochastic method followed by heat welding process are introduced and numerical settings applied for corresponded MD simulations are provided. Then, the results obtained through MD simulations are presented.

4.4.1 Numerical Experiments

In the previous section, a stochastic algorithm developed for the generation of randomly organized CNT network materials has been explained. By utilizing that algorithm, several numerical specimens have been generated to investigate the mechanical behavior of CNT networks under tensile loading conditions. The

numerical specimens were generated by changing the cross-link density parameter in order to present the effects of cross-link-density on the mechanical behavior of CNT network materials. For this purpose, four different types of CNT network models were generated having cross-link densities per CNT as 5, 6, 7 and 8. Figure 4.19 shows the examples of CNT network samples with 5 and 7 cross-link densities in average.

In all CNT network specimens, CNT units were kept the same having the chirality of (5,0) (armchair) and length of 20nm. Therefore, the only parameter that is varied in the generation of the specimens is the cross-link density. The cross-link density, as mentioned in the previous section, was maintained by segmentation of line segments which represented the CNTs in the design space.

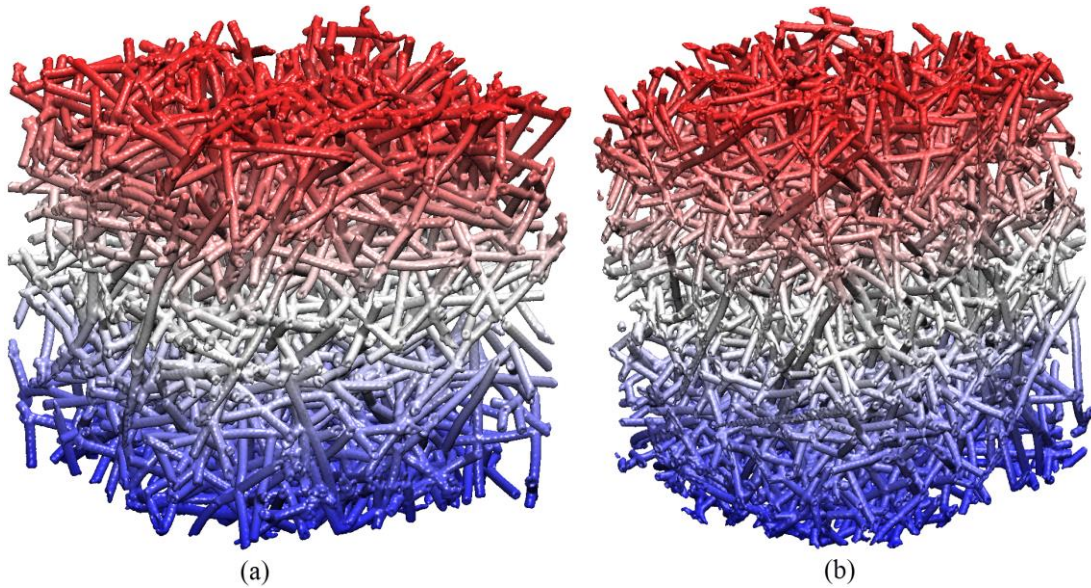


Figure 4.19 : CNT network samples with different cross-link densities, (a) 5 cross-links and (b) 7 cross-links per CNT.

For the tensile loading experiment, as in the case of investigating nanoporous materials focused in the previous chapter, MD simulations were employed to simulate the tensile loading on the CNT network specimens by using the LAMMPS code [26]. The interactions between Carbon atoms were modeled by the AI-REBO potential [41].

As also applied to the tensile loading of nanoporous specimens in Chapter 3, the MD simulations of the tensile experiments are realized in 3 basic steps. In the first step atomic coordinates are read and energy minimization is performed. In this step, atomic coordinates being read are obtained through the stochastic process explained

in the previous section and welding process performed at the junctions. In the minimization process, equilibrium positions of atoms in the systems are received by finding the minimum of total potential energy of the system in successive iterations. In the second major step before the application of tensile loading, for the purpose of incorporating thermal vibrations into the system, or in other words in order to take into account temperature effects, the system is equilibrated at room temperature. In the last part, in order to apply tensile loading, tensile displacements are applied to one end of the atomic structure while the other end is fixed as shown in Figure 3.12(a) in Chapter 3. Therefore, the same tensile loading scheme with the case of nanoporous simulations is followed for the CNT network simulations.

According to 3 basic stages mentioned above, within an MD simulation of tensile loading applied to each CNT network specimen, before the application of tensile loading, an energy minimization process is activated to minimize total energy of the system to find equilibrium configurations of atoms. This process can be thought as removing artificial residual stresses from the system to reach relaxed and more stable equilibrium state. After performing energy minimization on each initial CNT network specimen, the system was equilibrated at 300°K using the Langevin thermostat for a total of 10 ps at a time step size of 0.5 fs. Boundary conditions and stress-strain calculations were performed in the same way as done for nanoporous simulations explained in the previous chapter. According to that, uniaxial tensile loading was subsequently applied in one of the principal directions as displacement boundary condition on one side of the structure over the 1/10 of the total length with a strain increment of 0.1% that was held constant for 1 ps at 300°K. The other side of the structure was held fixed while periodic boundary conditions were employed on all the other sides of the structure. Due to the fact that the strain rate applied to the specimens affects the mechanical response apparently [172], the same strain rate that is 10^9 (1/s) was applied to all specimens. For the purpose of decreasing the noise on the atomic forces due to thermal fluctuations, stresses were computed based on atomic forces averaged over 200 time steps spaced uniformly within each strain increment. At each strain increment, atomic system was equilibrated for 1ps and atomic forces were averaged for each atom in the last 0.2ps-period of that equilibration time. Calculated averaged atomic forces were summed to find the total force at the cross section of the specimen. By this way, total force (P) as shown in

Figure 3.11(a) was calculated for each loading/straining step. Classical continuum equations for stress and strain (Figure 3.11(b)) were employed to calculate stress and strain values at each load step to generate stress-strain curves for the test specimen.

4.4.2 Results

In tensile loading simulations of CNT network specimens, by dumping out the atomic coordinates, snapshots of the system could be obtained and thus the progress of the simulation could be traced. In this regard, several snapshots for the tensile experiment of CNT network specimen with cross-link density of 7 is given in Figure 4.20. According to this, as the number of loading steps increases, elongation of the specimen until the rupture can be visualized and any special deformation mechanisms (if exists) can be observed.

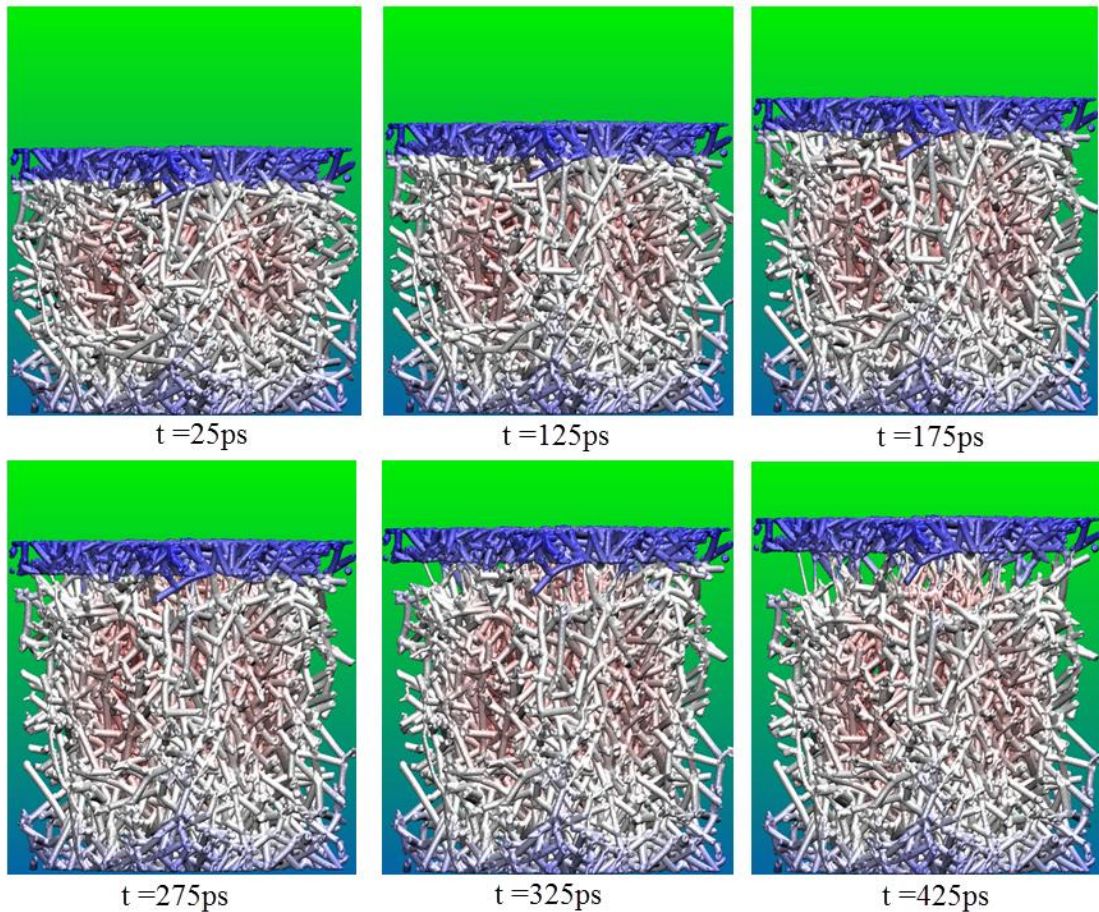


Figure 4.20 : Several instances of CNT network specimen with cross-link density of 7 at different time points in tensile loading simulation.

The most significant observation from the snapshots taken from the tensile simulations is that deformation of the specimens is initiated by rotation or bending of CNT segments in the network around cross-links trying to be aligned in the loading

directions. Therefore, in this initial mode of deformation, the dominant mechanism is the aligning of individual CNT segments along the loading direction by bending around cross-link locations. This deformation phase can be considered as the preparation of the network to fully stretching against tensile loading. However, it should be also noted that some CNTs or CNT segments may already be aligned along the loading direction or bending rigidity of CNT segment around corresponding cross-link may be sufficiently high, which result in initiation of straining of individual CNTs without any initial aligning process. Therefore, the exact deformation mechanism consists of two different modes of deformation occurring simultaneously. In the first aligning mode, CNTs or CNT segments mainly bend around a stiffer region that is a cross-link region consisting of covalently bonded intersecting zones until aligning along the loading direction. In the other deformation mode, namely stretching mode, due to inability of bending, CNT segments get strained in the loading direction.

Because of the random nature of CNT network specimens, CNT segments, which are the part of CNTs between two cross-link points, in the network are oriented randomly, in the total picture both aligning and stretching modes take place at the same time. However, in the initial phase of the deformation, the dominant mechanism is the aligning mechanism due to that most of the randomly oriented CNTs are not aligned in a specific direction. In Figure 4.20, snapshots upto 275ps (including 275ps) demonstrate the deformation of aligning-dominant mode. As the tensile deformation progresses, dominancy of aligning mechanism decreases and the structure transforms into a fully stretched mode in which all CNTs strained in the loading direction without any local bending deformations of CNT segments. In Figure 4.20, snapshots taken at 325ps and 425ps present examples of fully-stretched deformation mode.

It is considered that local bending deformation mode of CNT segments is driven by the bending stiffness of the CNTs in addition to the stiffness of cross-link focal points. As the stiffness of the cross-link focal points increases relative to the bending stiffness of CNT segments, tendency of CNT segment bending around the cross-link focal also increases. For this reason, local bending deformation modes of CNT segments is determined by the struggling between bending stiffnesses of CNT segments and rigidity of cross-link regions which are covalently bonded links

between intersected CNTs generated by the heat welding process in the atomistic modeling phase.

Following the aligning mode, CNT segments come to a point of locking in which they cannot continue to their local bending deformation mode. This situation of CNT segments in which they are fully locked is the initiation of their fully stretched deformation mode. In the deformation mode of stretching, local bending deformation mechanisms are not observed anymore. Instead of local bending deformation, all CNT segments strain individually in the loading direction and the CNT network specimen finally fails after successive failures of individual CNT segments in the vicinity of load application region.

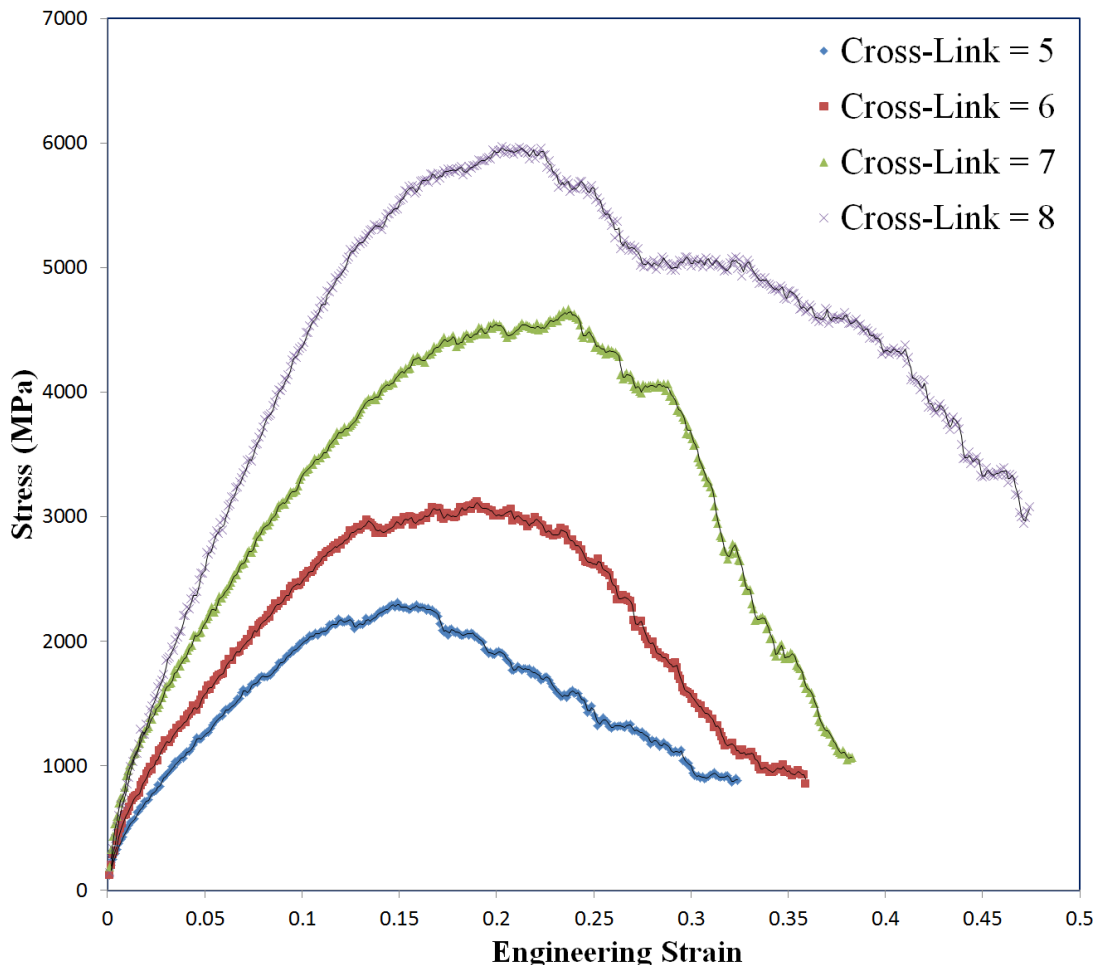


Figure 4.21 : Stress-strain curves of CNT network specimens under tensile loading with different cross-link densities.

As described in the previous chapter, calculations for the values of stress and strain were performed by using classical continuum equations (see Figure 3.12b) at each

load step. The stress-strain curves obtained for the CNT network specimens with different cross-link densities under tensile loading are shown in Figure 4.21.

According to the stress-strain curves presented in Figure 4.21, apparently it is noticed that as the number of cross-links increases the stiffness of the CNT networks also increases. The stiffest specimen, or in other words, the specimen with the highest Young's modulus, is easily determined to be the specimen with cross-link density of 8, while the least stiff specimen has the least number of cross-links per CNT.

As observed from Figure 4.21, the Young's modulus is not the only mechanical property improved by increasing the cross-link density. The yield and ultimate strength values of the specimens also increase with increasing number of cross-link densities. Because there were no obvious transitions from linearity so the values of yield points have been approximated conventionally by finding the intersection of the stress-strain curve with a line parallel to the initial slope of the curve and which intercepts the abscissa at 0.2%. Moreover, ultimate strain, which is the measure of maximum elongation, increases as the cross-link density increases. The quantitative evaluation of the numerical experiments on the CNT network specimens with different cross-link densities is given in Table 4.3.

Table 4.3 : Summary of quantitative results from tensile loading simulations.

Cross-Link Density	Density (g/cm ³)	Modulus (GPa)	Yield Strength (MPa)	Ultimate Strain (%)
5	0.45	14.55	2006	32
6	0.53	18.96	2935	36
7	0.61	24.35	4248	38
8	0.83	37.00	5200	47

As the cross-link density increases, CNT segment lengths decrease while the percolation through the network increases due to increased connectivity between the CNTs. Because cross-links represent the interconnectivity between the CNTs in the network, the load distribution is more homogenous at higher cross-link densities through the network comparing with lower cross-link densities. Due to increased load-sharing capability, interconnection in the network increase as well, which, in turn, increases the number of CNT segments bearing the applied load. Eventually, mechanical properties are improved.

Naturally, as the cross-link density increases, density of the specimens is also elevated. However, stiffness increase rate by cross-link density increase is higher

then density increase rate. Therefore, stiffness-to-weight ratio values continue to increase despite the density increase.

Another interesting observation that can be inferred from the stress-strain curves of the specimens with different cross-link densities is the bilinearity form of the stress-strain curve in the elastic regime. Figure 4.22 illustrates this observation by focusing on the strain values up to 0.12. As can be noticed from the initial portion of stress-strain curve encapsulated by a rectangular region in Figure 4.22, for a very limited strain range, all specimens demonstrate a stiffer initial response to tensile loading. This initially stiffer deformation regime has increased up to approximately 2% strain level for the specimen with cross-link density of 8 whereas for lower cross-link densities the stiffer response range decreases.

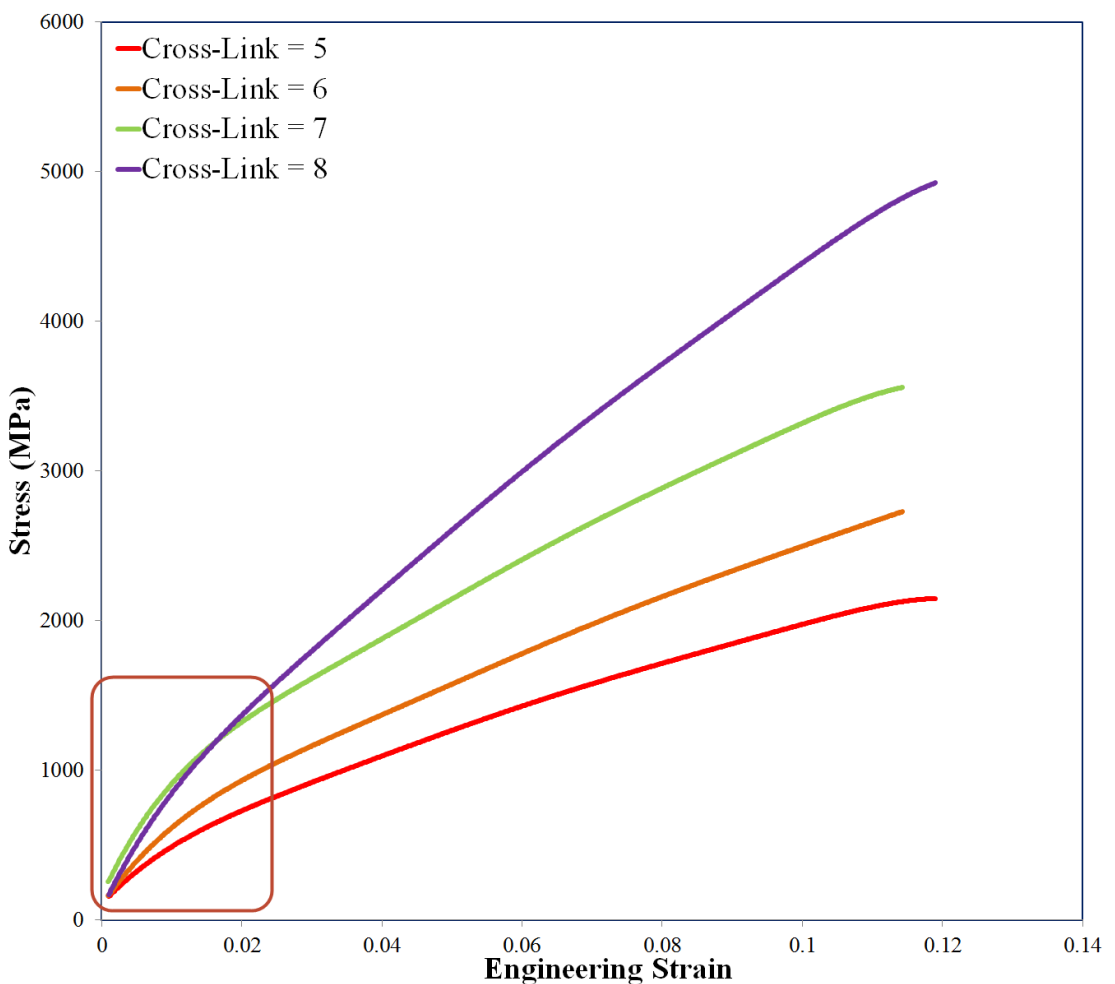


Figure 4.22 : Stress-strain curves of CNT network specimens under tensile loading with different cross-link densities.

Due to the reason that stiffer zone size changes with variations of cross-link densities, the initial stiffer response should be related with the cross-links where the

CNTs are interconnected with each other by covalent bonds. Therefore, this initially-stiffer behavior can be attributed to the stiffer response of cross-link regions that cease after a limited straining of the specimens. This observation can also be explained by a possible requirement of extra strain energy imparted to the covalently bonded cross-links to activate and motivate the deformation.

In order to investigate the mechanical behavior of CNT networks further, another principle loading type, that is shear loading, was applied on the same CNT network specimens with cross-link densities of 6, 7 and 8. Same MD settings with tensile simulations have been used for the those shear loading simulations while the only change is the loading direction.

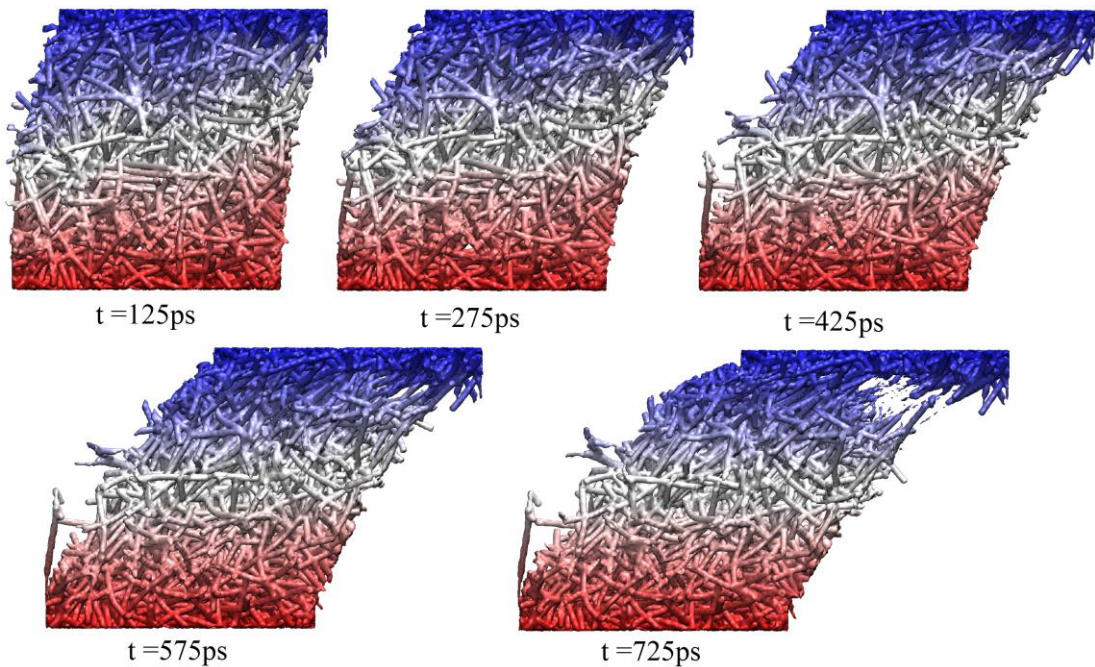


Figure 4.23 : Several instances of CNT network specimen with cross-link density of 6 at different time points in shear loading simulation.

Figure 4.23 illustrates several snapshots of shear loading simulation performed for the CNT network specimen with cross-link density of 6. Examining the shear deformation of CNT networks through MD simulation snapshots showed that displacement of atoms in the shearing direction initiated at the top where the shear loading was applied, while the atoms located sufficiently away from the top were not affected by shearing. As the shear loading is kept actively applied on the specimen, bending deformation of individual CNTs resulted in aligning of CNTs along the shearing direction. When the CNTs that are closest to the loading plane deformed by bending, shear effect transmitted to the lower network regions away from the loading

planes through covalently bonded CNT cross-links. In this way, shear load is transmitted to the all network resulting in collective shear deformation. When the shear loading effect disffuses into overall structure of the CNT network specimen, shear deformation continues with collective shearing of the total system. The final failure of the specimen due to shear loading occurs following the collective shear deformation of the specimen at the region closest to shear plane. This deformation behavior can also be observed from the snapshots provided in Figure 4.23. According to this, at the time point of 125ps, it is clearly noticed that shear loading effect is partially diffused into the network system, so only a portion of the specimen is deformed locally in the shear loading direction. As the loading is kept active, at the time point of 275ps, a larger portion of the specimen comparing to the time point of 125ps is deformed in the shearing direction. At the time point of 425ps, it is seen that shear loading effect has been distributed to the all structure and a collective or global shear deformation is observed. As a consequence of global shear deformation process, at the time point of 725ps, the network structure fails by fracture formations at the upper portion of the specimen close to the loading plane.

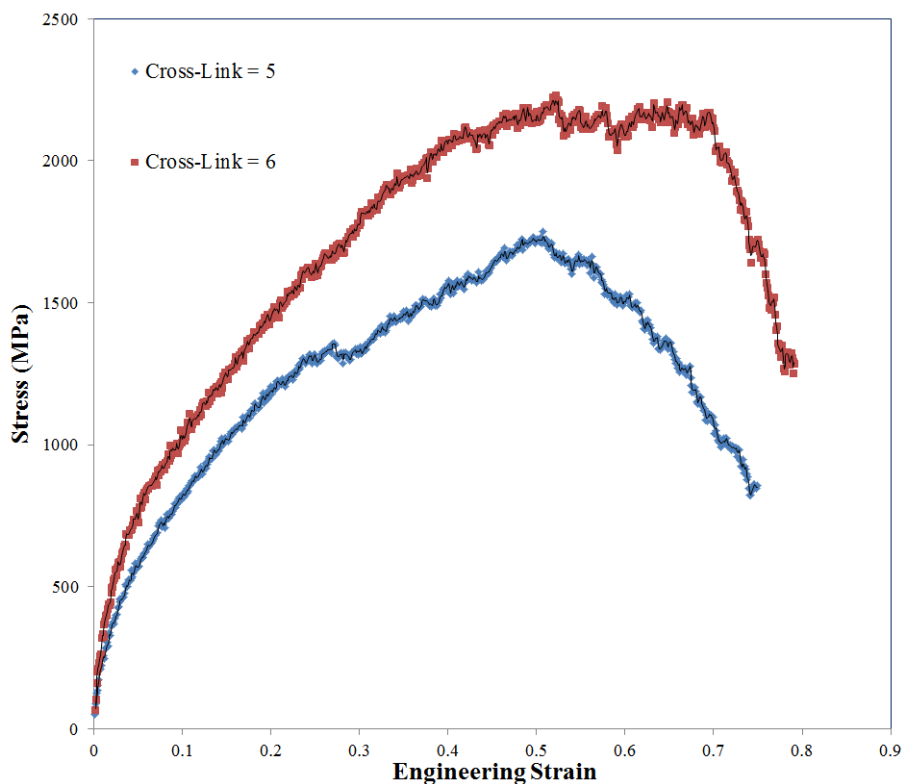


Figure 4.24 : Stress-strain curves of CNT network specimens under shear loading of the specimens with the cross-link densities of 5 and 6.

Figure 4.24 presents a typical stress strain curve for the shear loading of the network specimens with cross-link density values of 5 and 6 up to the point of ultimate strain. According to that, a linear elastic region is followed by a softening region as also observed in tensile simulations. Apart from this, ultimate strain value is determined to be approximately 0.8 for the specimen with cross-link density of 6, which is much higher than the ultimate strain value of 0.36 determined in the tensile simulations with the same specimen. Moreover, it is noticed that cross-link density increase improves the shear rigidity of the CNT network materials as shown in Figure 4.25. Shear yield strength and ultimate strain values of the CNT network materials are also observed to increase with increasing cross-link densities.

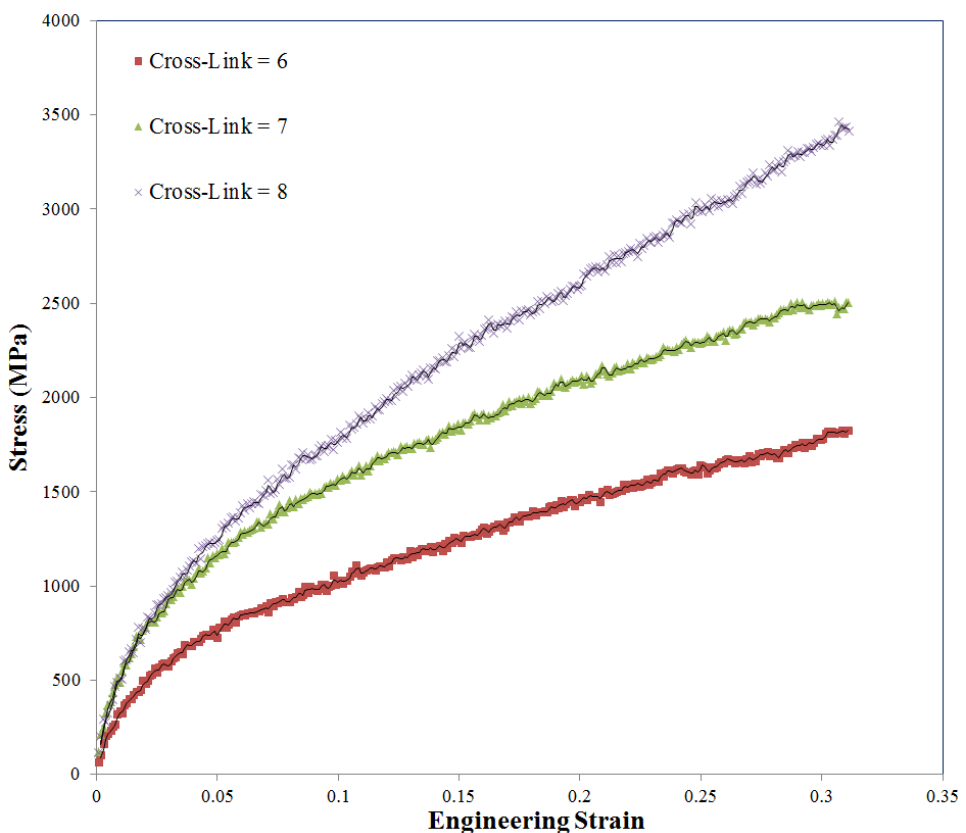


Figure 4.25 : Linear elastic regime of stress-strain curves of CNT network specimens under shear loading with different cross-link densities.

Another finding from shear loading simulations is that, similar to tensile simulations, linear elastic region consists of two linear parts. In this regard, Figure 4.25 presents the detailed illustration of bilinear forms in the stress-strain curves for the cross-link densities of 6, 7 and 8 up to the strain value of 0.3. Although the initial linear elastic region is much more stiffer than the second section, duration of the stiffer behavior is much less than the other phase.

Shear modulus values calculated for two stage values are given in Table 4.4. Quantitative description of shear modulus values for two different stages has shown that shear modulus in the initial elastic phase is approximately 6 times of the second phase.

Table 4.4 : Summary of quantitative results from shear loading simulations.

Cross-Link Density	Density (g/cm ³)	Shear Modulus (1st Stage)(GPa)	Shear Modulus (2nd Stage)(GPa)
6	0.53	24.96	4.45
7	0.61	36.91	5.86
8	0.83	42.60	7.20

The bilinearity of stress-strain relationship in the elastic region, which was also observed in the tensile response of the CNT networks, has been inferred to the required work to activate the individual CNTs to initiate the deformation for their aligning along the shear or tensile loading direction. Because this initial activation of the deformation is related to the stretching of the individual CNTs, it represents a higher stiffness comparing with bending deformation of CNT segments which are observed after the initial activation of the deformation.

4.5 Summary and Conclusion

In this chapter, a stochastic algorithm has been developed to model 2-D and 3-D CNT networks with random geometrical parameters such as CNT orientation and intersection angles. While some parameters are allowed to be random in nature, some parameters such as CNT chirality and length scale, cross-link or junctional density, angular limits for the intersections of two CNTs can be managed independently. In this way, several CNT network specimens with controlled structural parameters were able to be generated. CNT intersecting regions through CNT networks with the proposed method were welded following canonical MD simulations by heating and stable covalent bond formations could be obtained. The sample CNT network models generated by the proposed technique have been provided illustrating that generated samples represent the basic characteristics of CNT networks such as X, Y and T type of junctions formed between cross-linked CNTs. Finally, 2-D or 3-D CNT networks are generated with controllable parameters and can be employed for further mechanical, electrical or thermal studies. Due to the controllability and efficiency on the topological features of CNT networks and simplicity of the generation algorithm,

this CNT network generation method may significantly increase the numerical and theoretical investigations on the CNT networks.

The generation method proposed for the atomistic models of CNT networks is also applicable to continuum scale analyses in order to overcome the time and length scale limitations of classical MD simulations. Due to line segment representation of CNTs in the method, the generated network model can be easily converted to a CAD surface or line models, which will enable researchers to carry out FE simulations. Furthermore, following this study, mechanical, thermal or electrical properties of CNT networks can be optimized by changing the topological parameters, and manufacturing techniques can be developed or improved to produce optimized networks.

CNT network specimens generated by the developed technique have been employed to investigate mechanical behavior of CNT network materials. For this purpose, several CNT network specimens with different cross-link densities were utilized in MD simulations by applying tensile loading. Results of MD simulations showed that mechanical properties of CNT networks including Young's modulus, yield and ultimate tensile strength could be improved by increasing the cross-link density. Total elongation values of the specimens were also demonstrated to increase with cross-link density. Moreover, by tracking of tensile experiments in MD simulations, two different deformation modes, which are the modes of aligning and fully-stretching, have been identified. Moreover, it has been observed that the total deformation of the network is composed of two modes, while aligning mode is dominant at the initial phase up to straining of all CNT segments in the loading direction. In addition to tensile loading simulations, shear loading simulations have also been performed by using the same MD simulation parameters with tensile simulations. Similar to the results obtained through tensile loading experiments, it has been shown that cross-link density increase yields better mechanical performance in terms of shear modulus, shear yield strength and ultimate shear strain. In the regard of deformation mechanisms, it has been illustrated that shear deformation of the specimens starts from the loading plane and diffuses into the all structure in a progressive manner. Furthermore, bilinearity form of the stress-strain curves under shear loading, which has also been observed in tensile loading simulations, has been

quantitatively and graphically presented. According to that the bilinear form of stress strain curves has been explained by the initial activation of deformation

5. CONCLUSIONS AND RECOMMENDATIONS

Day after day nanoscience and nanotechnology bring out new and novel materials that are capable of performing incredibly much better than conventional materials due to their exceptional physical and chemical properties. CNT network and nanoporous materials are amazing examples of those novel materials having nano-organized structures. Both CNT network and nanoporous materials are built up randomly organized structural units that are CNTs in the case of CNT network materials while ligaments and junctions in the case of open cell nanoporous materials. Because of their complex morphologies arising from their random natured atomistic organization, it is highly challenging to numerically model these materials, which avoids increased number of computational experiments exploring their material properties. It would be very beneficial to develop such techniques that enable to generate atomistic models of those materials to investigate the effects of morphological parameters on their material properties. With this motivation, in the content of this dissertation, as the first stage of the study, stochastic models are developed for random natured nanomaterials such as CNT networks and nanoporous materials which have extraordinary properties including ultra-high stiffness-to-weight ratios that make them candidates in a broad range of applications.

In the regard of CNT network modeling, a stochastic algorithm is developed to model 2-D and 3-D CNT networks with random geometrical parameters such as CNT orientation and intersection angles. While some parameters are let to be random in nature, some behavior decisive parameters such as CNT chirality and length scale, cross-link density, angular limits for intersections can be kept under control, which enable to generate different models organized with different parameters. It should be noted here that the approach of considering the CNTs as line segments during the generation process save a lot of computational time for the generation of total network structure. Following the generation of a CNT network in which the CNT units are so close to each other that heating to certain temperatures can yield covalently bonded cross-links, classical molecular dynamics simulations are carried

out to obtain covalently bonded networks. Finally, 2-D or 3-D CNT networks were generated with controllable parameters and could be employed for further mechanical, electrical or thermal studies. Due to the controllability and efficiency on the topological features of CNT networks and simplicity of the generation algorithm, this CNT network generation method may significantly increase the numerical and theoretical investigations on the CNT networks.

The method proposed for the modeling of CNT networks is also applicable to continuum scale analyses in order to overcome the time and length scale limitations of classical molecular dynamics simulations. By the help of line segment representation of the CNTs in the method, the generated network model can be easily converted to a CAD surface or line segment model, which will enable researchers to carry out FE simulations. By this way, availability of the proposed method to be used in classical continuum scale computational studies enlarges the applicability zone of the method. Beside that, the proposed method for the generation of CNT networks, can be utilized or at least can be used as a base idea for the generation of similar network materials which consist of one dimensional structural units that can be idealized as line segments. For example, in the computational modeling of polymeric materials that consist of linear polymer chains, the proposed algorithm may be an ideal inspiration source. Furthermore, following this study, mechanical, thermal or electrical properties of CNT networks can be optimized by changing the topological parameters, and manufacturing techniques can be developed or improved to produce optimized networks.

For the modeling of nanoporous materials, with the spherical cell shape assumption, randomly intersected speherical ensembles are employed to generate nanoporous materials. Within the scope of the developed algorithm, by controlling the several parameters such as maximum and minimum number of spheres intersected to each sphere and maximum overlapping ratio between two intersected spheres, the porosity of the nanoporous systems can be arranged to generate desired nanoporous specimens with desired porosity values. In the meantime, some parameters that can be kept under control help to obtain different ranges of ligament size, which is another direct control on the morphology of nanoporous structures. Central coordinates and radii of spheres existing in the ensemble that is formed by randomly intersection of spheres are employed in atomistic modeling software to remove atoms

encapsulated by the spherical volumes from a crystalline solid block. As a result, by utilizing this technique atomistic models of nanoporous materials can be generated by controlling the key parameters affecting the morphology so the behavior of the structure with the spherical shape assumption of pores.

Applicability of both stochastic algorithms developed for CNT networks and nanoporous materials is shown by demonstrating the specimen samples having the proposed morphological characteristics such as porosity and cross-links for nanoporous and CNT network materials, respectively. For example, for CNT network specimens it is shown that through the network consisting of randomly intersected CNTs, several junction types that are already characterized in literature such as X, Y or T junctions could be generated by the proposed method following the heat welding process realized within molecular dynamics simulations. In the same manner, regarding nanoporous material modeling, it is demonstrated that basic features of a cellular structure such as ligaments, cell walls, pores on the cell walls and junctions could be obtained as a result of realizing the proposed method.

More importantly than showing the validity of proposed algorithms developed for the random atomistic structures, generated numerical specimens for both materials by using the developed techniques are used in molecular dynamics simulations to perform tensile loading experiments. As a result of MD simulations, stress-strain plots have been obtained and by evaluating stress-strain behavior from those plots, different aspects in deformation mechanisms of corresponded materials have been explained. For instance, regarding nanoporous numerical specimens it has been verified that as the porosity of the specimens increases the major mechanical properties including Young's modulus, yield and ultimate tensile strength of the nanoporous materials decreases. Beside this, a notable decrease in softening rate after a specific porosity value has been discovered and this significant softening rate decrease at higher porosity values has been devoted to more homogenous stress distribution due to increased compliance between ligaments and junctions. In order to verify this, von Mises stress distribution of the networks for two different porosities having distinctive softening rates have been compared. While in the specimen with lower porosity the high stress spot areas are cumulated around the upper edge location, for the sample with higher porosity peak stress foci are distributed more evenly. The reason for such a behavior has been explained by the

microstructural compliance issue between ligaments and junction. Thus, it has been concluded that as the porosity decreases stress flow through incompatible junctions and ligaments becomes more difficult to spread out, which in turn results in higher peak stress locations close to load application region. Similarly, stress-strain plots for CNT network specimens have been obtained through MD simulations and shown that as the cross-link density increases, Young's modulus, yield and ultimate tensile strength of CNT networks have been improved. Moreover, deformation mechanisms of CNT networks under tensile loading have been identified by illustrating deformation snapshots taken from the MD simulations while the tensile loading was in progress. In this regard, two main deformation styles have been defined to explain the characteristics of deformation mechanisms. One of these, aligning type of deformation has been referred for the local bending deformations of CNT segments around relatively more rigid regions which are mostly cross-links. The other type of deformation has been named as stretching mode of deformation, in which the CNT segments are subjected to straining in the loading direction without any bending deformation. In conclusion, it has been underlined that the tensile deformation of CNT networks from the global windows proceeds with the combination and interaction of these two deformation styles.

The most important findings from the numerical experiments of the atomistic models which were generated by the presented techniques are the tips that might enable researchers to produce advanced materials with improved properties. For example, regarding nanoporous materials, in this dissertation it has been stated that as the compatibility between junctions and ligaments are increased, load bearing capacity of the porous network can be increased with more uniform lower-level stress distribution comparing to incompatible ligaments and junctions. Therefore, the importance of compliance between structural units within the porous network has been pointed out by this way. In the same way, a similar finding for CNT network materials has been demonstrated by explaining the two different local deformation styles. In this regard, as the period of local bending deformation mode of the CNTs is increased before that the stretching mode turns into dominant mechanism the total elongation of the structure can be increased, which results in improved mechanical performance.

The studies performed in this dissertation can be utilized in the future works for the further investigations on the structure-material relationship of especially randomly organized nanostructured materials. In this respect, first of all, the proposed atomistic model generation techniques for both CNT networks and nanoporous materials can be employed to investigate the effects of other controlled parameters on the mechanical performance. For instance, in this dissertation effects of porosity and cross-link density have been studied for nanoporous and CNT network materials, respectively. In the future studies, other parameters including effect of cell diameters for nanoporous materials and CNT chirality or CNT length scale for CNT network materials can be varied to explore their effects on the mechanical performance. Furthermore, other physical properties such as thermal properties of the materials can also be investigated in terms of the effects of controlled parameters (e.g., porosity, cross-link density) on the desired property. Therefore, the output of this study performed in this dissertation is not only useful or applicable to the investigation of mechanical properties, because of the reason that stochastic atomistic models can be employed in MD simulations for all purposes.

In this dissertation, only 3-D CNT network models have been employed in MD simulations for the investigation of mechanical properties. However, the proposed technique for the generation of random natured CNT networks can also be applicable to generate 2-D network models representing CNT films. As a result, computational experiments on CNT films can be conducted to explore their structure dependent properties and to find tips for manufacturing optimum structures.

Another research opportunity arising from this dissertation is the investigation on the effects of coating of nanoporous materials on the mechanical or thermal behavior of nanoporous materials. The stochastic method developed for the generation of atomistic structure of nanoporous structures can be easily improved to generate coated version of nanoporous structures and then the atomistic models can be used for any purpose of numerical experiments in MD simulations. Similarly, nanoporous models can be filled with another material to explore its effects on the mechanical properties as well as thermal properties.

REFERENCES

- [1] **You saf, A. A. & Ali, S.** (2008). Why nanoscience and technology? What is there for us? *J. Fac. Eng. & Tech.*, 11-20.
- [2] **Rao, C. N. R., Muller, A., & Cheetham, A. K.** (2004). *Chemistry of nanomaterials*. Weinheim: Wiley-VCH.
- [3] **Rao, C. N. R. & Cheetham, A. K.** (2001). Science and technology of nanomaterials. *J. Mater. Chem.*, 11, 2887-2892.
- [4] **Seigel, R. W., Hu, H., & Roco, M.C.** (1999). *Nanostructures science and technology*. Boston: Kluwer Academic Publishers.
- [5] **Roco, M. C., Williams, R. S., & Alivisatos, A. P.** (2000). *Nanotechnology research directions*. Boston: Kluwer Academic Publishers.
- [6] **Manasreh, O.** (2012). *Introduction to nanomaterials and devices*. Hoboken, NJ: John Wiley & Sons.
- [7] **Edelstein, A. S. & Cammarat ra, R. C.** (1996). *Nanomaterials: Synthesis, properties and applications* (2nd ed.). New York, NY: Taylor & Francis.
- [8] **Ajayan, P. M., Schadler, L. S., & Braun, P. V.** (2004). *Nanocomposite science and technology*. Weinheim: Wiley.
- [9] **Gogotsi, Y.** (2006). *Carbon nanomaterials*. Boca Raton, FL: CRC Press.
- [10] **O'Connell, A.J.** (2006). Carbon nanotubes properties and applications. Boca Raton, FL: CRC Press.
- [11] **Pokri pivny, V., Lohmus, R., Hussainova, I., Pokropivny, A., & Vlassov, S.** (2007). *Introduction to nanomaterials and nanotechnology*. Tartu: Tartu University Press.
- [12] **Binns, C.** (2010). *Introduction to nanoscience and nanotechnology*. Hoboken, NJ: John Wiley & Sons.
- [13] **Tanaka, K., Yamabe, T., & Fukui, K.** (1999). *The science and technology of carbon nanotubes* (1st ed.). Oxford: Elsevier Ltd.
- [14] **Hornyak, G. L., Dutta, J., Tibbals, H. H., & Rao, A. K.** (2008). *Introduction to nanoscience*. Boca Raton, FL: CRC Press.
- [15] **Iijima, S., & Ichihashi, T.** (1993). Single-shell carbon nanotubes of 1-nm diameter. *Nature*, 363, 603-605.
- [16] **Bethune, D. S., Klang, C. H., Vries, M. S., Gorman, G., Savoy, R., Vazquez, J., & Beyers, R.** (1993). Cobalt-catalysed growth of carbon nanotubes with single atomic-layer walls. *Nature*, 363, 605-607.
- [17] **Iijima, S.** (1991). Helical microtubules of graphitic carbon. *Nature*, 354, 56-58.

- [18] **Vollath, D.** (2008). *Nanomaterials: an introduction to synthesis, properties and applications*. Weinheim: Wiley-VCH.
- [19] **Guozhong, C.** (2004). *Nanostructures & Nanomaterials: Synthesis, properties & applications*. London: Imperial College Press.
- [20] **Schodek, D. L., Ferreira, P., & Ashby, M. F.** (2009). *Nanomaterials, nanotechnologies and design: An introduction for engineers and architects*. Oxford: Elsevier Ltd.
- [21] **Singh, S. C., Zeng, H. B., Guo, C., & Cai, W.** (2012). *Nanomaterials*. Weinheim: Wiley-VCH.
- [22] **Jackson, M. J.** (2006). *Microfabrication and nanomanufacturing*. Boca Raton, FL: CRC Press.
- [23] **Busnaina, A.** (2006). *Nanomanufacturing handbook*. Boca Raton, FL: CRC Press.
- [24] **Lu, G. Q., & Zhao, X. S.** (2004). Nanoporous materials: An overview. In G. Q Lu & Zhao X.S. (Eds.), *Nanoporous Materials: Science and Engineering* (Vol.4, pp.1-12). London, UK: Imperial College Press.
- [25] **Polarz, S., & Smarsly, B.** (2002). Nanoporous materials. *Journal of Nanoscience and Nanotechnology*, 2 (6), 581-612.
- [26] **Plimpton, S.** (1995). Fast parallel algorithms for short-range molecular-dynamics. *J. Comput. Phys.*, 117, 1-19.
- [27] **Alder, B. J. & Wainwright, T. E.** (1959). Studies in molecular dynamics. i. general method. *J. Chem. Phys.*, 27, 1208-1216.
- [28] **Gibson, J. B., Goland, A. N., Milgram, M., & Vineyard, G. H.** (1960). Dynamics of radiation damage. *Phys. Rev.*, 120, 1229-1253.
- [29] **Rahman, A.** (1964). Correlations in the motion of atoms in liquid argon. *Phys. Rev.*, 136, A405-A411.
- [30] **Weiner, S. J., Kollman, P. A., Case, D. A., Singh, U. C., Ghio, C., Alagona, G., ... Weiner, P.** (1984). A new force-field for molecular mechanical simulation of nucleic acids and proteins. *J. Am. Chem. Soc.*, 106, 765-784.
- [31] **Frenkel, D. & Smit, B.** (2002). *Understanding Molecular Simulation: From Algorithms to Applications* (2nd ed.). San Diego, CA: Academic Press.
- [32] **Tobias, D. J., Martyna, G. J., & Klein, M. L.** (1993). Molecular dynamics simulations of a protein in the canonical ensemble. *J. Phys. Chem.*, 97, 12959-12966.
- [33] **Maitland, G. C., Rigby, M., Smith, E. B., & Wakeham, W. A.** (1981). *Intermolecular forces:their origin and determination*. Oxford: Clarendon Press.
- [34] **Stone, A. J.** (1996). *The theory of intermolecular forces*. Oxford: Clarendon Press.
- [35] **Evans, D. J. & Morriss, G. P.** (1990). *Statistical mechanics of nonequilibrium liquids*. London: Academic Press.

- [36] **Andersen, H. C.** (1980). Molecular dynamics simulations at constant pressure and/or temperature. *J. Chem. Phys.*, *72*, 2384-2393.
- [37] **Deleeuw, S. W., Perram, J. W., & Petersen, H.G.** (1990). Hamilton equations for constrained dynamics systems. *J. Stat. Phys.*, *61*, 1203-1222.
- [38] **Verlet, L.** (1967). Computer experiments on classical fluids. i. thermodynamical properties of Lennard-Jones molecules. *Phys. Rev.*, *159*, 98-103.
- [39] **Daw, M.S. & Baskes, M.I.** (1984). Embedded-atom method: Derivation and application to impurities, surfaces, and other defects in metals. *Phys. Rev. B*, *29*, 6443-6453.
- [40] **Stuart, S. J., Tutein, A. B., & Harrison, J. A.** (2000). A reactive potential for hydrocarbons with intermolecular interactions. *J. Chem. Phys.*, *112*, 6472-6486.
- [41] **Brenner, D. W., Shenderova, O. A., Harrison, J. A., Stuart, S. J., Ni, B., & Sinnott, S. B.** (2002). A second-generation reactive empirical bond order (REBO) potential energy expression for hydrocarbons. *Phys. Rev. B*, *14*, 783-802.
- [42] **Gibson, L. J. & Ashby, M. F.** (1997). *Cellular Solids: Structures and Properties* (2nd ed.). Cambridge, England: Cambridge University Press.
- [43] **Bonroy, K., Friedt, J. -M, Frederix, F., Laureyn, W., Langerock, S., Campitelli, A., ...Declerck, P.** (2004). Realization and characterization of porous gold for increased protein coverage on acoustic sensors. *Anal. Chem.*, *76*, 4299.
- [44] **Weissmüller, J., Viswanath, R. N., Kramer, D., Zimmer, P., Wuerschum, R., & Gleiter, H.** (2003). Charge-induced reversible strain in a metal. *Science*, *300*, 312.
- [45] **Hodge, A. M., Biener, J., Hayes, J. R., Bythrow, P. M., Volkert, C. A., & Hamza, A. V.** (2007). Scaling equation for yield strength of nanoporous open-cell foams. *Acta Mater.*, *55*, 1343-1349.
- [46] **Sun, X. Y., Xu, G. K., Li, X., Feng, X. Q., & Gao, H.** (2013). Mechanical properties and scaling laws of nanoporous gold. *J. Appl. Phys.*, *113*, 023505-9.
- [47] **Farkas, D., Caro, A., Bringa, E., Crowson, D.** (2013). Mechanical response of nanoporous gold. *Acta Materialia*, *61*, 3249-3256.
- [48] **Sun, Y., Ye, J., Shan, Z., Minor, A.M., Balk, T.J.** (2007). The Mechanical Behavior of Nanoporous Gold Thin Films. *JOM*, *59*, 54-58.
- [49] **Zhu, H. X., Knott, J. F., & Mills, N. J.** (1997). Analysis of the elastic properties of open-cell foams with tetrakaidecahedral cells. *Journal of the Mechanics and Physics of Solids*, *45*, 319-343.
- [50] **Warren, W. E., & Kraynik, A. M.** (1988). Linear elastic properties of open-cell foams. *Journal of Applied Mechanics*, *55*, 341-346.

- [51] **Duria, D. J.** (1997). Bubble-scale model of foam mechanics: Melting, nonlinear behavior, and avalanches. *Physical Review E*, 55, 1739-1751.
- [52] **Xia, R., Xu, C. X., Wu, W. W., Li, X., Feng, X. Q., & Ding, Y.** (2009). Microtensile tests of mechanical properties of nanoporous Au thin films. *Journal of Materials Science*, 44, 4728–4733.
- [53] **Li, R. & Sieradzki, K.** (1992). Ductile-brittle transition in random porous Au. *Phys. Rev. Lett.*, 68, 1168-1178.
- [54] **Erlebacher, J., Aziz, M. J., Karma, A., Dimitrov, N., & Sieradzki, K.** (2001). Evolution of nanoporosity in dealloying. *Nature*, 410, 450-453.
- [55] **Kramer, D., Viswanath, R. N., & Weissmüller, J.** (2004). Surface-stress induced macroscopic bending of nanoporous gold cantilevers. *Nano Letters*, 4, 793.
- [56] **Ganguly, P. & Ulm, F. -J.** (2007). Analysis of deformation coupled surface remodeling in porous biomaterials. *J. Mater. Sci.*, 42, 8873.
- [57] **Kaneko K.** (1994). Determination of pore size and pore size distribution: 1. Adsorbents and catalysis. *Journal of Membrane Science*, 96, 59-89.
- [58] **Hakamada, M. & Mabuchi, M.** (2007). Mechanical strength of nanoporous gold fabricated by dealloying. *Scr. Mater.*, 56, 1003-1009.
- [59] **Zhang, W. X. & Wang, T. J.** (2007). Effect of surface energy on the yield strength of nanoporous materials. *Appl. Phys. Lett.*, 90, 063104.
- [60] **Mathur, A. & Erlebacher, J.** (2007). Size dependence of effective Young's modulus of nanoporous gold. *Appl. Phys. Lett.*, 90, 061910.
- [61] **Biener, J., Hodge, A. M., & Hamza, A. V.** (2005). Microscopic failure behavior of nanoporous gold. *Appl. Phys. Lett.*, 87, 121908.
- [62] **Kirca, M., Gul, A., Ekinci, E., Yardim, F., & Mugan, A.** (2007). Computational modeling of micro-cellular carbon foams. *Finite Elem. Anal. Des.*, 44, 45-52.
- [63] **Li, R., Sieradzki, K.** (1992). Ductile-Brittle Transition in Random Porous Au. *Phys. Rev. Lett.*, 68, 1168-1171.
- [64] **Khang, B., Batrouni, G. G., Redner, S., Arcangelis, L., & Hermann, H. J.** (1988). Electrical Breakdown in a Fuse Network with Random, Continuously Distributed Breaking Strengths. *Phys. Rev. B.*, 37, 7625-7637.
- [65] **Volkert CA, Lilleodden ET, Kramer D, Weissmuller J.** (2006). Approaching the Theoretical Strength in Nanoporous Au. *Appl Phys Lett* 89, p.061920.
- [66] **Volkert, C.A. & Lilleodden, E.T.** (2006). Size Effects in the Deformation of Sub- Micron Au Columns, *Philos. Mag.* 86,pp. 5567-5579.
- [67] **Biener, J., Hodge, A. M., Hayes, J. R., Volkert, C. A., Zepeda-Ruiz, L.A., Hamza, A. V., & Abraham, F. F.** (2006). Size Effects on the Mechanical Behavior of Nanoporous Au. *Nano Letters*, 6, 2379-2382.

- [68] **Hodge, A. M., Doucette, R. T., Biener, M. M., Biener, J., Cervantes, O. & Hamza, A. V.** (2009). Ag effects on the elastic modulus values of nanoporous Au foams. *Journal of Materials Research*, 24, 1600-1606.
- [69] **Ko, W. L.** (1965). Deformation of foamed elastomers. *Journal of Cellular Plastics*, 1, 45-50.
- [70] **Dou, R. & Derby, B.** (2011). Deformation mechanisms in gold nanowires and nanoporous gold. *Philosophical Magazine*, 91(7), 1070-1083.
- [71] **Biener, J., Hodge, A. M. & Hamza, A. V.** (2005). Microscopic Failure Behavior of Nanoporous Gold. *Appl. Phys. Lett.*, 87, 121908.
- [72] **Biener, J., Hamza, A. V. & Hodge, A. M.** (2008). Deformation Behavior of Nanoporous Metals. In F. Yang & J. C. M. Li (Eds.), *Micro and nano mechanical testing of materials and devices* (pp.121-138). New York, NY: Springer.
- [73] **Bonroy, K., Friedt, J. -M., Frederix, F., Laureyn, W., Langerock, S., Campitelli, A., ...Declerck, P.** (2004). Realization and characterization of porous gold for increased protein coverage on acoustic sensors. *Anal. Chem.*, 76, 4299-4306.
- [74] **Ganguly, P., & Ulm, F- J.** (2007). Analysis of deformation coupled surface remodeling in porous biomaterials. *Mater. Sci.*, 42, 8873-8884.
- [75] **Allen, M. P. & Tildesley, D. J.** (1987). *Computer simulation of liquids*. Clarendon: Oxford University Press.
- [76] **Andrews, E. W., Gioux, G., Onck, P., & Gibson, L. J.** (2001). Size effects in ductile cellular solids. Part II: experimental results. *International Journal of Mechanical Sciences*, 43(3), 701-713.
- [77] **Chen, L., Ozisik, R., & Schadler, L. S.** (2010). The influence of carbon nanotube aspect ratio on the foam morphology of MWNT/PMMA nanocomposite foams. *Polymer*, 51, 2368-2375.
- [78] **Xu, G. & Argon, A. S.** (2000). Homogeneous nucleation of dislocation loops under stress in perfect crystal. *Philosophical Magazine Letters*, 80, 605-611.
- [79] **Bauccio, M.** (1993). *ASM Metals Reference Book* (3rd ed.). Materials Park, Ohio: ASM Intl.
- [80] **Fischer-Cripps, A.C.** (2009). *The IBIS Handbook of Nanoindentation*. Forestville, Australia: Fischer-Cripps Laboratories.
- [81] **Ding Y., Kim, Y. -J., & Erlebacher J.** (2004). Nanoporous Gold Leaf: ‘Ancient Technology’. *Adv. Mater.*, 16, 1897-1900.
- [82] **Geer, J. R. & Nix, W. D.** (2005). Size dependence of mechanical properties of gold at the sub-micron scale. *Appl. Phys. A*, 80 (8), 1625-1629.
- [83] **Xiang, Y., Chen, X., Tsui, T. Y., Jang, J. -I. & Vlassak, J. J.** (2006). Mechanical properties of porous and fully dense low- κ dielectric thin films measured by means of nanoindentation and the plane-strain bulge test technique. *Journal of Materials Research*, 21, 386-395.

- [84] **Dou, R. & Derby B.** (2010). Strain gradients and the strength of nanoporous gold. *J. Mater. Res.*, *25*, 746-753.
- [85] **Qian, L. H., Chen, M. W.** (2007). Ultrafine nanoporous gold by low-temperature dealloying and kinetics of nanopore formation. *Appl. Phys. Lett.*, *91*, 083105.
- [86] **Uchic, M. D., Dimiduk, D. M., Florando, J. N., & Nix, W. D.** (2004). Sample dimensions influence strength and crystal plasticity. *Science*, *305*, 986-989.
- [87] **Rösler, J., Nähth, O., Jäger, S., Schmitz, F., & Mukherji, D.** (2005). Fabrication of nanoporous Ni-based superalloy membranes. *Acta Mater.*, *53*, 1397-1406.
- [88] **Jin, H. -J., Kurmanaeva, L., Schmauch, J., Rösner, H., Ivanisenko, Y., Weissmüller, J.** (2009). Deforming nanoporous metal: Role of lattice coherency. *Acta Mater.*, *57*(9), 2665-2672.
- [89] **Hayes, J. R, Hodge, A. M., Biener, J., Hamza, A. V., & Sieradzki, K.** (2006). Monolithic Nanoporous Copper by Dealloying Mn-Cu. *J. Mater. Res.*, *21*, 2611-2616.
- [90] **Wu, B., Heidelberg, A., & Boland, J. J.** (2005). Mechanical properties of ultrahigh-strength gold nanowires. *Nature Materials*, *4*, 525 – 529.
- [91] **Horstemeyer, M. F., Baskes, M. I., & Plimpton, S. J.** (2001). Length scale and time scale effects on the plastic flow of fcc metals. *Acta Mater.*, *49*, 4363-4374.
- [92] **Erlebacher, J., Aziz, M. J., Karma, A., Dimitrov, N., & Sieradzki. K.** (2001). Evolution of nanoporosity in dealloying. *Nature*, *410*, 450-453.
- [93] **Lee, D., Wei, X. D., Zhao, M. H., Chen, X., Jun, S. C., Hone, J., Kysar, J. W.** (2007). Plastic deformation in nanoscale gold single crystals and open-celled nanoporous gold. *Modelling Simul. Mater. Sci. Eng.*, *15*, 181-192.
- [94] **Chu, T. C., Ranson, W. F., & Sutton, M. A.** (1985). Applications of digital image correlation techniques to experimental mechanics. *Exp. Mech.*, *25*, 232–44.
- [95] **Zhou, M.** (2003). A new look at the atomic level virial stress: on continuum-molecular system equivalence. In Welland, M., (Ed.), *Proceedings of the Royal Society A Mathematical Physical and Engineering Sciences*. (pp. 2347-2392). United Kingdom: The Royal Society.
- [96] **Liu, Z., & Searso, P. -C.** (2006). Single Nanoporous Gold Nanowire Sensors. *J. Phys. Chem. B*, *110*, 4318-4322.
- [97] **Logar, Z. & Kaučič, V.** (2006). Nanoporous Materials: From Catalysis and Hydrogen Storage to Wastewater Treatment. *Acta Chim. Slov.*, *53*, 117–135.
- [98] **Newman, R. C., Corcoran, S. G, Erlebacher, J., Aziz, M. J., & Sieradzki, K.** (1999). Alloy Corrosion. *MRS Bulletin*, *74*(7), 24-28.

- [99] **Parida, .S., Kramer, D., Volkert, C. A., Rosner, H., Erlebacher, J., & Weissmuller, J.** (2006). Volume Change During the Formation of Nanoporous Gold by Dealloying. *Phys. Rev. Lett.*, *97*, 035504.
- [100] **Sieradzki, K. & Newman, R.** (1985). Brittle behavior of ductile metals during stress-corrosion cracking. *Phil. Mag. A*, *51*, 95-132.
- [101] **Koh, S. J. A. & Lee, H. P.** (2006). Molecular dynamics simulation of size and strain rate dependent mechanical response of FCC metallic nanowires. *Nanotechnology*, *17*(14), 3451-3467.
- [102] **Weissmüller, J., Viswanath, R. N., Kramer, D., Zimmer, P., Wuereschum, R., & Gleiter, H.** (2003). Charge induced reversible strain in a metal. *Science*, *300*, 312-315.
- [103] **Kramer, D., Viswanath, R. N., & Weissmüller, J.** (2004). Surface-Stress induced macroscopic bending of nanoporous gold cantilevers. *Nano Lett.*, *4*, 793-796.
- [104] **Van Petegem, S., Brandstetter, S., Hodge, A. M., El-Dasher, B. S., Biener, J., Schmitt, B., Borca, C., Van Swygenhoven, H.** (2009). On the microstructure of nanoporous gold: an X-ray diffraction study. *Nano Lett.*, *9*, 1158–1163.
- [105] **Stafford, C. M., Harrison, C., Beers, K. L., Karim, A., Amis, E. J., Van Landingham, M. R., ...Simonyi, E. E.** (2004). A buckling-based metrology for measuring the elastic moduli of polymeric thin films. *Nature Materials*, *3*, 545-550.
- [106] **Dai, H. J.** (2002). Carbon nanotubes:synthesis, integration, and properties. *Accounts of Chemical Research*, *35*, 1035-1044.
- [107] **Dai, H. J.** (2001). Nanotube growth and characterization. *Carbon Nanotubes*, *80*, 29-53.
- [108] **Treacy, M. M. J., Ebbesen, T. W., & Gibson, J. M.** (1996). Exceptionally high Young's modulus observed for individual carbon nanotubes. *Nature*, *381*, 678-680.
- [109] **Wong, E. W., Sheehan, P. E., & Lieber, C. M.** (1997). Nanobeam mechanics: elasticity, strength, and toughness of nanorods and nanotubes. *Nature*, *381*, 678-680.
- [110] **Krishnan, A., Dujardin, E., Ebbesen, T. W., Yianilos, P. N., & Treacy, M. M. J.** (1998). Young's modulus of single-walled nanotubes. *Phys. Rev. B*, *58*, 14013-14019.
- [111] **Salvetat, J. P., Kulik, A.J., Bonard, J. M., Briggs, G. A. D., Stockli, T., & Metenier, K.** (1999). Elastic modulus of ordered and disordered multiwalled carbon nanotubes. *Adv. Mater.*, *11*(2), 161-165.
- [112] **Tombler, T. W., Zhou, C. W., Alexaeyev, I., Kong, J., Dai, H. J., & Liu, I.** (2000). Reversible electromechanical characteristics of carbon nanotubes under local-probe manipulation. *Nature*, *405*, 769-772.

- [113] **Cooper, C. A. & Young, R. J.** (2000). Investigation into the deformation of carbon nanotubes and their composites through the use of Raman spectroscopy. *Optical Devices and Diagnostics in Materials Science*, 172, 1205-1217.
- [114] **Yu, M. F., Files, B. S., Arepalli, S., & Ruoff, R. S.** (2000). Tensile loading of ropes of single wall carbon nanotubes and their mechanical properties. *Phys. Rev. Lett.*, 84, 5552-5555.
- [115] **Lourie, O. & Wagner, H. D.** (1998). Transmission electron microscopy observations of fracture of single-wall carbon nanotubes under axial tension. *Applied Physics Letters*, 73, 3527-3536.
- [116] **Yakobson, B. I., Brabec, C. J., & Bernholc, J.** (1996). Nanomechanics of Carbon Tubes: Instabilities beyond Linear Response. *Physical Review Letters*, 76, 2511-2514.
- [117] **Halicioglu, T.** (1998). Stress calculations for carbon nanotubes. *Thin Solid Films*, 312, 11-14.
- [118] **Zhou, G., Duan, W., & Gu, B.** (2001). First-principles study on morphology and mechanical properties of single-walled carbon nanotube. *Chem. Phys. Lett.*, 333, 344-349.
- [119] **Robertson, D. H., Brenner, D. W., & Mintmire, J. W.** (1992). Energetics of nanoscale graphitic tubules. *Physics Review Letters B*, 45, 592-601.
- [120] **Cornwell, C. F. & Wille, L. T.** (1997). Elastic properties of single-walled carbon nanotubes in compression. *Solid State Communications*, 101, 555-558.
- [121] **Lu, J. P.** (1997). Elastic properties of carbon nanotubes and nanoropes. *Phys. Rev. Lett.*, 79, 1230-1297.
- [122] **Herhandez, E., Goze, C., Bernier, P., & Rubio, A.** (1998). Elastic properties of C and $B_xC_yN_z$ composite nanotubes. *Phys. Rev. Lett.*, 80, 4502-4505.
- [123] **Yao, N. & Lordi, V.** (1998). Young's modulus of single-walled carbon nanotubes. *J. Appl. Phys.*, 84, 1939-1944.
- [124] **Ozaki, T., Iwasa, Y., & Mitani, T.** (2000). Stiffness of single-walled carbon nanotubes under large strain. *Phys. Rev. Lett.*, 84, 1712-1715.
- [125] **Lier, G. V., Alsenoy, C. V., Doran, V. V., & Geerlings, P.** (2000). Ab initio study of the elastic properties of single-walled carbon nanotubes and grapheme. *Chem. Phys. Lett.*, 326, 181-185.
- [126] **Belytschko, T., Xiao, S. P., Schats, G. C., Ruoff, R. S.** (2002). Atomistic simulations of nanotube fracture. *Phys. Rev. B*, 65, 2354301-2354308.
- [127] **Huang, J. Y., Chen, S., Wang, Z. Q., Kempa, K., Wang, Y. M., Jo, S. H., Chen, G., Dresselhauss, M. S., & Ren, Z. F.** (2006). Superplastic carbon nanotubes. *Nature*, 439, 281.
- [128] **Iijima, S., Brabec, C., Maiti, A. & Bernholc, J.** (1996). Structural flexibility of carbon nanotubes. *J. Chem. Phys.*, 104, 2089-2092.

- [129] **Arias, I., & Arroyo, M.** (2008). Size-dependent nonlinear elastic scaling of multiwalled carbon nanotubes. *Physical Review Letters*, 100, 085503.
- [130] **Wang, M., & Wang, J., Chen, Q., & Peng, L. M.** (2005). Fabrication and electrical and mechanical properties of carbon nanotube interconnections. *Adv. Funct. Mater.*, 15, 1825-1831.
- [131] **Baughman, R. H., Zakhidov, A. A., & de Heer, W. A.** (2002). Carbon nanotubes – The route towards applications. *Science*, 297, 787-792.
- [132] **Hu, J., Odom, T. W., & Lieber, C. M.** (1999). Chemistry and physics in one-dimension: synthesis and properties of nanowires and nanotubes. *Acc. Chem. Res.*, 32, 435-445.
- [133] **Leroy, C. M., Carn, F., Trinquecoste, M., Backov, R., & Delhaes, P.** (2007). Multiwalled-carbon-nanotube-based carbon foams. *Carbon*, 45, 2317-2320.
- [134] **Worsley, M. A., Kucheyev, S. O., Satcher, J. H., Hamza, A. V., & Baumann, T. F.** (2009). Mechanically robust and electrically conductive carbon nanotube foams. *App. Phy. Let.*, 94 (7), 073115.
- [135] **Nabeta, M., & Sano, M.** (2005). Nanotube foam prepared by gelatin gel as a template. *Langmuir*, 21, 1706-1708.
- [136] **Kaur, S., Ajayan, P. M., & Kane, R.S.** (2006). Design and characterization of three-dimensional carbon nanotube foams. *J. Phys. Chem. B.*, 110, 21377-21380.
- [137] **Bryning, M. B., Milkie, D. E., Islam, M. F., Hough, L. A., Kikkawa, J. M., & Yodh, A. G.** (2007). Carbon nanotube aerogels. *Adv. Mater.*, 19, 661-664.
- [138] **Lee, H. S., Yun, C. H., Kim, S. K., Choi, J. H., Lee, C. J., Jin, H. J., ... Park, M.** (2009). Percolation of two-dimensional multiwall carbon nanotube networks. *Appl. Phys. Lett.*, 95, 134104.
- [139] **Meng, F. Y., Shi, S. Q., Xu, D. S., & Yang, R.** (2006). Size effect of X-shaped carbon nanotube junctions. *Carbon*, 44, 1263-1266.
- [140] **Snow, E. S., Novak, J. P., Campbell, P.M., & Park, D.** (2003). Random networks of carbon nanotubes as an electronic material. *Appl. Phys. Lett.*, 82, 2145-2147.
- [141] **Frankland, S. J. V., Harik, V. M., Odegard, G. M., Brenner, D. W., & Gates, T. S.** (2003). The stress-strain behavior of polymer–nanotube composites from molecular dynamics simulation. *Compos. Sci. Technol.*, 63, 1655–1661.
- [142] **Thostenson, E. T., & Chou, T. W.** (2006). Carbon nanotube networks: sensing of distributed strain and damage for life prediction and self healing. *Adv. Mater.*, 18, 2837-2841.
- [143] **Li, Y., Qiu, X., Yin, Y., Yang, F., & Fan, Q.** (2009). The specific heat of carbon nanotube networks and their potential applications. *J. Phys. D: Appl. Phys.*, 42, 155405.
- [144] **Dimaki, M., Bøggild, P. & Svendsen, W.** (2007). Temperature response of carbon nanotube networks. *J. Phys.: Conf. Ser.*, 61, 247-251.

- [145] **Slobodian, P., Riha, P., Lengalova, A., & Saha, P.** (2011). Compressive stress-electrical conductivity characteristics of multiwall carbon nanotube networks. *J. Mater. Sci.* 46, 3186-3190.
- [146] **Coluci, V. R., Dantas, S. O., Jorio, A., & Galvao, D. S.** (2007). Mechanical properties of carbon nanotube networks by molecular mechanics and impact molecular dynamics calculations. *Phys. Rev. B*, 75, 075417.
- [147] **Li, Y., Qiu, X., Yang, F., Yin, Y., & Fan, Q.** (2009). Stretching-dominated deformation mechanism in a super square carbon nanotube network. *Carbon*, 47, 812-819.
- [148] **Hall, L. J., Coluci, V. R., Galvao, D. S., Kozlov, M. E., Zhang, M., Dantas, S. O., & Baughman, R. H.** (2008). Sign change of Poisson's ratio for carbon nanotube sheets. *Science*, 320, 504-507.
- [149] **Jin, Y., & Yuan, F.G.** (2003). Simulation of elastic properties of single-walled carbon nanotubes. *Compos. Sci. Technol.*, 63, 1507-1515.
- [150] **Lan, M. & Waisman, H.** (2012). Mechanics of SWNT aggregates studied by incremental constrained minimization. *J. Nanomech. Micromech.*, 2, 15-22.
- [151] **Yang, Y., Gupta, M. C., Dudley, K. L., & Lawrence, R.W.** (2005). Novel carbon nanotube-polystyrene foam composites for electromagnetic interference shielding. *Nano Letters*, 5, 2131-2134.
- [152] **Li, C., & Chou, T. W.** (2003). A structural mechanics approach for the analysis of carbon nanotubes. *Int. J. Solids Struct.*, 40, 2487-2499.
- [153] **Berber, S., Kwon, Y. K., & Tomànek, D.** (2000). Unusually high thermal conductivity of carbon nanotubes. *Phys. Rev. Lett.*, 84, 4613–4616.
- [154] **Feng, Y. M., Lourie, O., Dyer, M. J., Moloni, K., Kelly, T. F., & Ruoff, R.S.** (2000). Strength and breaking mechanism of multiwalled carbon nanotubes under tensile load. *Science*, 287, 637-640.
- [155] **Lin, Y., Cai, W., Shao, X.** (2006). Fullerenes connected nanotubes: An approach to build multidimensional carbon nanocomposites. *Chemical Physics*, 331, 85-91.
- [156] **Reddy, A. L. M., & Ramaprabhu, S.** (2007). Design and fabrication of carbon nanotube-based microfuel cell and fuel cell stack coupled with hydrogen storage device. *Int. J. Hydrogen Energ.*, 32, 4272-4278.
- [157] **Snow, E. S., Novak, J. P., Lay, M. D., Houser, E. H., Perkins, F. K., & Campbell, P. M.** (2004). Carbon nanotube networks: Nanomaterial for macroelectronic applications. *J. Vac. Sci. Technol. B*, 22, 1990-1994.
- [158] **Jaber, A. L., Hahm, M. G., Kim, T. H., Somu, S., Busnaina, A., & Jung, Y. J.** (2009). Large scale highly organized single-walled carbon nanotube networks for electrical devices. *Appl. Phys. A-Mater.*, 96, 373-377.
- [159] **Tu, Y., Lin, Y., Yantasee, W., & Ren, Z.** (2004). Carbon nanotubes based nanoelectrode arrays: fabrication, evaluation, and application in voltammetric analysis. *Electroanal.*, 17, 79-84.

- [160] **Novak, P. J., Lay, M. D., Perkins, F. K., & Snow, E.S.** (2004). Macroelectronic applications of carbon nanotube networks. *Solid State Electron.*, 48, 1753-1756.
- [161] **Tai, N. H., Yeh, M. K., & Liu, J. H.** (2004). Enhancement of the mechanical properties of carbon nanotube/phenolic composites using a carbon nanotube network as the reinforcement. *Carbon*, 42, 2735-2777.
- [162] **Li, C., & Chou, T. W.** (2008). Modeling of damage sensing in fiber composites using carbon nanotube networks. *Compos. Sci. Technol.*, 68, 3373-3379.
- [163] **Zavodchikova, M. Y., Nasibulin, A. G., Kulmala, T., Grigoras, K., Anisimov, A. S., Franssila, S., ...Kauppinen, E. I.** (2009). Novel carbon nanotube network deposition technique for electronic device fabrication. *Phys. Stat. Sol.*, 245, 2272-2275.
- [164] **Cassell, A. M., McCool, G. C., Tee, N. H., Koehne, J. E., Chen, B., Li, J., ...Meyyappan, M.** (2003). Carbon nanotube networks by chemical vapor deposition. *Appl. Phys. Lett.*, 82, 817-819.
- [165] **Jang, E. Y., Kang, T. J., Im, H. W., Kim, D. W. & Kim, Y. H.** (2008). Single-walled carbon-nanotube networks on large area glass substrate by the dip-coating method. *Small*, 12, 2255-2261.
- [166] **Zavodchikova, M. Y., Kulmala, T., Nasibulin, A. G., Ermolov, V., Franssila, S., Grigoras, K., & Kauppinen, E. I.** (2009). Carbon nanotube thin film transistors based on aerosol methods. *Nanotechnology*, 20, 085201.
- [167] **Rahatekar, S. S., Koziol, K. K., Kline, S. R., Hobbie, E. K., Gilman, J. W., & Windle, A. H.** (2009). Length-dependent mechanics of carbon-nanotube networks. *Adv. Mater.*, 21, 874-878.
- [168] **Gorrasi, G., Lieto, R. D., Patimo, G., Pasquale, S. D., Sorrentino, A.** (2011). Structure-property relationships on uniaxially oriented carbon nanotube/polyethylene composites. *Polymer*, 52, 1124-1132.
- [169] **Kis, A. & Zettl, A.** (2008). Nanomechanics of carbon nanotubes. *Phil. Trans. R. Soc. A*, 366, 1591-1611.
- [170] **Chakrapani, N., Wei, B., Carrillo, A., Ajayan, P. M., Kane, R. S.** (2004). Capillarity-driven assembly of two-dimensional cellular carbon nanotube foams. *Natl. Acad. Sci.*, 101, 4009-4012.
- [171] **Shima, H. & Sato, M.** (2008). Multiple radial corrugations in multiwall carbon nanotubes under pressure. *Nanotechnology*, 19, 495705.
- [172] **Sato, M. & Shima, H.** (2009). Buckling Characteristics of Multiwalled Carbon Nanotubes under External Pressure. *Interactions and Multiscale Mechanics*, 2(2), 209-222.

APPENDICES

APPENDIX A: Workflows for the generation of randomly intersected sphere and CNT network

APPENDIX A: Workflows for the generation of randomly intersected sphere and CNT network

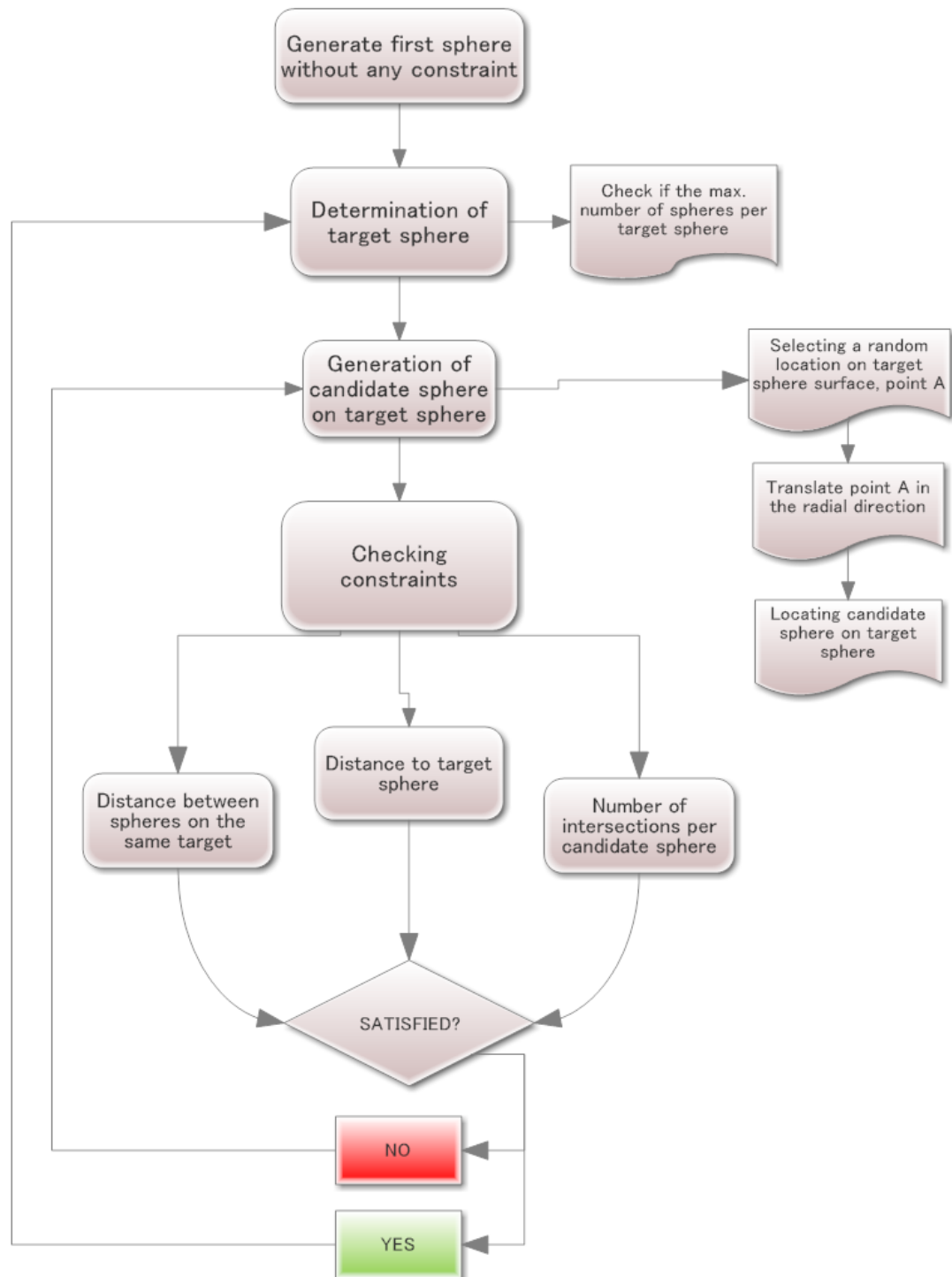


Figure A.1 : Workflow for generation of randomly intersected sphere network.

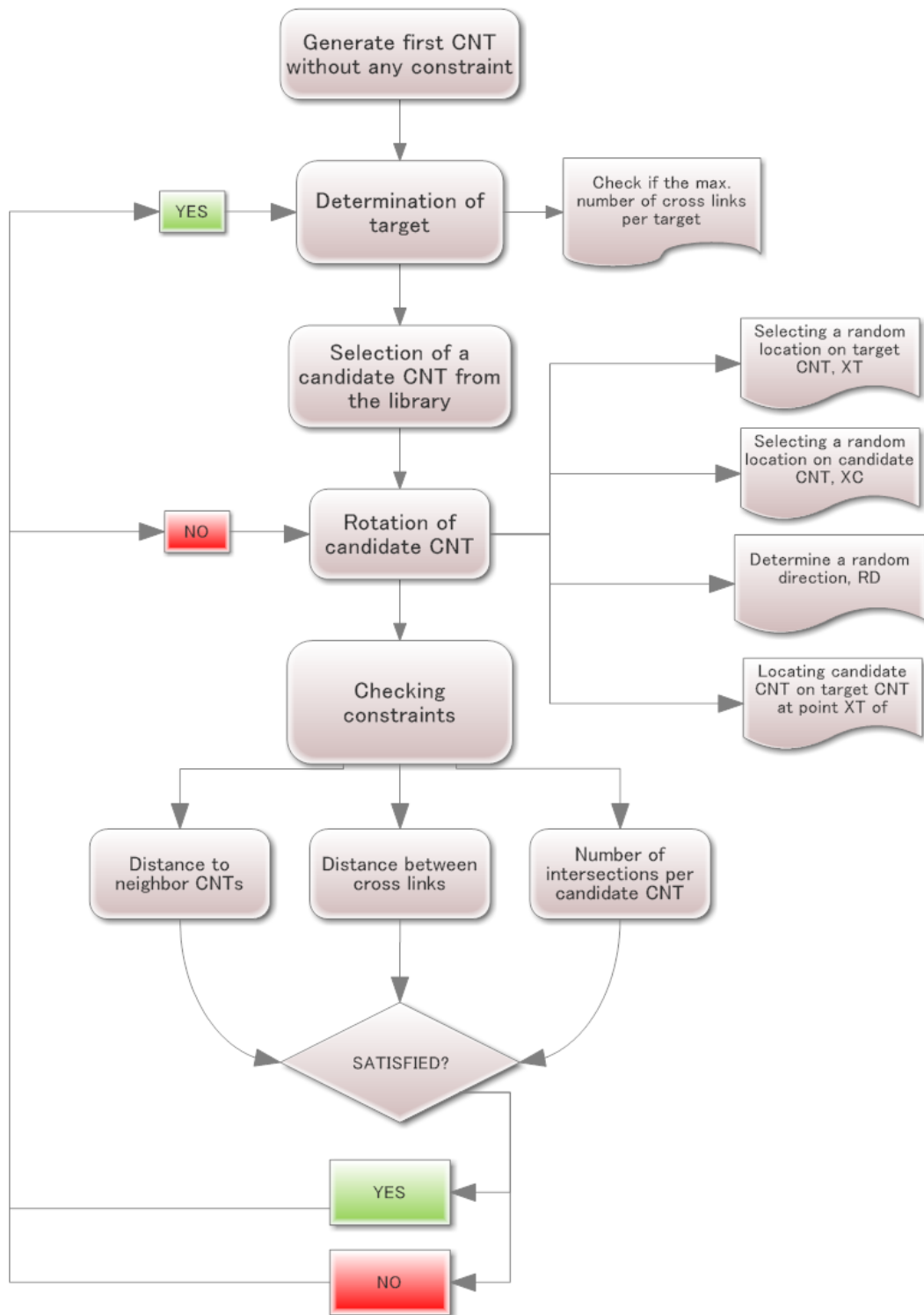


Figure A.2 : Workflow for the generation of CNT network.

CURRICULUM VITAE

Name Surname: Mesut Kırca

Place and Date of Birth: Amasya/ 13.02.1981

E-Mail: kircam@itu.edu.tr

B.Sc.: Aeronautical Engineering, ITU

M.Sc. : Mechanical Engineering, ITU

Professional Experience and Rewards:

2012 (June)- ... : Design Engineer, General Electric-Aviation

2010 (June)- 2012 (May): F&DT Engineer, Korean Aerospace Industry (KAI), Airbus A350XWB Project, ATARD Engineering Korea

2009 (January) to 2010 (June): Research Assistant, University of Pittsburgh, USA

2008 (March) to 2009 (January): VESTEL Defense Industry, Structural Design and Analysis Engineer

2007 (April) to 2008 (March): FORD OTOSAN Automotive Company, Powertrain Engineering, R&D Engineer

2004 (May) to 2005 (March): ITU LCH Helicopter Project (ROTAM), R&D Engineer

List of Publications and Patents:

Journal

- Baykasoglu, C., **Kırca, M.** and Mugan, A. (2013). Nonlinear failure analysis of carbon nanotubes by using molecular-mechanic based models. *Composite Part B: Engineering*, 50, 150-157.
- Y. Fu, **M. Kırca**, and A. C. To (2011). On determining the thermal state of individual atoms in molecular dynamics simulations of nonequilibrium processes in solids. *Chemical Physics Letters*, 506, 290-297.
- Yang, X., To, A. C., and **Kırca, M.** (2011). Thermal conductivity of periodic array of intermolecular junctions of silicon nanowires. *Physica E*.
- Datta, A., **Kırca, M.**, Fu, Y., and To, A. C. (2011). Surface structure and properties of functionalized nanodiamonds: a first-principles study. *Nanotechnology*, 22, 065706.
- **Kırca, M.**, Gul, A., Yardım, M. F., Ekinci, E., Mugan, A. (2007). Computational Modeling of Micro-Cellular Carbon Foams. *Finite Elements in Analysis and Design* , 44, 45-52.

Conference

- **Kirca, M.**, He, W., To, A.C. Validation of the Thermomechanical Atomistic-to-Continuum Model. *Joint ASCE-ASME-SES Conference on Mechanics and Materials*, June 2009.
- **Kirca, M.**, Ozansoy, O. Finite Element Modeling of Microcellular Carbon Foam. *5th International Conference on Advanced Engineering Design*, 2006, Prague, Czech Republic.
- Dogan, V., **Kirca, M.** Dynamic analysis of a helicopter rotor by Dymore Program. *The 7th International Conference on Vibration Problems (ICOVP-2005)*, Isik University.
- A. Giri, J. Tao, **M. Kirca**, and A. C. To. Mechanics of nanoporous metals. In *Handbook of Micromechanics and Nanomechanics*, edited by S. Li and X. L. Gao (Pan Stanford, Singapore), 2013.

PUBLICATIONS/PRESENTATIONS ON THE THESIS

Journal

- **M. Kirca**, Mugan A. and A.C. To, "Mechanical behavior of coated metallic nanofoams", *Computer Methods in Applied Mechanics and Engineering*, 2013 (To be submitted).
- **M. Kirca**, X. Yang, and A. C. To, "A stochastic algorithm for modeling heat welded random carbon nanotube network," *Computer Methods in Applied Mechanics and Engineering*, 259, 1-9, 2013
- B. A. Stormer, N. M. Piper, X. Yang, J. Tao, Y. Fu, **M. Kirca**, and A. C. To (2012). "Mechanical properties of SWNT X-junctions through molecular dynamics simulation," *International Journal of Smart and Nano Materials*.
- A. C. To, J. Tao, **M. Kirca**, and L. Schalk (2011), "Ligament and joint sizes govern softening in nanoporous aluminum," *Applied Physics Letters*, 98, 051903.
- A. Giri; J. Tao; L. Wang; **M. Kirca**; A. To, Compressive behavior and deformation mechanism of nanoporous open-cell foam with ultrathin ligaments, *Journal of Nanomechanics and Micromechanics* (Accepted).

Conference

- Icer E., Celebi A.T., **Kirca M.**, Baykasoglu C. and Mugan A., "Comparison of the strain behavior of nanoporous Cu", NanoTR-9 Erzurum, 24-28 June 2013.
- Celebi A.T., Icer E., **Kirca M.**, Baykasoglu C. and Mugan A., "Analysis of Junctions in Carbon Nanotube Networks", NanoTR-9 Erzurum, 24-28 June 2013.
- **Kirca M.**, Islam M. F., To A.C, "Mechanical Properties of Ultra-Lightweight Fused Carbon Nanotube Structures", 10th US National Congress on Computational Mechanics, July 2009.

Book Chapter

- A. Giri, J. Tao, **M. Kirca**, and A. C. To, "Mechanics of nanoporous metals," in *Handbook of Micromechanics and Nanomechanics*, edited by S. Li and X. L. Gao (Pan Stanford, Singapore), 2013.